BIOMIMETIC AND OPTIMAL DESIGNS OF GROOVED AERODYNAMIC THRUST BEARINGS FOR INCREASED LOAD CAPACITY

BY

YUNLUO YU

A thesis submitted to

the University of Birmingham

for the degree of

DOCTOR OF PHILOSOPHY

Department of Mechanical Engineering
School of Engineering
College of Engineering and Physical Science of
The University of Birmingham

June 2020

UNIVERSITY OF
BIRMINGHAM

University of Birmingham Research Archive

e-theses repository

This unpublished thesis/dissertation is copyright of the author and/or third parties. The intellectual property rights of the author or third parties in respect of this work are as defined by The Copyright Designs and Patents Act 1988 or as modified by any successor legislation.

Any use made of information contained in this thesis/dissertation must be in accordance with that legislation and must be properly acknowledged. Further distribution or reproduction in any format is prohibited without the permission of the copyright holder.

ABSTRACT

This thesis presents a PhD study which aims to develop novel micro surface structures for grooved aerodynamic thrust bearings to achieve a considerable increase in load capacity when operating under a given air film thickness acceptable in engineering practice, which will help widen the application of grooved aerodynamic thrust bearings while ensuring a safe operation. In this study, three approaches are presented: (1) the design of a biomimetic aerodynamic thrust bearing; (2) the optimisation of the groove geometry of spiral-grooved aerodynamic thrust bearings; and (3) the optimisation of the groove configuration of herringbone-grooved aerodynamic thrust bearings.

The novel biomimetic bearing is inspired by the micro surface structures of dragonfly wings; which presumably aid their flying and manoeuvre ability. The topography of the micro surface structures is studied, and the five most representative geometries are extracted before being applied onto bearings for performance evaluation. A computational fluid dynamics (CFD) model is developed to calculate the load capacity of the bearings under different velocities and flow angles. The optimal geometry and velocity angle are selected and manufactured on a bearing surface for experimental tests. The biomimetic bearing is found to increase the load capacity by up to 46.11% in comparison with

an optimised conventional spiral-grooved bearing.

The optimisation of the groove geometry of spiral-grooved aerodynamic thrust bearings is presented by combining the chaos-enhanced accelerated particle swarm optimisation (CAPSO) algorithm with the developed CFD model. Both discontinuous and continuous grooves are considered in the proposed method, which differs from existing studies. The optimisation process of an initial spiral-grooved aerodynamic thrust bearing is presented as a case study. The novel optimised grooves are discontinuous groove with completely new geometry. The load capacity of the novel optimised bearing, and that of an initial spiral-grooved bearing are compared experimentally. A 168.68% increase in load capacity has been found after optimisation.

The CAPSO algorithm and the developed CFD model are also combined to find the optimal groove configuration for herringbone-grooved aerodynamic thrust bearings. Different from existing studies, the optimal groove parameters in each section of the bearing are sought independently. An example of an optimised bearing is presented. The optimised herringbone grooves have different parameters in the inner and the outer sections, which is uncommon in existing grooves. The experiment results verified that compared with the non-optimised herringbone-grooved bearing, the new design can increase the load capacity by 30.77%.

In summary, through exploring novel micro surface structures for grooved aerodynamic thrust bearings using biomimetic and optimal design methods, this study presents a novel biomimetic bearing and two optimised aerodynamic thrust bearings with a completely new groove geometry and configuration. The novel designed bearings are found to have an increased load capacity compared to conventional spiral-grooved or herringbone-grooved bearings. The aims of this research have thus been met.

ACKNOWLEDGEMENTS

First and foremost, I want to sincerely appreciate my supervisor, Professor Kyle Jiang, for his support, encouragement and guidance during my study. I sincerely appreciate his contributions of ideas, time, networking and funding during my study. I also want to appreciate my second supervisor, Dr Carl Anthony, for his guidance and help during my study. Special thanks belong to Dr Guang Pu for his countless help and valuable advice during my study.

I gratefully acknowledge the scholarship from the university and the China Scholarship Council (CSC) which funded my study. I want to thank the team of laboratory technicians - Lee Gauntlett, Peter Thornton, and Jack Garrod - for their help with all experiment setup matters. I want to thank Janet for her excellent proofreading.

Special thanks belong to my supervisors in my Bachelor's and Master's degree studies: Professor Jin Qian, Dr Wei Li and Professor Deren Sheng for their support and help in my study and life. I also appreciate my friends: Dr Sunan Deng, Mr Tianchu Jiang, Dr Hanyang Xu, Mr Wuyang Zhuge, Mr Han Liu, Miss Narissa Li, Miss Yuanzhuo Mei, Miss Ya Zhou, Miss Ningge Wu, Miss Yixuan Wu and Miss Xiaoman Guo for their companion.

Finally, I want to appreciate my boyfriend Dr Yunfan Zhang and my family. Their unconditional support and encouragement have sustained me to persevere with my research till completion.

TABLE OF CONTENTS

ABSTRACT ..... **I**

ACKNOWLEDGEMENTS ..... **IV**

TABLE OF CONTENTS ..... **VI**

LIST OF PUBLICATIONS DURING THE PHD STUDY ..... **XI**

LIST OF ABBREVIATIONS ..... **XIII**

LIST OF SYMBOLS ..... **XIV**

LIST OF TABLES ..... **XVIII**

LIST OF FIGURES ..... **XX**

Chapter 1 INTRODUCTION **1**

1.1 Background and motivation 1

1.2 Aims and objectives 3

1.3 Thesis outline 4

Chapter 2 LITERATURE REVIEW **9**

2.1 Introduction 9

2.2 Typical air bearing classification and applications 9

2.2.1 Typical types of air bearings 10

2.2.2 Typical applications of air bearings..... 13

2.3 Numerical simulation of grooved aerodynamic bearings..... 16

2.3.1 Numerical modelling of grooved aerodynamic bearings..... 16

2.3.2 Improvement of numerical models for grooved air bearings..... 22

2.4 Experimental study of air bearings..... 25

2.5 Effects of the groove patterns on the bearing performances..... 27

2.5.1 Groove shape..... 28

2.5.2 Groove angle..... 28

2.5.3 The ratio of groove width to ridge width..... 29

2.5.4 The number of grooves..... 29

2.5.5 Grooved area..... 30

2.5.6 The depth of grooves..... 30

2.5.7 The surface profile of groove bottoms..... 31

2.5.8 Pumping direction..... 32

2.5.9 The surface with etched grooves..... 32

2.6 Optimisation schemes of grooved aerodynamic bearings..... 33

2.6.1 Optimisation by providing the optimal design rules..... 33

2.6.2 Optimisation by finding new geometries..... 36

2.6.3 Biomimetic designs..... 37

2.7 Summary 38

Chapter 3 CFD MODELLING AND VALIDATION OF GROOVED AERODYNAMIC THRUST BEARINGS 40

3.1 Introduction 40

3.2 Numerical simulation 41

3.2.1 Classical Reynolds equation 41

3.2.2 Modified Reynolds equation 44

3.2.3 Numerical solution of the discretized modified Reynolds equation ... 46

3.3 Grid independence test 48

3.4 Validation of the developed CFD model against published results ... 51

3.4.1 Verification of the load capacity's calculation – Case 1 51

3.4.2 Verification of the load capacity's calculation - Case 2 54

3.4.3 Verification of dynamic force coefficients' calculation - Case 3 57

3.4.4 Verification of dynamic force coefficients' calculation - Case 4 59

3.5 Summary 61

Chapter 4 A DRAGONFLY WING INSPIRED BIOMIMETIC AERODYNAMIC THRUST BEARING 63

4.1 Introduction 63

4.2 Background and motivations 64

4.3 Biomimetic features extraction 66

4.4 Biomimetic model design 71

4.5 Biomimetic bearing design 76

4.6 Experimental Verifications 82

4.6.1 Test rig description 82

4.6.2 Instrumentation 89

4.6.3 Results and discussion 92

4.7 Summary 94

Chapter 5 GROOVE GEOMETRY OPTIMISATION FOR SPIRAL-GROOVED AERODYNAMIC THRUST BEARINGS 97

5.1 Introduction 97

5.2 Background and motivations 98

5.3 Problem modelling 100

5.3.1 Geometrical expression of the groove 100

5.3.2 Groove geometry optimisation 102

5.4 Groove geometry optimisation 105

5.4.1 Groove geometry optimisation process 105

5.4.2 Optimisation results 108

5.5 Experiment results and discussion 116

5.6 Summary 119

Chapter 6 GROOVE CONFIGURATION OPTIMISATION OF HERRINGBONE-GROOVED AERODYNAMIC THRUST BEARINGS 122

6.1 Introduction 122

6.2 Background and motivations 123

6.3 Search area and the objective function 124

6.4 Groove configuration optimisation 126

6.4.1 Groove configuration optimisation Process 126

6.4.2 Optimisation results 129

6.5 Experiment results and discussion 135

6.6 Summary 139

Chapter 7 CONCLUSIONS AND FUTURE WORK 142

7.1 Introduction 142

7.2 Conclusions 142

7.3 Summary of novel contributions to knowledge 144

7.4 Proposal for future work 145

APPENDIX 149

REFERENCES 153

LIST OF PUBLICATIONS DURING THE PHD STUDY

Journal papers:

- Yunluo Yu, Guang Pu, Tianchu Jiang and Kyle Jiang*. Discontinuous grooves in thrust air bearings designed with CAPSO algorithm. International Journal of Mechanical Sciences, 165, p.105197, 2020.

- Yunluo Yu, Guang Pu, Tianchu Jiang and Kyle Jiang*. A dragonfly wing inspired biomimetic aerodynamic thrust bearing for increased load capacity. International Journal of Mechanical Sciences, p.105550, 2020.

- Yunluo Yu, Guang Pu, Tianchu Jiang and Kyle Jiang*. Optimisation of herringbone grooved thrust air bearings for maximum load capacity. (Submitted to ASME Journal of Tribology, July 2020.)

Conference papers and presentation:

- Yunluo Yu, Guang Pu and Kyle Jiang*. Modelling and analysis of the static characteristics and dynamic responses of herringbone-grooved thrust

bearings. In IOP Conference Series: Materials Science and Engineering (Vol. 280, No. 1, p. 012006), 2017. IOP Publishing.

- Yunluo Yu, Guang Pu and Kyle Jiang*. Numerical modelling and analysis of hydrostatic thrust air bearings for high loading capacities and low air consumption. In IOP Conference Series: Materials Science and Engineering (Vol. 280, No. 1, p. 012005), 2017. IOP Publishing.

LIST OF ABBREVIATIONS

APSO	Accelerated Particle Swarm Optimisation
CAPSO	Chao-enhanced Accelerated Particle Swarm Optimisation
CFD	Computational Fluid Dynamics
CMMs	Coordinate Measuring Machines
FDM	Finite Difference Method
FEM	Finite Element Method
FVM	Finite Volume Method
HGATB	Herringbone-grooved Aerodynamic Thrust Bearing
NGT	Narrow Groove Theory
NI	National Instruments
PSO	Particle Swarm Optimisation
SGATB	Spiral-grooved Aerodynamic Thrust Bearing
TPFPAJBs	Three-pad Fixing Pad Aerodynamic Journal Bearings

LIST OF SYMBOLS

b_1, W_{groove}	Width of the groove	m
b_2, W_{land}	Width of the ridge	m
c	The dynamic damping coefficient	N·s/m
C	The dimensionless dynamic damping coefficient	
D_a	The average value of the depth of grids	m
F	Maximum bearing load capacity	N
$f(Kn)$	Effective viscosity coefficient	
$g^{(i,*)}$	Optimal position in the i^{th} iteration	
h	Fluid film height	m
h_0	Designed air film thickness	m
h_g	Depth of grooves	m
k	The dynamic stiffness coefficient	N/m
K	The dimensionless dynamic stiffness coefficient	
Kn	Knudsen number	
K_p	Number of agents or particles	
L, T_L	The average value of the length and width of measured longitudinal veins	m

N_g, N	Number of grooves	
N_{it}	Iteration number	
n_{inner}, n_{outer}	Number of grooves of the inner and outer section	
P_{max}, P_{min}	Maximum and minimum pressure	Pa
P_{in}, P_{out}	The pressure at the inner and outer boundary of the bearing	Pa
P_0, P_1	Zero and first-order pressure field	
p_a	Ambient pressure	Pa
p	Pressure	Pa
r	Radius	m
r_{groove}	Dam radius	m
r_m	The average value of the inner and outer radius of the bearing	m
r_{in}, r_1	The inner radius of the thrust air bearing	m
r_{out}, r_2	The outer radius of the thrust air bearing	m
r_{s1}, r_{s2}	The inner and outer sealing radius	m
t	Time	s
U_1, U_2, V_1, V_2	Surface linear velocity	m/s
$\bar{u}_j$	The average surface linear velocity of the	m/s

	journal air bearing	
$\bar{u}_t$	The average surface linear velocity of the thrust air bearing	m/s
W, T_C	The average value of the length and width of measured cross veins	m
w_{gr}	The ratio of groove width to ridge width	
$w_{gr\text{-}inner}$, $w_{gr\text{-}outer}$	The ratio of groove width to ridge width of the inner and outer sections	
X	Vector of optimisation variables	
$\Delta h_{incline}$	Difference between the minimum and maximum air film thickness caused by an inclination	m
Λ	Bearing compressibility number	
Ω	Control volume	
α	Spiral angle	deg
α_{inner}, α_{outer}	Groove angle of inner and outer sections	deg
β	Velocity angle	deg
γ	Convergence factor	
ε	Maximum increment size	
η	Viscosity	N·s/m^2
θ	Angular position in the θ-axis	deg

θ_L , θ_w	The central angle of membranes and veins area	deg
ι	A random movement of the particle (or agent) within the searching area	
ρ	Density	kg/m^3
ϱ	Attraction parameter	
σ	Frequency number	
$\sigma_{sealing}$	Sealing ratio	
ς	Convergence parameter	
φ_i	Angle changed in the direction of the coordinate θ	deg
Φ_p	Rarefaction coefficient	
ω	Angular speed	rpm
ω_p	Perturbation frequency	rpm

LIST OF TABLES

Table 3-1: Design parameters and operating conditions of the spiral-grooved aerodynamic thrust bearing 49

Table 3-2: The load capacity and simulation time of different mesh grid numbers……50

Table 3-3: Geometrical parameter values of the spiral-grooved bearing in the work of Waumans et al. [131] 52

Table 3-4: Prescribed variables and constraints in the work of Hashimoto and Namba [92]..... 56

Table 3-5: Prescribed variables and constraints in the work of Malanoski and Pan [49], Zirkelback and San Andres [132] and Liu et al. [133] 57

Table 3-6: Prescribed variables and constraints in the work of Faria [134]..... 59

Table 4-1: Working conditions and design parameters of the studied bearings.....77

Table 4-2: Function description of the components of the test rig..... 84

Table 5-1: Working conditions and design parameters of the initial SGATB .. 106

Table 5-2: The vector of optimisation variables of the proposed method and the conventional method 109

Table 5-3: The load capacity of all the studied grooves 114

Table 6-1: Groove design variables and their permissible values in the optimisation process..... 127

Table 6-2: Design variables and operating conditions of the non-optimised HGATB 127

Table 6-3: The parameters of the non-optimised HGATB and the optimised HGATBs 132

Table 6-4: The load capacity of the non-optimised HGATB and the optimised HGATBs 134

LIST OF FIGURES

Figure 1-1: The structure of the thesis..... 4

Figure 2-1: The classification of air bearings based on the pressure generation mechanism..... 10

Figure 2-2: An overview of typical rigid and compliant bearings..... 12

Figure 2-3: Theoretical analysis methodologies of grooved bearings..... 17

Figure 3-1: Bearing geometry in the work of Waumans et al. [131]. Same geometry is used in Case 1 to verify the developed CFD model. 52

Figure 3-2: Verification of the developed model against the results of Waumans et al. [131]: (a) at 120,000 rpm; (b) at 180,000 rpm; and (c) at 240,000 rpm. Waumans et al. [131] explained the difference between the simulation and experimental results as a result of (1) deformation of the rotating disc caused by centrifugal forces; (2) variation of the length of the shaft caused by Poisson effect; (3) alignment and surface imperfections of bearing components. 54

Figure 3-3: The simulation results of (a) Hashimoto and Namba [92], and (b) the developed CFD model at 40,000 rpm under an air film thickness of 22.6 μm. The

two results are very similar in terms of the pressure distribution, load capacity, maximum and minimum pressure; which proves the accuracy of the developed CFD model. 55

Figure 3-4: Verification against the results of Malanoski and Pan [49], Zirkelback and San Andres [132] and Liu et.al [133]: (a) dimensionless dynamic stiffness coefficient, and (b) dimensionless dynamic damping coefficient. The results of the present analysis match very well with the others' simulation results, which verifies the accuracy of the developed CFD model. 58

Figure 3-5: Comparison with the results of Faria [134]: dimensionless dynamic stiffness coefficient and damping coefficient against various frequency number……...60

Figure 4-1: The comparison between the wing morphology of a bird and a dragonfly in flight. Different with bird wings, dragonfly wings cannot bend heavily to hold air and produce thrust during flying. Their high lifting capacity is very likely to be contributed to their surface structures. 66

Figure 4-2: The grids morphologies of dragonfly wings: (a) the testing sample of a dragonfly wing; (b) top five representative geometries after imaging with ×5 magnification. 68

Figure 4-3: An example of measuring results of an aligned quadrilateral grid of a dragonfly wing: (a) length of a longitudinal vein; (b) width of a longitudinal vein; (c) length of a cross vein; (d) width of a cross vein; (e) depth of a grid 71

Figure 4-4: Five biomimetic models inspired by dragonfly wings. Here, the veins are mimicked by black areas, while the membranes are mimicked by the white……...72

Figure 4-5: The load capacity of Models 1 - 5 with a velocity angle of 90^{o} 73

Figure 4-6: The load capacity of Models 1 - 5 against various velocity angles. The value of the velocity is fixed as 120 m/s. 74

Figure 4-7: Models 1a - 5a are developed for a circular surface. Here, the veins are mimicked by black areas, while the membranes are mimicked by the white……...75

Figure 4-8: The load capacity of Models 1a - 5a against various velocity angles and a fixed rotating speed of 90,000rpm 76

Figure 4-9: The geometry (left side) and dimensionless pressure distribution (right side) of (a) the biomimetic bearing; (b) the optimised spiral-grooved bearing; and (c) the reference spiral-grooved bearing..... 80

Figure 4-10: Dynamic performance of the biomimetic and optimised bearing

against various frequency number: (a) the dynamic stiffness coefficients and (b) the dynamic damping coefficients 81

Figure 4-11: Overview of the developed test rig which can be used to measure the load capacity of grooved aerodynamic thrust bearings from 0 to 90,000 rpm……..82

Figure 4-12: The main part of the test rig. The studied air film is formed between the rotating disc and the test bearing, while the rotating disc can rotate up to 90,000 rpm. The parallelism between the test bearing and the rotating disc is adjusted through the adjustable mount. 83

Figure 4-13: Arrangement of the associated systems for the lubricating, cooling and controlling of the motor. The motor is lubricated by oil mist and cooled by water for runs up to 90,000 rpm. The motor is controlled by an inverter. An oil mist separator is used to remove the oil from the oil mist to protect the environment……..85

Figure 4-14: The associated system: (a) the front view (left) and side view (right) of the motor; (b) the inverter of the motor; (c) the water pump to cool the motor; (d) the oil-mist generator (left) and the oil-mist separator (right)..... 86

Figure 4-15: The set-up to adjust the parallelism between the two surfaces. It

needs to be adjusted before each test to ensure the safety and accuracy of the tests..... 87

Figure 4-16: Measurement configuration..... 90

Figure 4-17: The test bearings: (a-b) the optimised spiral-grooved bearing; and (c-d) the biomimetic bearing. The surface structures of the bearings are manufactured by laser ablation (LASEA LS5-001). 91

Figure 4-18: The numerical and experimental load capacity of the biomimetic bearing and the optimised spiral-grooved bearing..... 93

Figure 5-1: An example of continuous and discontinuous grooves [142]..... 100

Figure 5-2: The process of finding a new groove 101

Figure 5-3: The groove geometry optimisation process..... 107

Figure 5-4: The optimisation process of: (a) the conventional optimisation method; and (b) the proposed optimisation method 110

Figure 5-5: The geometries of: (a) the initial spiral grooves; (b) the conventional herringbone grooves; (c) the conventional optimised grooves; (d) the novel optimised grooves, and the dimensionless pressure distribution of: (e) the initial spiral grooves; (f) the conventional herringbone grooves; (g) the conventional

optimised grooves; (h) the novel optimised grooves. Here, the grooves are represented by yellow areas, while the ridges are represented by the blue. ...112

Figure 5-6: The dynamic performance of the optimised and initial bearing: (a) the dimensionless dynamic stiffness coefficients and (b) the dimensionless dynamic damping coefficients against the frequency number at 80,000 rpm ..115

Figure 5-7: The test bearings: (a) the initial SGATB; and (b) the novel optimised bearing. The grooves are manufactured by laser ablation (LASEA LS5-001). 116

Figure 5-8: The theoretical and experimental load capacity of the initial SGATB and the novel optimised bearing.....117

Figure 6-1: Variables of herringbone grooves..... 125

Figure 6-2: The effect of the permissible values of the groove parameters on the non-optimised HGATB..... 128

Figure 6-3: The groove configuration optimisation process..... 129

Figure 6-4: The progress of (a) the conventional optimisation; and (b) the novel optimisation 131

Figure 6-5: The geometry of: (a) non-optimised HGATB; (b) conventional optimised HGATB and (c) novel optimised HGATB, and the dimensionless

pressure distribution of: (d) non-optimised HGATB; (e) conventional optimised HGATB and (f) novel optimised HGATB 133

Figure 6-6: The dynamic performance of the optimised and non-optimised bearing against the frequency number at 70,000 rpm 135

Figure 6-7: The geometry of (a) the non-optimised HGATB and (b) the novel optimised bearing 136

Figure 6-8: Simulation and experiment results on the load capacity of tested bearings..... 137

CHAPTER 1 INTRODUCTION

1.1 Background and motivation

The research carried out in this thesis arose from a need to maximize the load capacity of grooved aerodynamic thrust bearings for oil-free turbomachinery. This is consistent with the growing trends in oil-free turbomachinery which require more economic, clean and safe lubrication technologies [1]. Grooved aerodynamic bearings, which offer a lubrication-free, very low friction, no-pollution alternative to conventional contact bearings are ideal solutions for meeting these trends [2].

Grooved aerodynamic bearings are self-acting bearings which do not require a continuous supply of compressed air during operation. Among aerodynamic bearings, grooved bearings have advantages in that they are: easy and inexpensive to manufacture; have a relatively high load capacity, and excellent stability (all gas bearings suffer from stability issues, grooved bearings are more stable than some); thus they have been sought after in industry in recent decades [3–5]. Despite the above-mentioned benefits, comparing with oil-lubricated grooved bearings, grooved aerodynamic bearings do suffer from a small load

capacity due to the low viscosity of air film, which limits their applications [6]. Thrust bearings face even more challenges in this problem compared with journal bearings; since for applications like gas turbines, steam engine generators, etc., the axial loading can be much higher than the radial loading due to a pressure difference between the compressor and the turbine side.

To overcome this problem, the bearing clearance in grooved aerodynamic thrust bearings is designed to be very thin to generate enough pressure. However, even when the air film thickness has been reduced to a limited value, the load capacity of the grooved aerodynamic thrust bearing may still far below that which is required. Moreover, an extremely thin air film might easily result in some contact of two bearing surfaces, which would break the machine and cause serious accidents since the shaft rotates at high speeds.

How to increase the bearing load capacity while maintaining a suitable air film to prevent the contact of the shaft and the bearing has thus become one of the most important problems encountered in the design of grooved aerodynamic thrust bearings. The work described in this thesis is concerned with this challenge.

1.2 Aims and objectives

This PhD research aims to develop novel micro surface structures for grooved aerodynamic thrust bearings to achieve a considerable increase in load capacity when operating under a given air film thickness acceptable in engineering practice, which will help widen the application of grooved aerodynamic thrust bearings while ensuring a safe operation. The specific objectives of this study are:

i. Develop and validate a computational fluid dynamic (CFD) model to calculate the load capacity, dynamic stiffness and damping coefficients of grooved aerodynamic thrust bearings.

ii. Extract promising features from biomimetic samples which might lead to a high load capacity to design a biomimetic aerodynamic thrust bearing.

iii. Embed the developed CFD model of grooved aerodynamic thrust bearings in the chaos-enhanced accelerated particle swarm optimisation (CAPSO) algorithm to find the optimal groove geometry for spiral-grooved bearings and the optimal groove configuration for herringbone-grooved bearings.

iv. Develop a test rig and experimentally validate the proposed biomimetic and optimal design methods against the test rig measurements for load

capacity.

This study will focus on thrust bearings, but the proposed methods are also applicable in principle to journal bearing designs.

1.3 Thesis outline

This thesis consists of seven chapters. The structure of the thesis is demonstrated in Figure 1-1. The detailed outline of this thesis is introduced below.

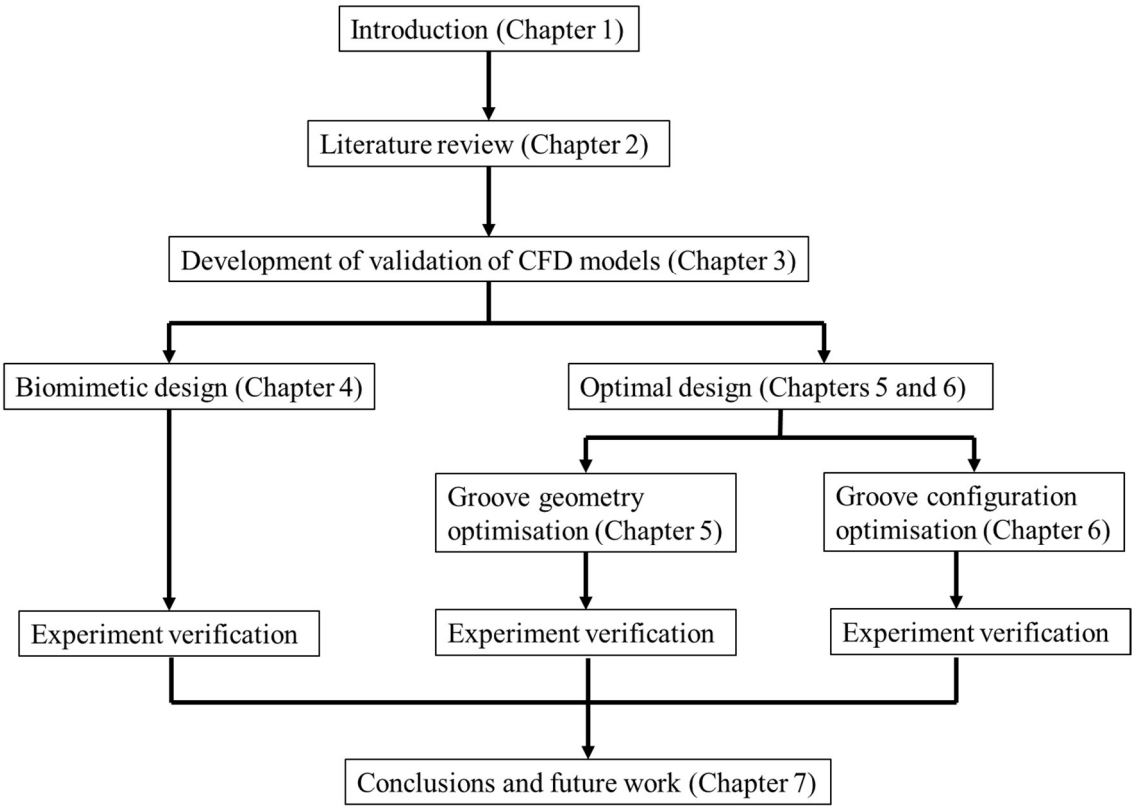


Figure 1-1: The structure of the thesis

Chapter 1 – Introduction

In this chapter, the basic background and motivations of the study are introduced, followed by the aims and objectives of this study. The outline of this thesis is also presented.

Chapter 2 – Literature review

This chapter presents a critical literature review that identifies the gaps in the state-of-the-art research, elucidating further the motivation for the study. It first introduces typical air bearing classifications and applications. Afterwards, it reviews the numerical and experimental studies of grooved aerodynamic bearings. Then, it reviews the effects of various groove design parameters on the performances of grooved aerodynamic bearings, followed by a review of optimisation schemes of grooved aerodynamic bearings.

Chapter 3 – CFD modelling and validation of grooved aerodynamic thrust bearings

This chapter presents the development of a CFD model and its validation process against publication results. In this chapter, the CFD model is developed by solving the Reynolds equation using finite volume and finite difference methods. Afterwards, an example of grid independence tests is given to ensure that the

simulation results are not affected by the quality of the mesh grids. Finally, the performance of the developed CFD model in calculating the load capacity, dynamic stiffness and damping coefficients of grooved aerodynamic thrust bearings is validated against the published results.

Chapter 4 – A dragonfly wing inspired biomimetic aerodynamic thrust bearing

This chapter introduces the development of a novel biomimetic aerodynamic thrust bearing, which is inspired by the micro surface structures of dragonfly wings. In this chapter, firstly, the topography of the micro surface structures of dragonfly wings, which presumably aid flying and manoeuvre ability of dragonflies, is studied and five most representative geometries are extracted to build biomimetic models. Then, based on the CFD model developed in Chapter 3, the load capacity of the biomimetic models under various velocities and flow angles are compared, and the best geometry and velocity angle are chosen to design the biomimetic bearing. Afterwards, a grooved aerodynamic thrust bearing test rig is developed from scratch to measure the load capacity of the biomimetic bearing and an optimised conventional spiral-grooved bearing to verify the proposed biomimetic design method.

Chapter 5 – Grooved geometry optimisation for spiral-grooved aerodynamic thrust bearings

This chapter proposes a novel CAPSO-based groove geometry optimisation method for spiral-grooved aerodynamic thrust bearings. Different from existing studies, the proposed method allows the possibility of finding either continuous or discontinuous grooves. As an example, the optimisation process of an initial spiral-grooved bearing is presented. The optimised bearing is compared with the initial spiral-grooved bearings both theoretically and experimentally to verify the proposed method.

Chapter 6 – Groove configuration optimisation of herringbone-grooved aerodynamic thrust bearings

This chapter proposes a novel CAPSO-based groove configuration optimisation method for herringbone-grooved aerodynamic thrust bearings. The proposed method optimises the groove parameters in sections, which differ from existing studies. As an example, the optimisation process of an initial herringbone-grooved bearing is implemented. The optimised groove is compared with the initial herringbone-grooved bearings both theoretically and experimentally to verify the proposed method.

Chapter 7 – Conclusions and future work

This chapter gives the conclusions and main contributions of this PhD study, followed by a few suggestions about future work.

CHAPTER 2 LITERATURE REVIEW

2.1 Introduction

In this chapter, grooved aerodynamic thrust bearing knowledge and research activities relevant to this study are reviewed. It begins with a brief introduction to typical air bearing classifications and applications in section 2.2. Then, in section 2.3, the numerical simulation of grooved aerodynamic bearings is reviewed. Section 2.4 addresses classical experimental studies of grooved aerodynamic thrust bearings. Then section 2.5 reviews the effects of various groove design parameters on the performances of grooved aerodynamic bearings. In section 2.6, optimisation schemes of grooved aerodynamic bearings are reviewed. The summary of this chapter is given in section 2.7.

2.2 Typical air bearing classification and applications

Air bearings are bearings that use air as the lubrication fluid to prevent contact between the bearing and the shaft [5,7,8]. This section introduces the typical types of air bearings, followed by a summarization of typical air bearing

applications.

2.2.1 Typical types of air bearings

The four types of engineering bearings used in various applications are rolling element bearings [9,10], magnetic bearings [11,12], oil bearings [13,14], and air bearings [15]. Among them, air bearings stand out since they use air as a lubricant, thus reducing the drag losses and improving the overall efficiency [16]. Air bearings can be classified into three types based on the pressure generation mechanism, as illustrated in Figure 2-1.

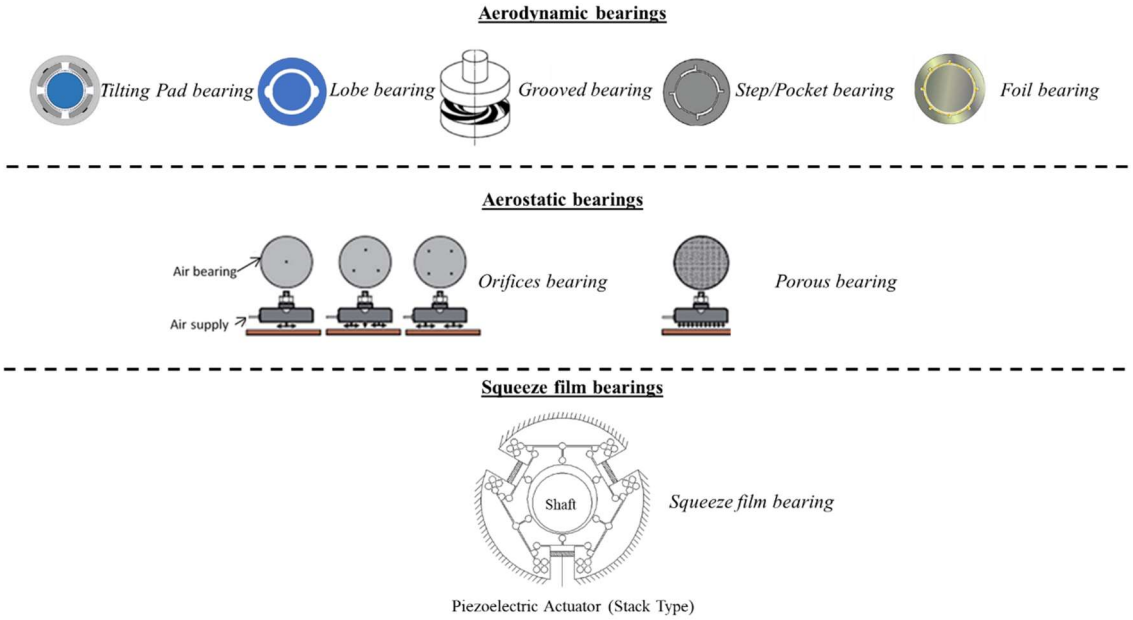


Figure 2-1: The classification of air bearings based on the pressure generation mechanism

(1) Aerodynamic bearings, or self-acting air bearings

This type of bearing produces a pressurized air film by the relative motion between the shaft and the bearing [17]; which will drag air into an air wedge and develop a pressure gradient. Comparing with aerostatic bearings, the principal advantage of aerodynamic bearings is that they can act without an external pressure source. However, aerodynamic bearings have starting and stopping friction since they have very small load capacity at low speeds, and results in some wearing of the bearing surfaces. Typical types of aerodynamic bearings include foil bearings [18], step/pocket bearings [19], lobe bearings [20], grooved bearings [5] and tilting pad bearings [21].

(2) Aerostatic bearings

Aerostatic bearings need an external air supply system to provide pressurized air either via orifices [22,23] or porous materials [24,25]. Different with aerodynamic bearings, aerostatic bearings can generate a load capacity even when the shaft is not rotating [26,27]. However, they suffer from pneumatic hammer, which is a self-excited instability that prove troublesome in externally pressurized air bearings [28]. Also, since they need a continuous supply of compressed air, the operation and maintenance costs are thus increased.

(3) Squeeze film air bearings

With these bearings, the pressurized air film is generated by a squeezing-film action [29] through external motion exciters like electromagnetic or piezoelectric devices [30]. In this way, squeezing-film air bearings do not require an external air supply or an air wedge.

The external pressurization and the self-acting principle can also be combined to generate pressurized air film, which is the case for hybrid air bearings [31]. In these bearings, the dry friction between the bearing and shaft during the start and stop process can be avoided, while the self-excited whirl instability can be postponed.

Air bearings can also be categorized into rigid geometry and compliant bearings, as presented in Figure 2-2.

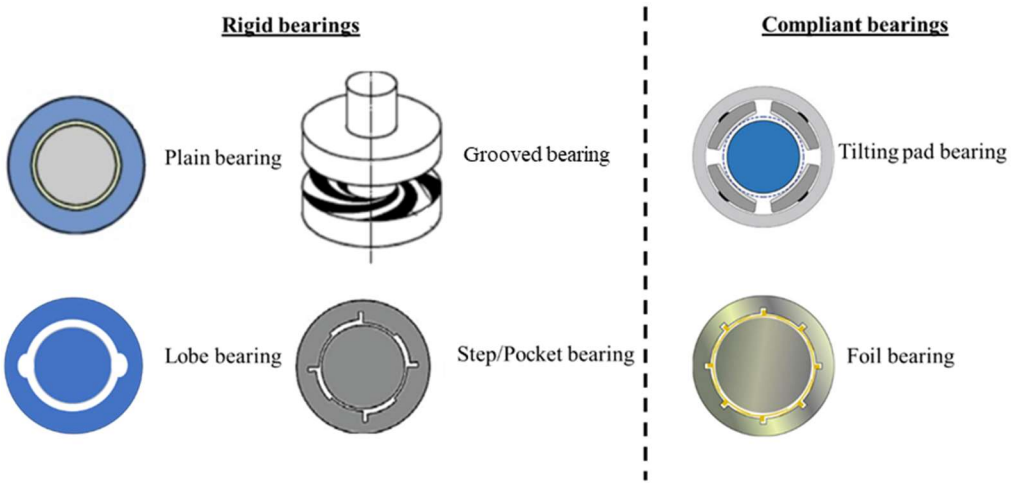


Figure 2-2: An overview of typical rigid and compliant bearings

(1) Rigid air bearings

When appropriately designed, rigid air bearings can generate a specific load capacity. Typical types of rigid air bearings include plain bearings [32], grooved bearings [5], lobe bearings [20], and step/pocket bearings [19].

(2) Compliant-surface air bearings

Comparing with rigid air bearings, compliant-surface air bearings could provide additional damping thanks to their compliant structures. Typical compliant air bearings include foil bearings [33], which consist of flexible foils; and tilting-pad air bearings which consist of divided bearing sleeves [21]. Foil bearings have received increasing interest among compliant air bearings thanks to their high level of reliability, but they require high manufacturing precision on the foil thickness and bumps [34].

2.2.2 Typical applications of air bearings

Before 1970, the applications of air bearings were largely limited by manufacturing accuracy and material qualities [35]. Due to the fast development of manufacturing technologies and high-performance computers over the past decades, there is a rising interest in air bearings. As a consequence, air bearings

are adopted in a wide range of industries, such as in coordinate measuring machines (CMMs) [36]; linear stages [37]; hard disk drives [38]; machines for the textile industry [39], food industry [40] and medical industry [41]; ultra-precision machine tools [42]; and turbomachinery [43]. The advantages of using air bearings in the above-mentioned industries are introduced below:

CMMs: In 1965, CMMs first utilized air bearing technology with a finely polished granite guide surface. Russ Shelton, considered to be the father of CMMs, discovered the advantages of building CMMs with porous carbon air bearings that offered straighter, frictionless motion [44]. Besides, error correction is also more effective since air bearings are smoother and more repeatable compared to rolling element bearings.

Linear stage: Air bearing linear stages can provide sub-micron accuracy, ultra-smooth motion and absolute repeatability since they replace the mechanical contact using a thin air film. Consequently, the friction, wear, vibration and hysteresis effects are avoided; while the precision of the motion can be improved [37].

Hard disk drives: The spindles in hard disk drives usually working with very high rotating speed. With low friction and low wear compared with traditional contact bearings, air bearings are found to give an excellent performance in hard disk

drives. Besides, air bearings do not have sealing problems, which are highly undesirable in hard disk drives. In 1961, IBM commercialized the first use of air bearing spindles in large hard disk drives, which allowed for higher data concentrations [45].

Machines for the textile. food, and medical industry: Since the lubricant (air) has no adverse effects on the environment and the products, air bearings are ideal bearing solutions for clean-room applications i.e. the medical, food, and textile industries [39,40,41];.

Ultra-precision machine tools: Air bearings are widely utilized in ultra-precision machine tools since they can provide very accurate velocity control, zero-friction and low vibration; thus improving the machining precision. By using air bearings, machining errors of ultra-precision machine tools can be limited to the order of the micro-inch [46].

Turbomachinery: Air bearings can play an important role in turbomachinery since the demand for more economical and clean lubrication technologies is increasing rapidly [47–49]. Air bearing supported turbomachinery is benefited from reduced weight and design simplicity since there is no need of an oil-supply system. Moreover, air bearing supported turbomachinery shows high temperature and speed capability by using air as the lubricant [50].

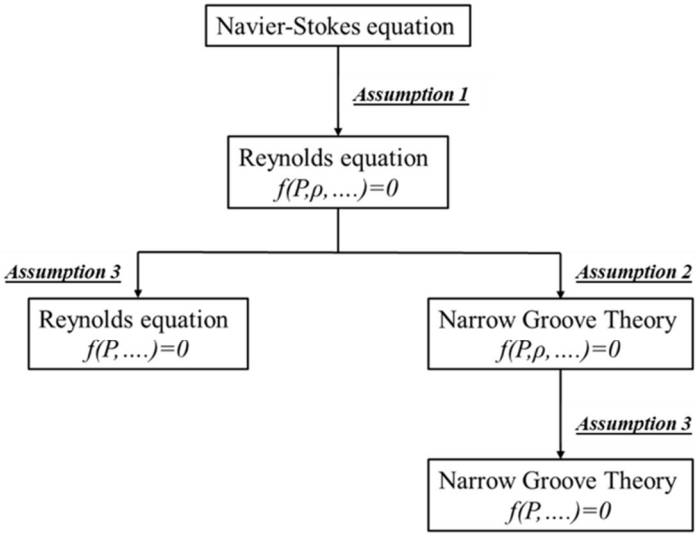
In general, air bearings have the advantages of zero-pollution, low friction, low wear, and high precision; hence, they are ideal bearing solutions for applications which demand high rotating speed, ultra-precision, and/or an oil-free environment. However, air bearings require a high machining tolerance, which consequently increases the cost of manufacturing. Besides, the load capacity of air bearings is small due to the low viscosity of air [51], which restricts their applications.

2.3 Numerical simulation of grooved aerodynamic bearings

2.3.1 Numerical modelling of grooved aerodynamic bearings

The numerical modelling of grooved aerodynamic bearings is challenging since the air film shows periodic geometrical discontinuities caused by the grooves. Figure 2-3 summarizes various grooved bearing modelling methodologies. The fundamental governing equation of grooved aerodynamic bearings is the Navier-Stokes equation [52,53]. Based on the Navier-Stokes equation, the Reynolds equation is derived with several assumptions to simplify the simulation process. Then, with further different assumptions, two branches are developed in simulating grooved aerodynamic bearings: narrow groove theory (NGT) and

direct discretization. The NGT assumes that the number of grooves is infinite, to get “smooth pressure” [54]. Contrarily, another branch used numerical discretization methods to model the ridges and grooves directly [55].



Assumption 1: (1) the fluids are Newtonian; (2) there is no slip at boundaries; (3) the inertial and body forces are much smaller than the viscous forces; (4) the density, pressure and viscosity of the fluid are constant in the film thickness direction; (5) the film thickness is much smaller compared with bearing lengths or radius.

Assumption 2: (1) the total pressure change across a groove-ridge pair equals to the total pressure change across the groove and ridge respectively; (2) the derivative of pressure across a groove-ridge pair is constant; (3) the pressure shows periodic distribution along the circumferential direction of the bearing; (4) the pressure gradient normal to bearing surfaces is constant on both sides of the interfaces of the grooves and ridges; (5) the mass flow parallel to the bearing surfaces follows the continuity principle on the interfaces of the grooves and ridges; (6) the curvature effect is neglected.

Assumption 3: (1) lubricants are isothermal; (2) lubricants are ideal gas.

Figure 2-3: Theoretical analysis methodologies of grooved bearings

2.3.1.1 Narrow groove theory

The Reynolds equation was first used only for incompressible fluid lubricants [56].

In 1913, Harrison [57] extended the Reynolds equation to compressible fluid lubricants by making the following assumptions: (1) the fluids are Newtonian; (2) there is no slip at boundaries; (3) the inertial and body forces are much smaller than the viscous forces; (4) the density, pressure and viscosity of the fluid are constant in the film thickness direction; (5) the film thickness is much smaller compared to bearing lengths or radius. These assumptions correspond to Assumption 1 in Figure 2-3.

Based on Assumption 1, Whipple [58] further introduced the NGT to deal with the periodic geometrical discontinuities caused by the grooves. The NGT assumes that the number of the grooves is infinite, and thus an infinite small pressure fluctuation is achieved over a ridge-groove area. In this way, the overall pressure distribution of the grooved bearing will be smoother. The NGT adopts several assumptions to derive a modified Reynolds equation, which corresponds to Assumption 2 in Figure 2-3: (1) the total pressure change across a groove-ridge pair equals to the total pressure change across the groove and ridge respectively; (2) the derivative of pressure across a groove-ridge pair is constant; (3) the pressure shows periodic distribution along the circumferential direction of the bearing; (4) the pressure gradient normal to bearing surfaces is constant on both sides of the interfaces of the grooves and ridges; (5) the mass flow parallel to the bearing surfaces follows the continuity principle on the interfaces of the grooves

and ridges; (6) the curvature effect is neglected.

Boeker et al. [59] commented that the NGT could achieve a “fairly rough but useful estimate of the operating characteristics and the optimal properties of such bearings”. In 1967, Whipple’s work was extended by Whitley [60], who introduced the end effects and considered the curvature effect and the number of grooves.

The applicability of the incompressible NGT was assessed by Muijderman [61] in depth. At the same time, Vohr and Pan [62] proposed an NGT-based simulation model for grooved journal gas bearings. In 1965, Malanoski and Pan [54] extended Vohr and Pan’s work and presented an analysis of static and dynamic performances of spiral-grooved thrust gas bearings.

Vohr and Chow [63] also applied an NGT-based model to simulate herringbone-grooved journal bearings. The NGT-based model took Assumption 1 and Assumption 2 to derive a modified Reynolds equation, which could obtain the pressure distribution within the gas film of the bearing. Besides, other assumptions (Assumption 3 in Figure 2-3) are incorporated to simplify the Reynolds equations further: (1) lubricants are isothermal; (2) lubricants are ideal gas. With these two assumptions, the Reynolds equations are expressed in pressure only, rather than in pressure and density. Since the NGT assumes that the number of grooves is infinite, the solutions are satisfied only when the number

of grooves is large enough.

2.3.1.2 Direct discretization

Instead of assuming the number of grooves is infinite, the Reynolds equation can also be directly solved after discretization. In 1997, Van der Stegen [64] used the finite difference method (FDM) to calculate the load capacity of herringbone-grooved gas journal bearings at large compressibility numbers. However, it needs to be pointed out that due to discontinuity of the fluid film at the interface of the grooves and ridges, the FDM might show convergence difficulties when solving the Reynolds equations.

In 1970, Reddi and Chu [65] introduced an analysis for a grooved bearing with compressible gas lubricants based on the finite element method (FEM). Miller and Green [66] compared the FVM and the FEM in simulating spiral-grooved gas seals. They concluded that the FVM used approximately 50% less time than the FEM for their cases.

Besides the FDM- and FEM-based schemes, The finite volume method (FVM) has also been widely adopted to deal with discontinuous air film [43, 44]. Compared to the FEM, the FVM shows better convergence performance [69]. However, the FEM can achieve a higher accuracy compared to the FVM.

Yu and Ma [70] used an FDM based on the Reynolds equation and an FVM based on the Navier-Stokes equation to calculate the two-dimensional flow field of an aerostatic thrust bearing. They concluded that the FDM-based simulation requires a smaller number of mesh grids and achieves a higher calculation efficiency than the FVM-based simulation. However, the FVM-based simulation can calculate the pressure change with a higher calculation resolution.

The matrix equation of air bearings can be solved by iteration methods i.e. Gauss-Seidel iteration. Bonneau and Absi [71] analysed herringbone-grooved journal bearings with a small number of grooves. They used the Newton-Raphson method to solve the discretized Reynolds equations. Unlike the NGT, which is only valid for a large number of grooves, their work successfully deals with the simulation of grooved bearings with a small number of grooves.

In summary, since the mesh of grooved bearings needs to coincide with the air film discontinuities, it is challenging to direct discretise Reynolds equations [72]. As a result, it is challenging and time-consuming to embed direct discretization methods into optimisation algorithms [73].

2.3.2 Improvement of numerical models for grooved air bearings

The classic Reynolds equation is derived from the Navier-Stokes equation with thin-film assumptions (Assumption 1 in Figure 2-3), which ignore the rarefaction effect [74] and the inertial effect [75]. With further assumptions (Assumption 3 in Figure 2-3) that lubricants are ideal gas and isothermal, Reynolds equations are expressed only in pressure, instead of in density and pressure. However, some applications need to consider the real gas effect [76] and/or the thermal effect [77] to achieve accurate simulation results. These effects are discussed in detail below.

2.3.2.1 Rarefaction effect

At low pressures, the rarefaction effect becomes critical for air bearings [74,78]. The rarefaction effect is related to the Knudsen number Kn, which is the ratio of the mean free molecular path of air to the film thickness. If $Kn < 0.001$, airflow is considered as a continuum flow. If $0.001 < Kn < 0.1$, the air is considered as rarefied and the first-order slip boundary conditions need to be considered. If $0.1 < Kn < 10$, the air is considered as a transition flow, and the second-order or higher-order slip boundary condition needs to be considered. If $Kn > 10$, the air is considered as a molecular flow [79].

The rarefaction effect could affect the performances of air bearings. At Kn = 0.1, Hsing and Malanoski [80] found a 20% deviation in simulating the stiffness of a spiral-grooved thrust bearing for models with or without considering the rarefaction effect. Shukla et al. [81] concluded an increasing Kn would lead to decreasing load capacity.

2.3.2.2 Inertia effect

It is widely accepted that when the modified Reynolds number $Re^{*} < 1$, the inertia effect can be neglected in the simulation; when the modified Reynolds number is larger than 1, the inertia effect needs to be considered [82]. Sahlin et al. [83] and Cupillard et al. [84] confirmed that the inertia effect would affect the load capacity of bearings by analysing infinitely long parallel sliders with dimples. Dobrica and Fillon [85] concluded that when the texture aspect ratio and the Reynolds number are both small, the solutions of the Navier-Stokes and Reynolds equations match well with each other. However, for a large modified Reynolds number, corrections for the inertia effect need to be considered in solving Reynolds equations, to improve the accuracy.

2.3.2.3 Real gas effect

Many applications have treated air as an ideal gas [86,87]. However, when air is working in a humid environment or near the saturation line, this assumption is not valid. In such an environment, the density terms become a non-linear function of the temperature and pressure, which is difficult to be simplified. Guenat and Schiffmann [88] studied the real gas effect for plain, step and herringbone-grooved journal air bearings. They concluded that the bearing performances were largely reduced by the real gas effect, losing 50% in load capacity, and close to 100% in dynamic stability for specific configurations. However, the dynamical stability might increase for several orders of magnitude in some cases.

Guenat and Schiffmann [88] concluded that the effect of the humid air on the load capacity could be ignored, but it would reduce the dynamic stability by 25%. Therefore, for applications where the air bearings are operating in warm and humid environments, a stability margin needs to be considered.

2.3.2.4 Thermal effect

Hughes and Osterle [89] concluded that compared with the wetted surface, the volume of the fluid film is so small that it behaves isothermally, thus an isothermal assumption is valid usually in the simulation of air bearings. With the isothermal

assumption, the Reynolds equations can be expressed only in pressure with constant viscosity. Wilson [90] concluded that for a wide range of temperatures (up to 1310.9 K), the model with isothermal assumptions could achieve better accuracy in simulating bearing performances, including the load capacity.

2.4 Experimental study of air bearings

Performing experimental studies on grooved air bearings are the consequential and natural step of the development of the theoretical framework by Reynolds. Since aerodynamic bearings are designed to work under high rotating speeds, it is crucial to avoid direct contact of the rotor and the bearing when designing the test rig for grooved thrust bearings.

This can be solved by ensuring the parallelism between two bearing surfaces both at static conditions and high speeds. One way to achieve that is through mechanical fittings, as shown by Waumans et al. [91]. The main part of their test rig consisted of a shaft and a titanium rotor disc which was supported by aerostatic journal bearings. The diameter of the shaft and the rotor disc was 6 mm and 20 mm respectively. The testing bearings consisted of interchangeable bronze parts and acted on the inner side of the rotor disc. The grooves were

machined by micro-milling. By specifying stringent fabrication tolerances on components, the close parallelism between two bearing surfaces at high speeds can be ensured.

A similar set-up can be found in the work of Cunningham et al. [92], who developed a test rig to explore the effect of herringbone-grooved geometries and clearances on a half-frequency whirl. In their test rig, a vertical steel rotor was mounted in two sleeves. The grooves were machined in the surface of the rotor. The rotor was supported by an aerodynamic thrust bearing at low speeds. The rotors were driven by a turbine. The air supply of the turbine was controlled by an electronic controller. By adjusting the air supply, the speed of the rotor could be adjusted.

The shaft can also be driven by motor through a coupling, as shown by Mohd Firdaus Bin Hassan [93]. Although his test rig was designed to test foil-air bearings, its shaft-driven method can also be used in developing the test rig for grooved air bearings. In his test rig, the shaft and the motor were connected using a cylindrical plastic coupling with a hexagonal inner surface that matched the 7 mm hexagonal cross-section segments projecting from the adjacent ends of the driven and driving shafts. This coupling was provided by a motor manufacturer. Hassan pointed out that this coupling would exert a bending moment, but he

explained that this limitation is not critically important, as evidenced by the experimental tests.

The parallelism between bearing components can also be adjusted directly, as shown in the test rig developed by Hashimoto et al. [6,94,95]. The test rig consisted of a test bearing, a rotating shaft, and a stator. The shaft was driven to rotate by a motor which could run up to 60,000 rpm. The motor was cooled by water, while an air spring vibration isolator was used to eliminate the vibration caused by disturbances. The grooved geometry was machined by etching. The parallelism between the bearing surfaces was examined by measuring the air film thickness at 12 points in the circumferential direction using an eddy current sensor. The parallelism inclination between the bearing surfaces was controlled within 5 μm in their studies.

2.5 Effects of the groove patterns on the bearing performances

Groove patterns are used widely and studied intensively in this PhD research since they can significantly affect the load capacity of bearings. The groove design parameters, including the groove shape, the groove angle, the ratio of

groove width to ridge width, the depth of grooves, the number of grooves, and the grooved area obviously affect bearing performances. The following section introduces the influences in detail.

2.5.1 Groove shape

The groove shape is found to have an important influence on the static and dynamic performance of grooved bearings. Hashimoto and Ochiai [96] compared the performances of pocketed, stepped, spiral-grooved and herringbone-grooved thrust gas bearings under the same groove/step/pocket depth, and concluded that the spiral-grooved bearing achieves the smallest friction torque and highest stiffness coefficients at high speeds. After that, Hashimoto and Namba [97] found that when grooves bend in the vicinity near the outer boundary of the spiral-grooved thrust bearing, the air film thickness and dynamic stiffness can be maximized. Chow and Vohr [98] found that journal bearings with helical grooves show good stability under lightly loaded conditions.

2.5.2 Groove angle

The effect of the groove angle on the load capacity of grooved aerodynamic thrust bearings has been investigated by many studies [76, 77]. They all concluded that

there is always an optimal groove angle which provides the highest load capacity. Shan et al. [99] investigated the effect of groove angles on the load capacity of spiral-grooved aerodynamic thrust bearings with different numbers of grooves. The effect of a spiral angle on the stiffness of spiral-grooved aerodynamic thrust bearings was investigated by James and Potter [100], who concluded that an angle of about 81^0 should be used for maximum axial bearing stiffness.

2.5.3 The ratio of groove width to ridge width

Shan et al. [99] analysed the effect of the ratio of groove width to ridge width on the load capacity of grooved aerodynamic thrust bearings and concluded that the highest load capacity was achieved when the ratio of groove width to ridge width ranges from 1 to 0.7. Same conclusions can be found in other studies [101,102]. However, the motion stability of a grooved aerodynamic thrust bearing simply decreases with the ratio of groove width to ridge width, as concluded by Zhang and Shan [102].

2.5.4 The number of grooves

Van der Stegen [64] concluded that for different ranges of compressibility numbers, the influence of the number of grooves on the load capacity is different.

For high compressibility numbers, when the number of grooves ranges from 4 to 6, the load capacity will increase with the number of grooves. However, when the number of grooves is large enough, the change in the load capacity is small [102,103]. At this condition, the NGT theory becomes valid.

2.5.5 Grooved area

Partially or fully covered grooves have a different effect on the bearing performances, including the load capacity and stability. Tala-Ighil et al. [104] concluded that partially covered grooves could achieve a higher hydrodynamic load capacity than fully covered grooves. Many studies [105–107] also confirmed this conclusion. However, Cunningham et al. [92] concluded that partially grooved bearings are less stable than fully grooved ones.

2.5.6 The depth of grooves

For thrust bearings, there is an optimum depth of grooves which can achieve the maximum load capacity. Any depth smaller or larger than the optimum depth will lead to a lower load capacity and damping coefficient.

Van der Stegen [64] summarized that at low compressibility numbers, the

optimum depth of grooves is almost fixed, but when the compressibility numbers increase, the optimum depth of grooves will gradually rise. There is an optimum ratio of the air film thickness in the grooved region and ridge region, which achieves the maximum axial stiffness as well. It is found to be around 1.8 for spiral-grooved thrust bearings [108].

2.5.7 The surface profile of groove bottoms

Maday [109] concluded that the taper-step is the optimal groove profile for slider bearings of infinite width. Whereas Chow et al. [110] compared the load capacity of three film profiles, tapered, taper-step and flat-step; and concluded that the taper-step bearing achieved the highest load capacity among the studied profiles. The load capacity of a taper-step enclosed-pocket bearing is also higher than the load capacity of a spiral-grooved bearing with a step profile. Gross [111] introduced the work of other researchers on finite width bearings with various groove profiles, including taper, taper-flat, flat-step and curved with compressible lubricants.

Ausman [112] optimised a step thrust bearing with compressible lubricants at various compressibility numbers and radius ratios. Fesanghary and Khonsari [113] proposed novel deformable groove designs for improving the load capacity of

grooved bearings. They assumed that the fluid film thickness is varied along the length of the groove and proposed three thickness patterns which are spline, linear and constant. They concluded that the optimised grooves which have a spline thickness profile can achieve a 45% higher load capacity compared to the original thickness profile.

2.5.8 Pumping direction

The bearing performances are different when the pumping direction is different. For an inward or outward pumping groove, the bearing will not generate any load capacity if the pumping direction is inverted.

Malanoski and Pan [54] concluded that the inward-pumping bearings outperform the outward-pumping bearings by achieving a higher load capacity. Moreover, inward-pumping bearings have better sealing. Shahin et al. [114] concluded that the outward-pumping spiral-grooved dry gas seals could have a negative stiffness and show instability compared with the inward-pumping version.

2.5.9 The surface with etched grooves

The grooves can be etched either on the rotor or the bearing. Malanoski and Pan

[54] concluded that the stability of spiral-grooved thrust gas bearings increases when the grooves are etched on the rotor, especially at high compressibility numbers. The same conclusion was made by Pan and Kim [115] for conical herringbone-grooved gas bearings, and by Fleming and Hamrock [116] for herringbone-grooved journal bearings.

2.6 Optimisation schemes of grooved aerodynamic bearings

Since air has comparatively low stiffness compared to liquids and solids, air bearings suffer from low load capacity. For aerostatic bearings, the load capacity can be increased easily by increasing the supply pressure. However, the load capacity of aerodynamic bearings is not so easily increased since it does not rely on any external compressed air. For grooved bearings, many studies have been undertaken to investigate how the groove parameters would affect their load capacity, as discussed below.

2.6.1 Optimisation by providing the optimal design rules

Since groove parameters can determine the performances of the bearing, many

studies have focused on providing optimal design rules for grooved aerodynamic bearings by finding the optimal groove parameters. James and Potter [100] presented a flexible design method for spiral-grooved aerodynamic thrust bearings. They calculated the static stiffness, load support, gas flow, compressor efficiency and power consumption and gave the theoretical performance curves. They suggested different spiral angles for high bearing stiffness and high compressor efficiency.

Satomi et al. [101] proposed optimisation principles for designing spiral-grooved aerodynamic thrust bearings based on the computed results obtained by FEM programs specially developed for the analysis of spiral-grooved bearings. They thoroughly investigated the influences of each of the design specifications on the load capacity, stiffness and damping ratio.

Song et al. [117] analysed the performance of spiral-grooved journal gas bearings in various operating conditions and presented guidelines for designing these bearings, by discussing the effects of grooved structural parameters on their dynamic performance.

Wong et al. [118] presented micro-bearing design charts that relate bearing geometry to performance and pointed out that there is a design tradeoff between the maximum working speed and the load capacity.

Chen et al. [119] established a mathematical model to calculate the pressure distribution of spiral-grooved aerodynamic bearings. Based on the result, they concluded that the structure parameters affect the bearing's static characteristics and the gas film pressure distribution; thus, reasonable design of structural parameters can increase the load capacity of the bearings.

Liu et al. [120] analysed the effects of the width, depth and orientation angle of grooves on the load capacity of three-pad fixing pad aerodynamic journal bearings (TPFPAJBs). They concluded that the ratio of the width to the diameter and the compressibility number have important effects on the load capacity of TPFPAJBs for a grooved surface.

Zhang et al. [103] analysed the influences of various parameters on the load capacity of a spiral-grooved thrust bearing. They concluded that the load capacity increases with the number of grooves and the bearing number; while there is an optimum value of groove angle, the ratio of groove depth to air film thickness, and the ratio of groove width to ridge width which can achieve the maximum load capacity. Zhang et al. [86] also gave the optimum groove parameters for the herringbone-grooved thrust and journal bearings.

2.6.2 Optimisation by finding new geometries

Recently, keen interest has been paid to develop new groove geometries which can achieve higher load capacity than conventional spiral-grooved or herringbone-grooved air bearings, but there are limited publications.

Hashimoto and Namba [97] described an optimum design method to find the optimal groove geometry of aerodynamic thrust bearings which could achieve improved bearing characteristics, such as bearing torque, dynamic stiffness, or air film thickness. When optimising the friction torque or the air film thickness, the optimised groove geometries are found to have a similar form with spiral groove geometry. When optimising the dynamic stiffness, the optimised groove is found to be a modified spiral groove. Ibrahim et al. [95] applied the groove geometry optimisation method proposed by Hashimoto et al. [6,97] to design thrust aerodynamic bearings for hard disk drive spindle motors.

Similarly, Fesanghary and Khonsari [121] adopted mathematical optimisation methods to find an optimum groove for parallel flat surface bearings. They concluded that compared to conventional spiral grooves, the optimum grooves can achieve a 36% higher load capacity, as verified by experiments.

Schiffmann [122] introduced enhanced groove geometries which can increase

the stability threshold of grooved bearings and the ratio of clearance to diameter. They summarized the optimum groove pattern distributions for a variety of dimensions and compressibility numbers to provide general design guidelines for herringbone-grooved gas journal bearings.

Ikeda et al. [123] developed a hydrodynamic bearing for high-speed motor spindles. The designed bearing is covered by non-uniform herringbone grooves. Experiment results proved that by adopting the non-uniform herringbone grooves, the spindle achieves a 20% higher maximum rotating speed than using uniform grooves.

2.6.3 Biomimetic designs

Biomimetic designs are the process of creating innovative ideas inspired by nature. This approach adapts some processes of natural organisms to solve design problems and provide excellent solutions for various engineering problems. Xu and Todorov [124] designed a biomimetic robotic hand after analysed the biomechanical advantages of human hands. The experiment shows that the biomimetic hand can be teleoperated to grasp objects with various natural hand postures. Yao et al. [125] designed a biomimetic robotic hand device, which they named a soft muscle glove. Experimental results showed that the biomimetic

device can achieve the functional range of motion of human hands and perform various grasp types. Shen et al. [126] designed a biomimetic underwater robot which is inspired by pectoral fish swimming modes.

Biomimetic designs have also been widely used in fluid-film lubrications. The John Crane Corporation designed dry gas seals with a biomimetic groove inspired by bird wings. They concluded that the biomimetic groove leads to a stiffer gas film compared to the conventional spiral groove [127]. Peng et al. [128] concluded that the outline of bird wings has a specific correlation with the groove pattern of dry gas seals. Gao et al. [129] presented a biomimetic aerostatic bearing which is inspired by the wings of long-eared owls. Compared to the conventional aerostatic bearing, the biomimetic one requires a 27% less supply pressure. However, although the biomimetic design has been successfully applied in aerostatic bearings and dry gas seals, it has not been applied to design aerodynamic bearings before this study.

2.7 Summary

This chapter presents a stage-of-the-art literature review on grooved aerodynamic thrust bearings and other research that is relevant to the study while highlights the knowledge gaps identified. Section 2.2 presented a description of

various types of air bearings and their typical applications; followed by sections 2.3 and 2.4, which respectively introduced theoretical and experimental studies on grooved aerodynamic bearings. Section 2.5 then addresses the effect of the groove patterns on the performances of grooved aerodynamic bearings. The last part of the review (section 2.6) was concerned with the optimisation schemes of grooved aerodynamic bearings.

After reviewing the above-mentioned literature, it can be found that developing grooved aerodynamic thrust bearings with improved load capacity is highly desirable to widen the applications of air bearings and to provide an ideal bearing solution to high-speed oil-free turbomachinery. Also, the literature review in section 2.6 shows that although the effect of different design parameters on the load capacity has been studied widely, it is challenging to find new groove geometries which have a better performance than conventional spiral and herringbone grooves. Moreover, biomimetic design methods, which provide excellent solutions for various engineering problems, have not been applied in designing aerodynamic bearings. This study will address these challenges.

CHAPTER 3 CFD MODELLING AND VALIDATION OF GROOVED AERODYNAMIC THRUST BEARINGS

3.1 Introduction

An accurate CFD model plays a significant role in the design and optimisation of grooved aerodynamic thrust bearings. With an accurate CFD model, the performance of the designed bearings can be predicted and compared, thus minimizing the experimental time and cost. In this chapter, to achieve the pressure distribution of grooved aerodynamic thrust bearings, a CFD model is developed by solving the Reynolds equation using finite volume and finite difference methods. As part of this work, the model is developed based on Dr Guang Pu's work in grooved aerodynamic journal bearings [130].

In this chapter, firstly, the Reynolds equation and its numerical solution method are introduced. Then, an example of grid independence tests is given to ensure that the simulation results are not affected by the quality of the mesh grids. Finally, the performance of the developed CFD model in calculating the load capacity,

dynamic stiffness and damping coefficients of grooved aerodynamic thrust bearings is validated against the published results.

The rest of this chapter is organized as follows: Section 3.2 introduces the numerical simulation process for grooved aerodynamic bearings; section 3.3 shows an example of grid independence tests; section 3.4 presents the validation process of the developed simulation models in calculating the load capacity, dynamic stiffness and damping coefficients of grooved aerodynamic thrust bearings; section 3.5 gives the summary of this chapter.

3.2 Numerical simulation

3.2.1 Classical Reynolds equation

The pressure distribution within the air film of grooved aerodynamic bearings is governed by the Reynolds equation. It was first derived by Osborne Reynolds in 1886 [131]. Reynolds restricted his analysis to incompressible fluids, while Harrison included the effects of compressibility in 1913 [132].

In the direct derivation of the Reynolds equation of aerodynamic bearings, the following assumptions are adopted:

1. the mass of the thin fluid film is neglected;

2. the pressure and viscosity are constant in the air film thickness direction;

3. the fluid is Newtonian fluid;

4. the fluid flow is laminar;

5. inertia and surface tension forces are negligible;

6. the fluid is isothermal;

7. the fluid is an ideal gas.

The full Reynolds equation is listed as follows:

$$\frac{\partial}{\partial \mathrm{x}}\left[\frac{\rho h^3}{12\eta}\frac{\partial p}{\partial x}\right]+\frac{\partial}{\partial \mathrm{y}}\left[\frac{\rho h^3}{12\eta}\frac{\partial p}{\partial y}\right]=\frac{\partial}{\partial x}\left[\frac{(U_1+U_2)\rho h}{2}\right]+\frac{\partial}{\partial y}\left[\frac{(V_1+V_2)\rho h}{2}\right]+\frac{\partial \rho h}{\partial t} \tag{3-1}$$

where ρ is the density; *p* the pressure; *h* the air film thickness; *η* the viscosity; U_1, U_2, V_1, V_2 the corresponding surface linear velocity; and t the time. For journal air bearings, the Reynolds equation is:

$$\frac{\partial}{\partial \mathrm{x}}\left[\frac{\rho h^3}{12\eta}\frac{\partial p}{\partial x}\right]+\frac{\partial}{\partial \mathrm{y}}\left[\frac{\rho h^3}{12\eta}\frac{\partial p}{\partial y}\right]=\frac{\partial}{\partial x}\left[\bar{u}_j \rho h\right]+\frac{\partial \rho}{\partial t} \tag{3-2}$$

here, $\bar{u}_j$ is the average surface linear velocity of the journal air bearing. After introducing the following dimensionless variables as:

$$H = \frac{h}{h_0},\ X = \frac{x}{r_0},\ Y = \frac{y}{r_0},\ P = \frac{p}{p_a},\ T = t\omega,\ \Lambda = \frac{6\eta\omega r_0^2}{p_a h_0^2} \tag{3-3}$$

where h_0 is the designed air film thickness; ω the angular speed; p_a the ambient pressure; and r_0 the bearing radius. The dimensionless variables are represented using corresponding capital letters. The dimensionless Reynolds equation for journal air bearings is then given as:

$$\frac{\partial}{\partial X}\left[PH^3\frac{\partial P}{\partial X}\right] + \frac{\partial}{\partial Y}\left[PH^3\frac{\partial P}{\partial Y}\right] = \Lambda\frac{\partial}{\partial X}(PH) + 2\Lambda\frac{\partial(PH)}{\partial T} \tag{3-4}$$

The Reynolds for thrust bearings is given in polar coordinates as:

$$\frac{\partial}{\partial \mathrm{r}}\left[\frac{r\rho h^3}{12\eta}\frac{\partial p}{\partial r}\right] + \frac{1}{r}\frac{\partial}{\partial \theta}\left[\frac{\rho h^3}{12\eta}\frac{\partial p}{\partial \theta}\right] = \frac{\partial}{\partial \theta}[\bar{u}_t\rho h] + r\frac{\partial \rho h}{\partial t} \tag{3-5}$$

Here, $\bar{u}_t$ is the average surface linear velocity of the thrust air bearing. After introducing the following dimensionless variables as:

$$H = \frac{h}{h_0},\ R = \frac{r}{r_{\mathrm{in}}},\ P = \frac{p}{p_a},\ T = t\omega,\ \Lambda = \frac{6\eta\omega r_{in}^2}{p_a h_0^2} \tag{3-6}$$

where r_{in} is the inner radius of the thrust air bearing. The non-dimensional form of the Reynolds equation for thrust air bearings is given as:

$$\frac{1}{R}\frac{\partial}{\partial \theta}\left[PH^3\frac{\partial P}{\partial \theta}\right] + \frac{\partial}{\partial R}\left[RPH^3\frac{\partial P}{\partial R}\right] = \Lambda R\frac{\partial}{\partial \theta}(PH) + 2\Lambda R\frac{\partial(PH)}{\partial T} \tag{3-7}$$

For grooved aerodynamic thrust bearings, the air film thickness of the bearing is expressed as:

$$H = \begin{cases} 1 + \frac{\Delta h_{incline}}{2h_0}\left(1 - \frac{r}{r_{\text{out}}}cos\theta\right) & ridge\ area \\ 1 + \frac{h_g}{h_0} + \frac{\Delta h_{incline}}{2h_0}\left(1 - \frac{r}{r_{\text{out}}}cos\theta\right) & groove\ area \end{cases} \quad (3\text{-}8)$$

where h_g is the depth of grooves, r_{out} the inner radius of the thrust air bearing, $\Delta h_{incline}$ the difference between the minimum and maximum air film thickness caused by an inclination of bearing surfaces, for perfectly parallel bearing surfaces $\Delta h_{incline} = 0$; θ the angular position in the θ-axis.

3.2.2 Modified Reynolds equation

The classical Reynolds equation was derived with the continuum no-slip boundary condition. However, if the air film thickness of the bearings is on the order of the mean free path of the air molecules, the effect of gas rarefaction cannot be ignored. Whether or not to consider the gas rarefaction effect can be decided by the Knudsen number (Kn), which is calculated as the ratio of the mean free path of the air molecules to the air film thickness. When 0.001<Kn<0.1, the first order slip boundary condition should be considered; when 0.1<Kn<10, the second-order or higher-order slip boundary condition should be considered.

The modified dimensionless Reynolds equation considering the effective viscosity and the gas rarefaction effect is listed as follows [79]:

$$\frac{1}{R}\frac{\partial}{\partial\theta}\left[\Phi_p PH^3\frac{\partial P}{\partial\theta}\right]+\frac{\partial}{\partial R}\left[\Phi_p RPH^3\frac{\partial P}{\partial R}\right]=\mathrm{f(Kn)}\Lambda\mathrm{R}\frac{\partial}{\partial\theta}(PH)+2\mathrm{f(Kn)}\Lambda\mathrm{R}\frac{\partial(PH)}{\partial T} \quad (3\text{-}9)$$

The Knudsen number *Kn* and the effective viscosity coefficient *f(Kn)* are calculated as [79]:

$$Kn=\frac{\lambda}{h} \quad (3\text{-}10)$$

$$\mathrm{f(Kn)}=\frac{1}{1+2Kn+0.2K^{\ 0.788e^{-Kn/10}}} \quad (3\text{-}11)$$

The rarefaction coefficient Φ_p is defined as [79]:

$$\Phi_p=\begin{cases}1+6Kn & First-order\ model\\ 1+6Kn+6Kn^2 & Second-order\ model\\ 1+0.10842Kn+\frac{9.3593}{Kn^{-1.17468}} & Boltzmann\ model\end{cases} \quad (3\text{-}12)$$

Assuming a small vibration of the bearing gap in an axial direction, the air film thickness, pressure and rarefaction coefficient are expressed, respectively, as follows:

$$H(r,\theta,t)=H(r,\theta)+\Delta Z\cdot e^{i\omega_p t} \quad (3\text{-}13)$$

$$P(r,\theta,t)=P(r,\theta)+P_1(r,\theta)\cdot\Delta Z\cdot e^{i\omega_p t} \quad (3\text{-}14)$$

$$\Phi_p=(\Phi_p)_0+(\frac{\partial\Phi_p}{\partial P})_0P_1(r,\theta)\Delta Ze^{i\omega_p t}+(\frac{\partial\Phi_p}{\partial H})_0\Delta Ze^{i\omega_p t} \quad (3\text{-}15)$$

where $i=\sqrt{-1}$, P_1 is the first-order pressure field. Substituting Equations (3-13)

to (3-15) into Equation (3-9), the zeroth and first-order lubrication equations are obtained in the following form [79]:

$$\frac{1}{R}\frac{\partial}{\partial\theta}\left[(\Phi_p)_0 P_0 H^3 \frac{\partial P_0}{\partial\theta}\right] + \frac{\partial}{\partial R}\left[(\Phi_p)_0 R P_0 H^3 \frac{\partial P_0}{\partial R}\right] = \mathrm{f(Kn)}\Lambda R \frac{\partial}{\partial\theta}(P_0 H) \quad (3\text{-}16)$$

$$\frac{1}{R}\frac{\partial}{\partial\theta}\left[\left((\Phi_p)_0 P_0 H^3 \frac{\partial P_1}{\partial\theta} + 3(\Phi_p)_0 P_0 H^2 \frac{\partial P_0}{\partial\theta} + (\Phi_p)_0 P_1 H^3 \frac{\partial P_0}{\partial\theta} + (\frac{\partial\Phi_p}{\partial P})_0 P_1 P_0 H^3 \frac{\partial P_0}{\partial\theta} + (\frac{\partial\Phi_p}{\partial H})_0 P_0 H^3 \frac{\partial P_0}{\partial\theta}\right)\right] + \frac{\partial}{\partial R}\left[\left((\Phi_p)_0 R P_0 H^3 \frac{\partial P_1}{\partial R} + 3(\Phi_p)_0 R P_0 H^2 \frac{\partial P_0}{\partial R} + (\Phi_p)_0 R P_1 H^3 \frac{\partial P_0}{\partial R} + \left(\frac{\partial\Phi_p}{\partial P}\right)_0 R P_1 P_0 H^3 \frac{\partial P_0}{\partial R}\right) + (\frac{\partial\Phi_p}{\partial H})_0 R P_0 H^3 \frac{\partial P_0}{\partial R}\right] = \mathrm{f(Kn)}\Lambda R \frac{\partial}{\partial\theta}(P_0 + P_1 H) + 2\mathrm{f(Kn)}\Lambda \frac{\omega_p}{\omega} R(P_0 + P_1 H)\cdot i \quad (3\text{-}17)$$

where ω_p is the perturbation frequency.

3.2.3 Numerical solution of the discretized modified Reynolds equation

The process of the discretization of the modified Reynolds equation is introduced in the Appendix. Solving the discretized equation requires defining boundary conditions. In this study, the following boundary conditions are used:

(a) The pressure at the inner and outer boundaries of the bearing is the atmospheric pressure;

(b) At recurrent boundaries, the pressure is the same;

(c) At the interfaces between groove and ridge pairs, the pressure and the flow are continuous.

With the above boundary conditions, the coefficients of Equations (3-16) and (3-17) can be obtained through an iterative method to achieve P_0 and P_1. The Newton-Raphson method is a widely used iterative method in solving Reynolds equations [3-4]. Lubrecht [135] summarized the advantages of the Newton-Raphson method in solving discretized equations as (1) small iteration numbers; (2) rapid convergence; (3) short computational times. With the consideration of the advantages mentioned above, the Newton-Raphson method is followed in this study to solve the discretized modified Reynolds equations, as derived in Algorithm 1.

Algorithm 1: The Newton-Raphson method for solving the modified Reynolds equation

Choose initial starting guess P_0, and desired maximum size ε;

for i=0,1, 2,…,do

Compute $\delta P^i = -f(P^i)/\, f'(P^i)$;

Derive new guess $P^{i+1} = P^i + \delta P^i$;

If $|\delta P^i| < \varepsilon$ then

Stop

end

end

Adopting the above-mentioned boundary conditions of thrust air bearings and using the Newton-Raphson method, the discretized Reynolds equation can be solved, and the pressure distribution within the air film can be obtained. Then, the following Equation (3-18) can be used to calculate its load capacity:

$$F = \int_{r_{\text{out}}}^{r_{\text{in}}} \int_0^{2\pi} (P_0 - 1) p_a \, r dr d\theta \tag{3-18}$$

The dynamic force coefficients are given by:

$$k + i \cdot \omega_P \cdot c = -\int_{r_{out}}^{r_{in}} \int_0^{2\pi} P_1 p_a \, r dr d\theta \tag{3-19}$$

where *k* is the dynamic stiffness coefficient and *c* the dynamic damping coefficient.

3.3 Grid independence test

The number of grids is an important factor in determining the computational time and accuracy of the simulation. Even with the simulation results ‘converged’, it is necessary to make sure that the solution is independent of the grids. Not checking this is a common cause of erroneous results in CFD. A coarse mesh could lead to a larger spatial discretization. However, when the number of grids is too large, the simulation process would be time-consuming. Therefore, the grid independence test is necessary to find a grid number which could ensure the

accuracy of the simulation while reducing the simulation time.

In this section, a spiral-grooved aerodynamic thrust bearing, its design and operating parameters listed in Table 3-1, is used to illustrate the process of the grid independence test. For evaluating the mesh grid number, different scales of mesh grids are adopted to calculate the load capacity of the bearing, and the results of the corresponding load capacity and simulation time are compared in Table 3-2. Here, a non-inclined air film is considered in all the simulation.

Table 3-1: Design parameters and operating conditions of the spiral-grooved aerodynamic thrust bearing

Parameters	Values
Inner radius r_1 (mm)	6
Outer radius r_2 (mm)	15
Depth of grooves h_g (μm)	15
Air film thickness h_0 (μm)	10
The ratio of groove width to ridge width w_{gr}	1
Spiral angle α (degree)	15
Number of grooves N	11
Rotating speed ω (rpm)	80,000

Table 3-2: The load capacity and simulation time of different mesh grid numbers

Mesh grid numbers	Load capacity (N)	Computational time (s)
23 x 45	1.84	6.22
34 x 67	2.09	14.85
45 x 89	2.17	25.00
56 x 111	2.20	41.13
78 x 155	2.23	122.98
100 x 199	2.24	313.51
133 x 265	2.24	968.61

From Table 3-2, it can be seen that the effect of the mesh grid numbers on the bearing load capacity is low, which means the developed model is independent of the mesh grid numbers. However, the effect of the mesh grid numbers on the simulation time is huge, ranging from 6.22 seconds to 968.61 seconds. Based on the results, for this case, the mesh grid numbers of 78 x 155 are determined as the optimal grid numbers, since they could ensure the accuracy of the simulation while maintaining a reasonable simulation time. In this study, the grid independence test is carried out once for each type of bearing to find the optimal mesh grid numbers. Then, the mesh grid numbers are always set as the optimal mesh grid numbers in all the following simulations. In this way, the accuracy of

the CFD model can be ensured, and the simulation time can be saved.

3.4 Validation of the developed CFD model against published results

3.4.1 Verification of the load capacity's calculation – Case 1

To examine the accuracy of the developed CFD model in calculating the load capacity, the bearing geometry and working parameters published by Waumans et al. [136], as shown in Figure 3-1 and Table 3-3, are simulated using the model. Since Waumans et al. [136] did not consider the inclination of the air film, a non-inclined air film is used in the present simulation for effective comparison purposes. The results are compared with the simulation and experimental results given by Waumans et al. [136] in Figure 3-2.

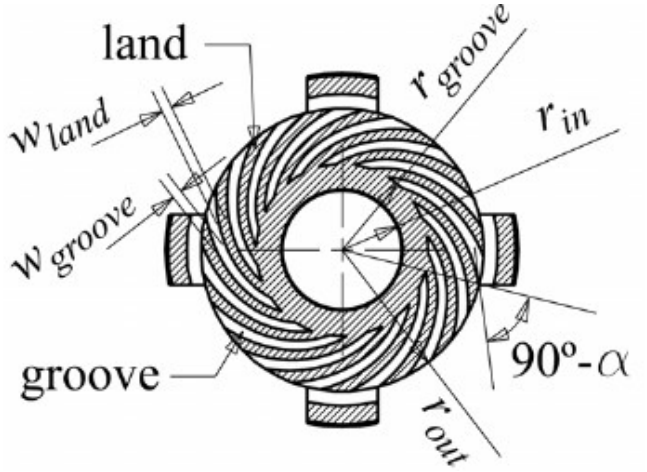


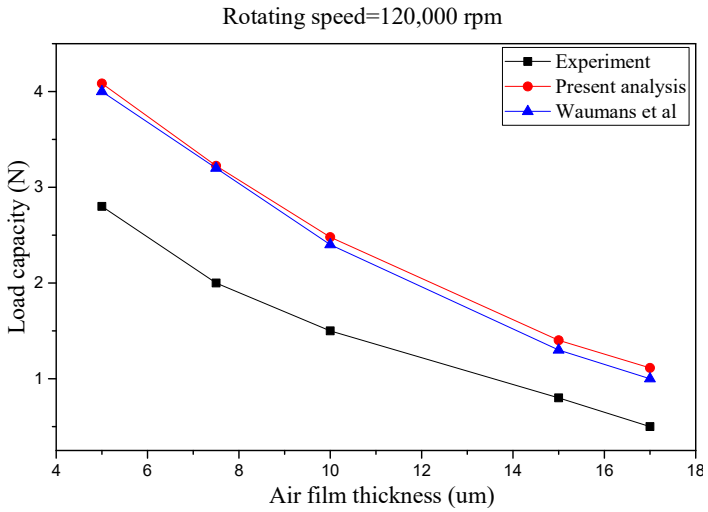
Figure 3-1: Bearing geometry in the work of Waumans et al. [136]. Same geometry is used in Case 1 to verify the developed CFD model.

Table 3-3: Geometrical parameter values of the spiral-grooved bearing in the work of Waumans et al. [136]

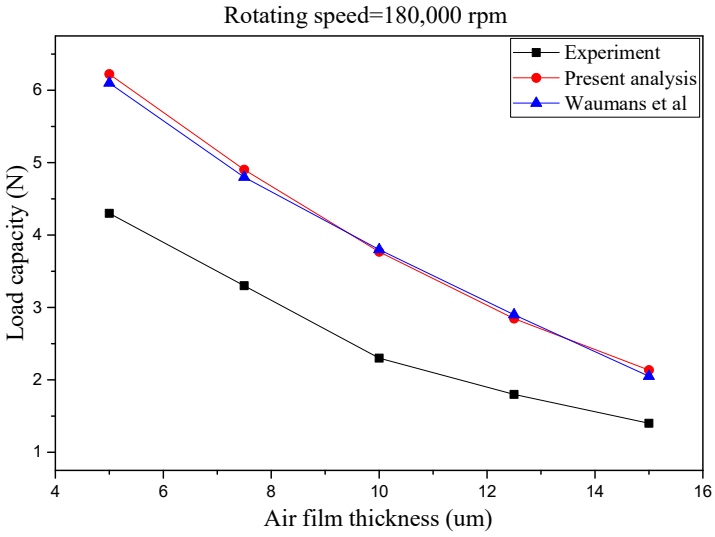
Geometry parameter	Value
r_{in} (mm)	4.25
r_{out} (mm)	10
r_{groove} (mm)	6
α (degree)	25
h_g (μm)	45
$W_{groove}/(W_{land}+ W_{groove})$	0.5
N	15

Figure 3-2 compares the simulation results obtained by the developed model and

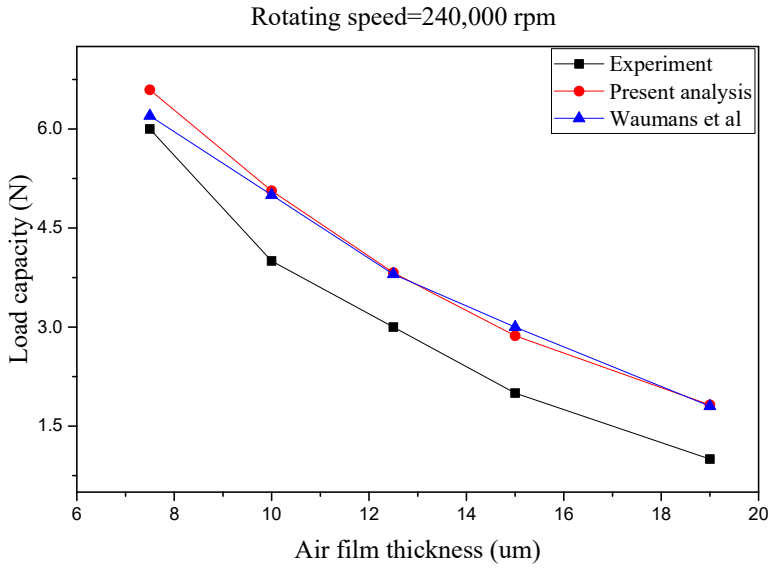
the simulation and experimental results presented in the work of Waumans et al. [136]. It can be seen that the model's simulation results are very close to their simulation results in all the simulated working conditions; while both of them show a reasonable agreement with their experimental results. The accuracy of the developed CFD model in calculating the load capacity of grooved aerodynamic thrust bearings has thus been verified.



(a)



(b)



(c)

Figure 3-2: Verification of the developed model against the results of Waumans et al. [136]: (a) at 120,000 rpm; (b) at 180,000 rpm; and (c) at 240,000 rpm.

Waumans et al. [136] explained the difference between the simulation and experimental results as a result of (1) deformation of the rotating disc caused by centrifugal forces; (2) variation of the length of the shaft caused by Poisson effect; (3) alignment and surface imperfections of bearing components.

3.4.2 Verification of the load capacity's calculation - Case 2

To further examine the developed CFD model, a bearing's working parameters in the work of Hashimoto and Namba [97], shown in Table 3-4, are also simulated using the developed model. A non-inclined air film is considered in both simulations. The results are compared in Figure 3-3. It can be found that the

pressure distribution obtained by the developed CFD model and in the work of Hashimoto and Namba [97] are very similar. In particular, the maximum and minimum pressure of the two simulation results are both very close, as well as the load capacity.

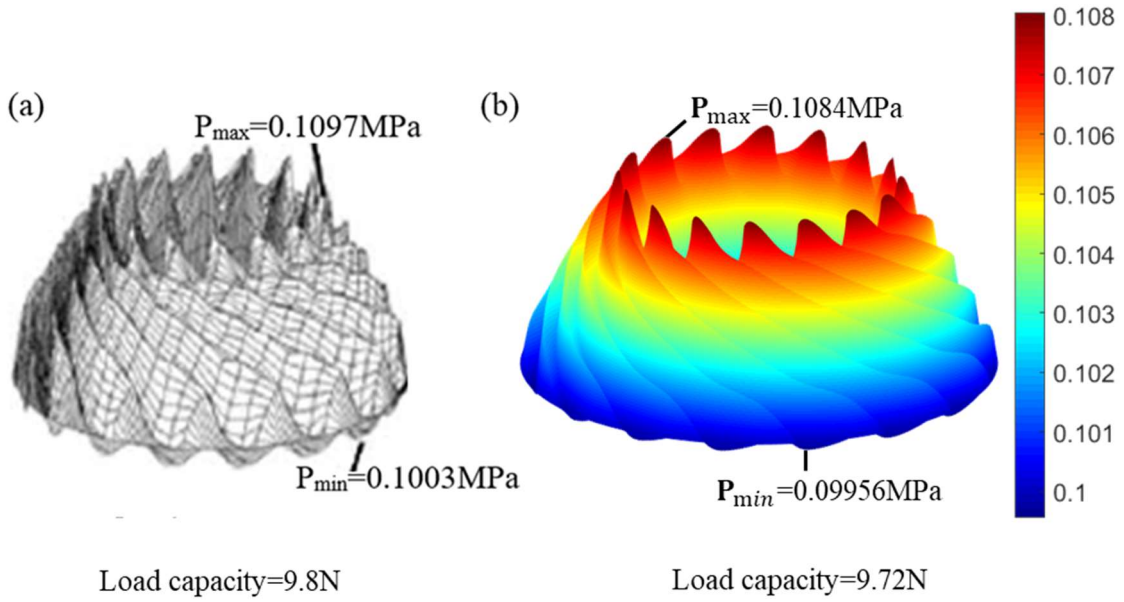


Figure 3-3: The simulation results of (a) Hashimoto and Namba [97], and (b) the developed CFD model at 40,000 rpm under an air film thickness of 22.6 μm. The two results are very similar in terms of the pressure distribution, load capacity, maximum and minimum pressure; which proves the accuracy of the developed CFD model.

Table 3-4: Prescribed variables and constraints in the work of Hashimoto and Namba [97]

Geometry parameter	Value
r_{in} (mm)	12.8
r_{out} (mm)	32
r_{groove} (mm)	18.56
α (degree)	18
h_g (μm)	20
$W_{groove}/(W_{land}+ W_{groove})$	0.636
N	16

In summary, two cases are presented here to validate the developed model in load capacity's calculation under various bearing dimensions and working conditions. From the comparisons in Case 1 and Case 2, it can be concluded that the developed CFD model is solving the Reynolds equation satisfactorily and that a reasonable agreement with experimental results in terms of the load capacity could, in general, be expected.

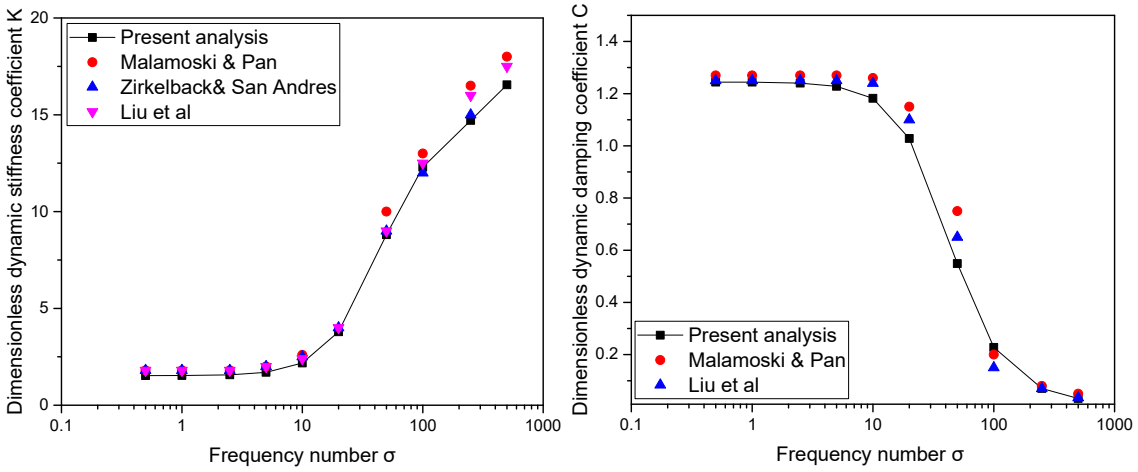
3.4.3 Verification of dynamic force coefficients' calculation - Case 3

The results obtained from Malanoski and Pan [54], Zirkelback and San Andres [137] and Liu et al. [138] for spiral-grooved aerodynamic thrust bearings are compared with the simulation results of the developed CFD model to examine the accuracy of the developed model in simulating the dynamic stiffness coefficient and damping coefficient. The original data in this calculation are listed in Table 3-5. A non-inclined air film is considered in all the simulations.

Table 3-5: Prescribed variables and constraints in the work of Malanoski and Pan [54], Zirkelback and San Andres [137] and Liu et al. [138]

Geometry parameter	Value
r_{in}/r_{out}	0.4
r_{groove}/r_{out}	0.56
α (degree)	18.8
h_g/h_o	3.05
$W_{groove}/(W_{land}+ W_{groove})$	0.6587
Λ	2
N	12

The comparison results are shown in Figure 3-4. Here, the frequency number $\sigma = 2\Lambda\frac{\omega_p}{\omega}$. From Figure 3-4, the present analysis agrees quite well with the available results, validating the developed model in calculating the dynamic stiffness coefficient and damping coefficient.



(a) (b)

Figure 3-4: Verification against the results of Malanoski and Pan [54], Zirkelback and San Andres [137] and Liu et.al [138]: (a) dimensionless dynamic stiffness coefficient, and (b) dimensionless dynamic damping coefficient. The results of the present analysis match very well with the others' simulation results, which verifies the accuracy of the developed CFD model.

3.4.4 Verification of dynamic force coefficients' calculation - Case 4

To further examine the performance of the developed CFD model in dynamic force coefficients' calculation, the simulation results of Faria [139] for a spiral-grooved gas seal are also used for comparison. The original data in this calculation are listed in Table 3-6.

Table 3-6: Prescribed variables and constraints in the work of Faria [139]

Geometry parameter	Value
r_{in} (mm)	71.12
r_{out} (mm)	88.9
r_{groove} (mm)	76.454
P_{in} (bar)	1
P_{out}(bar)	5
α (degree)	20
h_g (μm)	2.54
h_0 (μm)	2.54
$W_{groove}/(W_{land}+ W_{groove})$	0.5
N	12

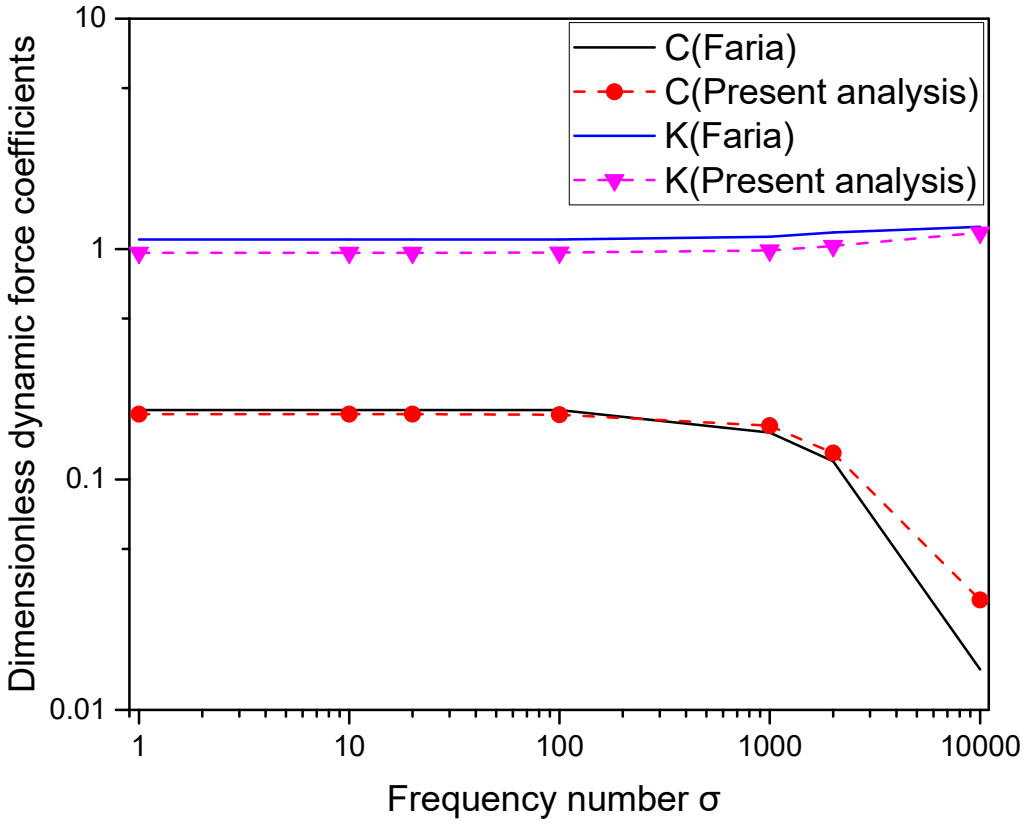


Figure 3-5: Comparison with the results of Faria [139]: dimensionless dynamic stiffness coefficient and damping coefficient against various frequency number (Λ=1253)

The comparison results are shown in Figure 3-5 where a non-inclined air film is considered in both simulations. These comparisons validate the developed model further.

In summary, two cases are presented here to validate the developed model in dynamic force coefficients' calculation under various bearing dimensions and working conditions. From the comparison in Case 3 and Case 4, it can be

concluded that the developed CFD model can achieve satisfactory accuracy in calculating the dynamic force coefficients of grooved aerodynamic thrust bearings.

3.5 Summary

This chapter presents the CFD modelling and validation processes of grooved aerodynamic thrust bearings. The CFD model is developed with reference to Dr Guang Pu's code in grooved aerodynamic journal bearings [130]. With reference to Dr Guang's model, the author developed and validated the CFD model for grooved aerodynamic thrust bearings and embed the developed model into biomimetic and optimisation design algorithms independently. The developed model is based on FDM and FVM analysis and can be used to calculate the load capacity, dynamic stiffness and damping coefficients of the grooved aerodynamic thrust bearings. A grid independence check is conducted before each study to find the optimal mesh grid size for ensuring the accuracy of simulation while saving computational time. The simulation results obtained by the developed model were proven to show good agreement with those published in the literature for load capacity, dynamic stiffness and damping coefficients; this validates the accuracy of the developed CFD model.

The CFD model is developed in a MATLAB environment, rather than other commercial CFD simulation software like ANSYS Fluent, since this allows the feasibility to integrate into the model other optimisation techniques. Such approaches will be presented in Chapters 5 and 6, where the CFD model is integrated into optimisation techniques to improve the load capacity of conventional grooved aerodynamic thrust bearings.

CHAPTER 4 A DRAGONFLY WING INSPIRED BIOMIMETIC AERODYNAMIC THRUST BEARING

4.1 Introduction

This chapter investigates the potential of the micro surface structures of dragonfly wings for generating a load capacity in aerodynamic bearings. The topography of micro surface structures of dragonfly wings is analysed, and five most representative geometries are extracted before being applied onto thrust bearings for performance evaluation. Based on the CFD model developed in Chapter 3, the load capacity of biomimetic models under various velocities and flow angles are compared, and the best geometry and velocity angle is taken to design the biomimetic bearing.

A grooved aerodynamic thrust bearing test rig is developed from scratch to compare the load capacity of an optimised conventional spiral-grooved bearing and the biomimetic bearing. The configuration of the test rig, the procedures to measure the load capacity of test bearings, and the instrumentation of the test rig

are introduced, after which experimental results are given to show the effectiveness of the proposed biomimetic design method.

The rest of this chapter is organized as follows: section 4.2 demonstrates the specific background and motivations of this study; section 4.3 illustrates the biomimetic feature extraction process; section 4.4 introduces the biomimetic surface models of dragonfly wings; section 4.5 presents a theoretical comparison between the biomimetic and conventional spiral-grooved bearings; section 4.6 presents the experimental verification process; the summary is presented in section 4.7. A version of this study has been accepted for publication in International Journal of Mechanical Science.

4.2 Background and motivations

Biomimetic designs have been widely used in fluid-film lubrications. The John Crane Corporation designed dry gas seals with a biomimetic groove inspired by bird wings. They concluded that the biomimetic groove leads to a stiffer gas film compared to the conventional spiral groove [127]. Peng et al. [128] concluded that the outline of bird wings has a specific correlation with the groove pattern of dry gas seals. Gao et al. [129] presented a biomimetic aerostatic bearing which is inspired by the wings of long-eared owls. Compared to the conventional

aerostatic bearing, the biomimetic one requires a 27% less supplier pressure. However, although the biomimetic design has been successfully applied in aerostatic bearings and dry gas seals, it has not been applied to design aerodynamic bearings before this study.

Bird wings are proved to be important biomimetic samples for fluid-film lubrication [112,113,114]. However, birds bend their wings heavily to hold air and produce thrust during flying to exploit the profound effect of wing morphology on aerodynamic performance, as shown in Figure 4-1(a), while surfaces of bearings/gas seals remain flat during the operation. Different from birds, wings of dragonflies are formed with flexible membranes without muscles. They cannot bend heavily like birds to hold air in downwards beats to produce lift, as shown in Figure 4-1(b). However, they can still hover and stay in the air by flapping wings, which is very likely to be contributed to their surface structures. Therefore, surface structures of dragonfly wings might be important biomimetic samples for aerodynamic bearings for generating high load capacity. Therefore, this study is set out to explore the potential of the micro surface structures of dragonfly wings in designing biomimetic aerodynamic bearings.



Figure 4-1: The comparison between the wing morphology of a bird and a dragonfly in flight. Different with bird wings, dragonfly wings cannot bend heavily to hold air and produce thrust during flying. Their high lifting capacity is very likely to be contributed to their surface structures.

4.3 Biomimetic features extraction

The wing of a dragonfly is constructed from a series of very lightweight skins with a very large number of the small quadrilateral, pentagonal and hexagon grid

structures, known as cells or cellulose, as presented in Figure 4-2(a). From Figure 4-2(a), it can be found that in different parts of dragonfly wings, the forms of cells are different. In the region which is near the costal margin, wing cells are generally quadrilateral grids. The two rows of quadrilateral grids which are formed by the costal margin, the subcostal margin and the radial vein R1 are covered from the root to the tip of the wing. In the region which is near the tip or the postal vein margin of the wing, wing cells are generally hexagon grids and pentagonal grids.

The surface structures of dragonfly wings are observed using the Alicona's high-resolution 3D measurement system to extract biomimetic models for bearings [140]. Test samples (as shown in Figure 4-2(a)) are taken from wings of dragonflies bought online [141] and are well-preserved in a container with room humidity and temperature. The grids morphologies of dragonfly wings are complex. After analysis, the top five representative geometries are extracted from different areas of a dragonfly wing, as shown in Figure 4-2(b). They are aligned quadrilateral, staggered quadrilateral, aligned pentagonal, staggered pentagonal and hexagonal grids. In particular, the dimensions of aligned quadrilateral grids in Region 1 are measured using the Alicona's high-resolution 3D measurement system. Examples of the Alicona's measuring results are shown in Figure 4-3. The length and width of corresponding longitudinal veins, the length and width of corresponding cross-veins, and the depth of grids in Region 1 of the wing

samples are measured. Five pieces of dragonfly wing samples are measured in this section, and for each sample, 4 grids in Region 1 are measured. It is found that the differences in the dimensions of measured grids are not large, and thus the average value of the dimensions has a certain degree of representativeness.

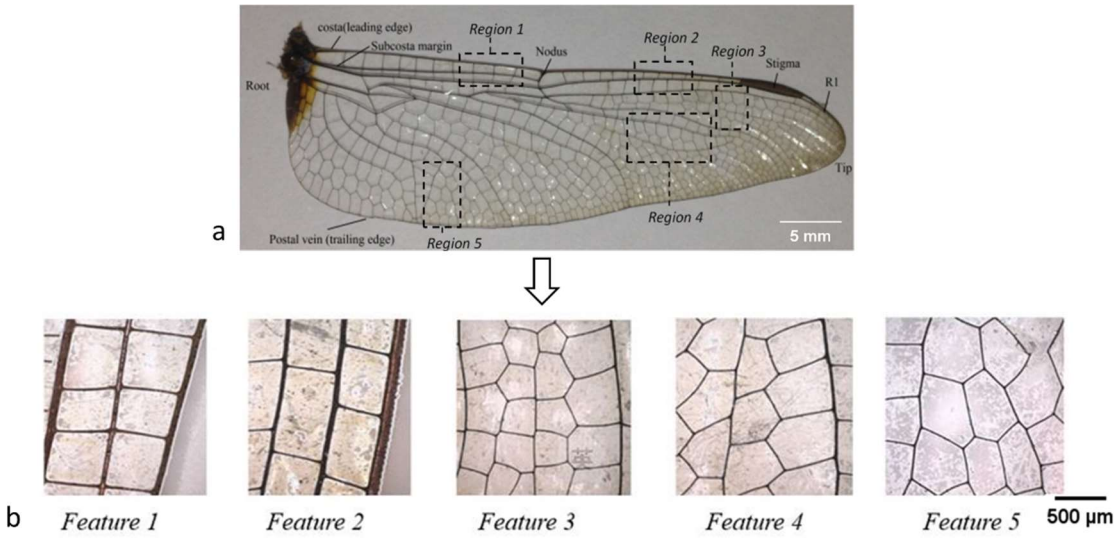
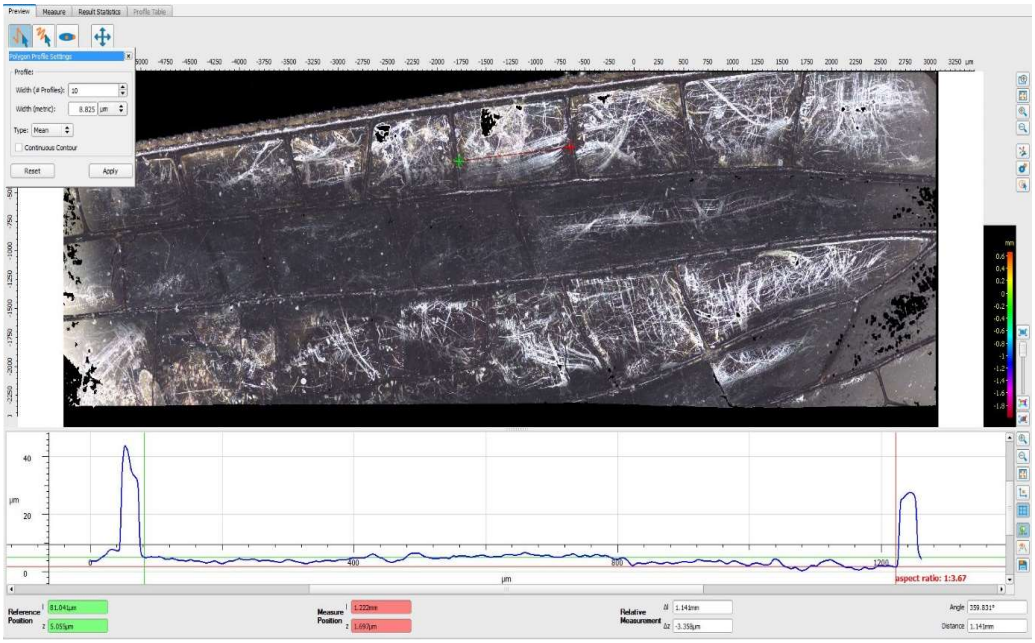


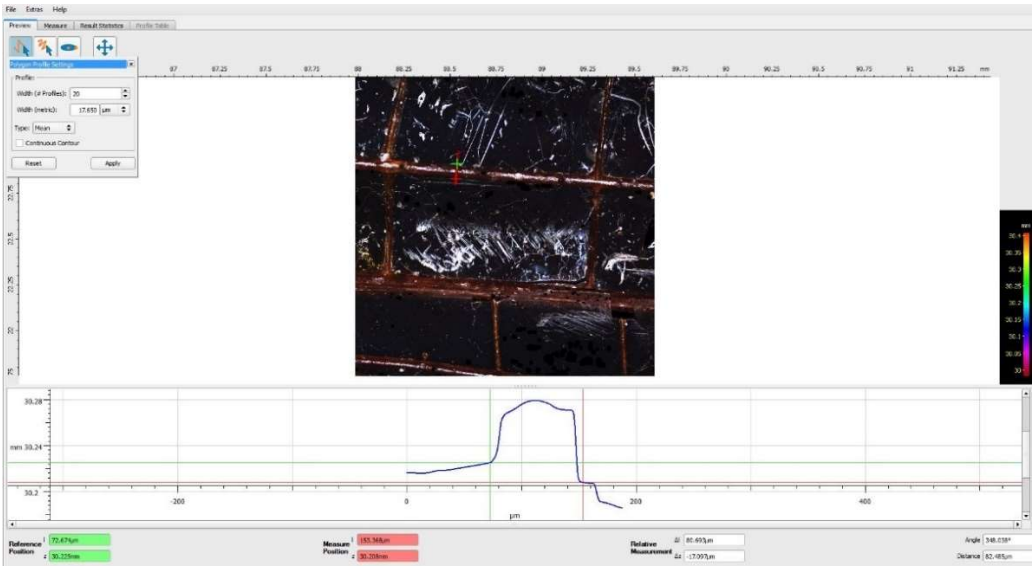
Figure 4-2: The grids morphologies of dragonfly wings: (a) the testing sample of a dragonfly wing; (b) top five representative geometries after imaging with ×5 magnification.

In this study, the average value of depths of grids D_a is calculated as 35 μm, the average value of lengths of corresponding longitudinal veins L is calculated as 1055 μm, the average value of widths of corresponding longitudinal veins T_L is calculated as 90 μm, the average value of lengths of corresponding cross veins W is calculated as 449 μm, and the average value of widths of corresponding cross veins T_C is calculated as 66 μm. The obtained data are going to be used to

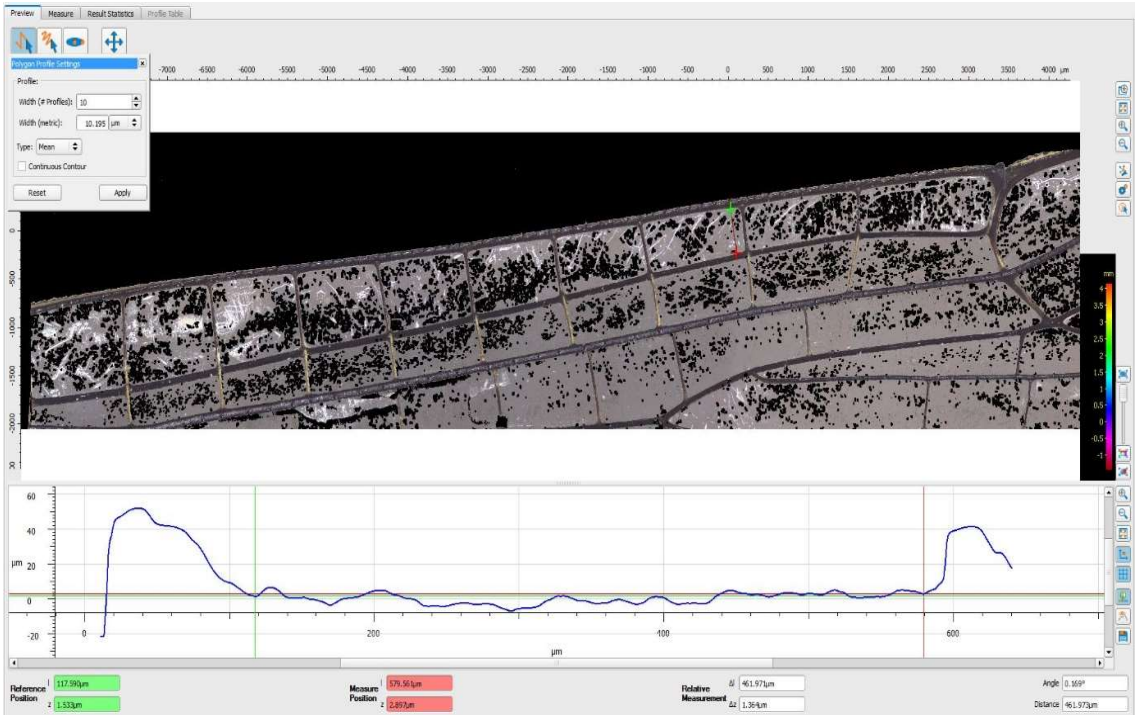
design biomimetic models in the following chapters.



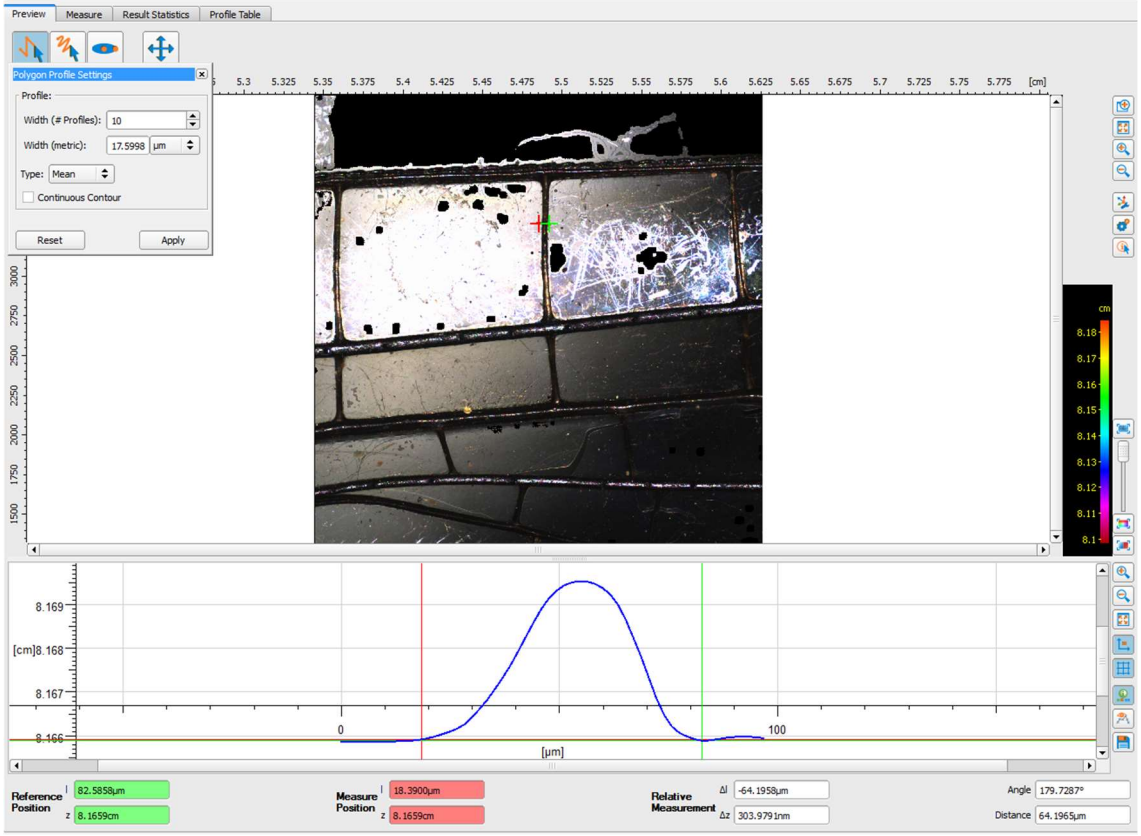
(a)



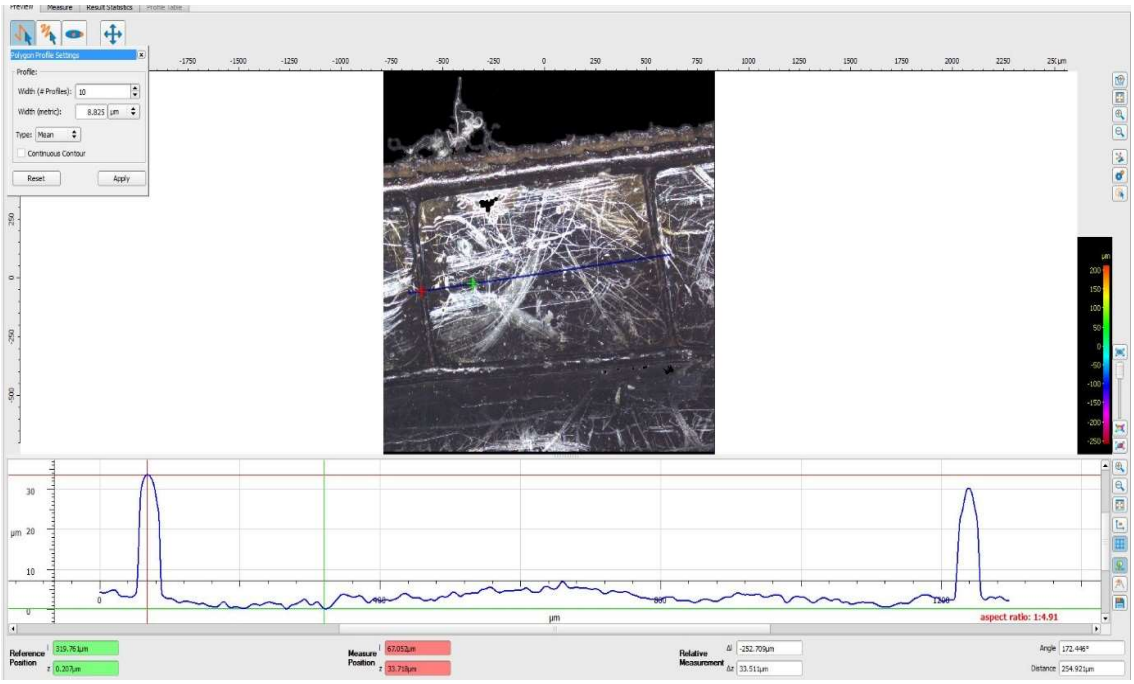
(b)


Preview
Measure
Result Statistics
Profile Table
Polygon Profile Settings
Profile:
Width (# Profiles): 10
Width (metric): 10.195 µm
Type: Mean
Continuous Contour
Reset
Apply
µm
Reference Position
Measure Position
Relative Measurement
Angle
Distance

(c)


Preview
Measure
Result Statistics
Profile Table
Polygon Profile Settings
Profile:
Width (# Profiles): 10
Width (metric): 17.5998 µm
Type: Mean
Continuous Contour
Reset
Apply
[cm]
[µm]
Reference Position
82.5858µm
8.1659cm
Measure Position
18.3900µm
8.1659cm
Relative Measurement
-64.1958µm
303.9791nm
Angle
179.7287°
Distance
64.1965µm

(d)



(e)

Figure 4-3: An example of measuring results of an aligned quadrilateral grid of a dragonfly wing: (a) length of a longitudinal vein; (b) width of a longitudinal vein; (c) length of a cross vein; (d) width of a cross vein; (e) depth of a grid

4.4 Biomimetic model design

To find out whether micro-grids structures of dragonfly wings could be important biomimetic samples for air bearing applications, firstly, five biomimetic models are designed based on the measuring results in section 4.3. The extracted biomimetic models are shown in Figure 4-4. The dimensions of Models 2 to 5 are designed according to the dimensions of Model 1 since each model needs to keep the

same number of grids in the same area for effective comparison purposes. Since the direction of the velocity would change during the flying of the dragonflies, the angle of the flow velocity is set as changeable and represented by β. Then, five extracted models are simulated under a 10 μm air film and a velocity of 15 m/s and 120 m/s respectively, to find whether it can produce a load capacity. The air film thickness in the different area of the models is defined by Equation (4-1).

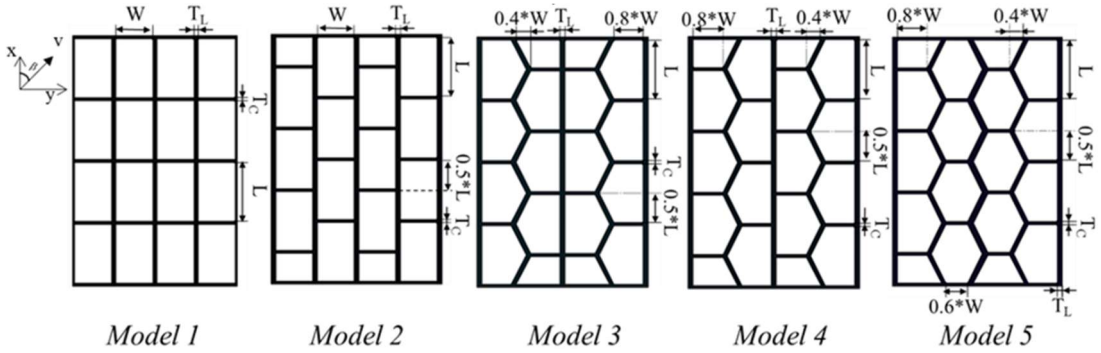


Figure 4-4: Five biomimetic models inspired by dragonfly wings. Here, the veins are mimicked by black areas, while the membranes are mimicked by the white.

$$h = \begin{cases} h_0 & areas\ of\ veins\ (black\ areas) \\ h_0 + D_a & areas\ of\ membranes\ (white\ areas) \end{cases} \quad (4\text{-}1)$$

The simulation results are shown in Figure 4-5. From Figure 4-5, it can be seen that all the five types of micro surface structures can produce a load capacity at both the studied speeds, in particular, when speeds increased to 120 m/s, the load capacity produced by all the five types of micro surface structures increased

by a large amount. Therefore, it can be concluded that it is promising to design biomimetic bearings by mimicking the micro surface structures of dragonfly wings. Besides, from Figure 4-5, it can be found that with a velocity angle of 90°, Model 3 (aligned pentagonal micro-grids) achieves the highest load capacity among all the studied models for both speeds.

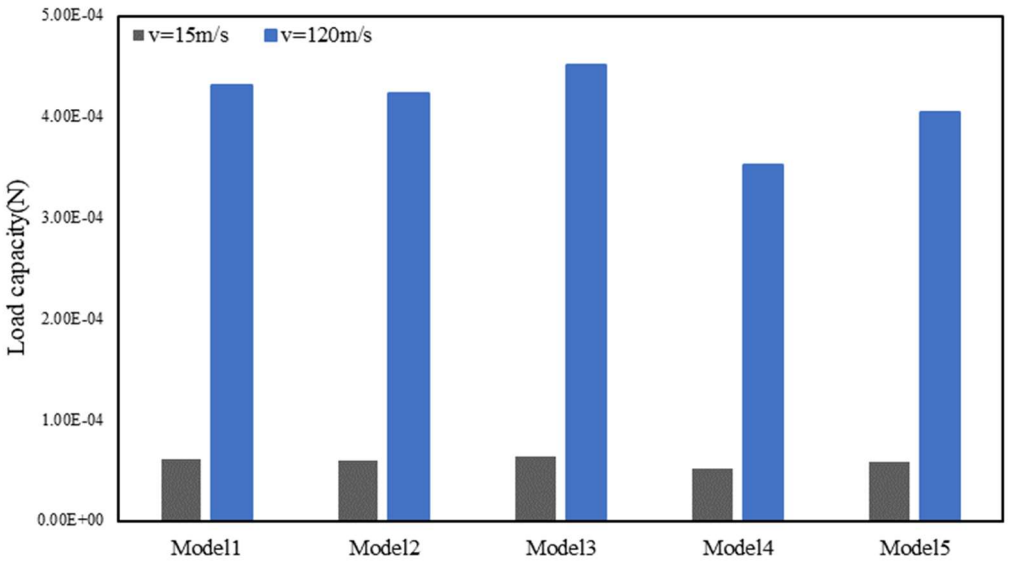


Figure 4-5: The load capacity of Models 1 - 5 with a velocity angle of 90°

Then, the influence of the velocity angle β is also investigated at a constant velocity of 120 m/s. The results are shown in Figure 4-6, from which it can be seen that for all the five types of micro-grids, the velocity angle β has an obvious effect on the load capacity. There is an optimum velocity angle that can achieve the highest load capacity, which is around 50° to 70° and various with the type of models. Also, it can be concluded that among all the five types of biomimetic

models, Model 1, which corresponding to aligned quadrilateral grids, produces the maximum load capacity with a velocity angle of 60°.

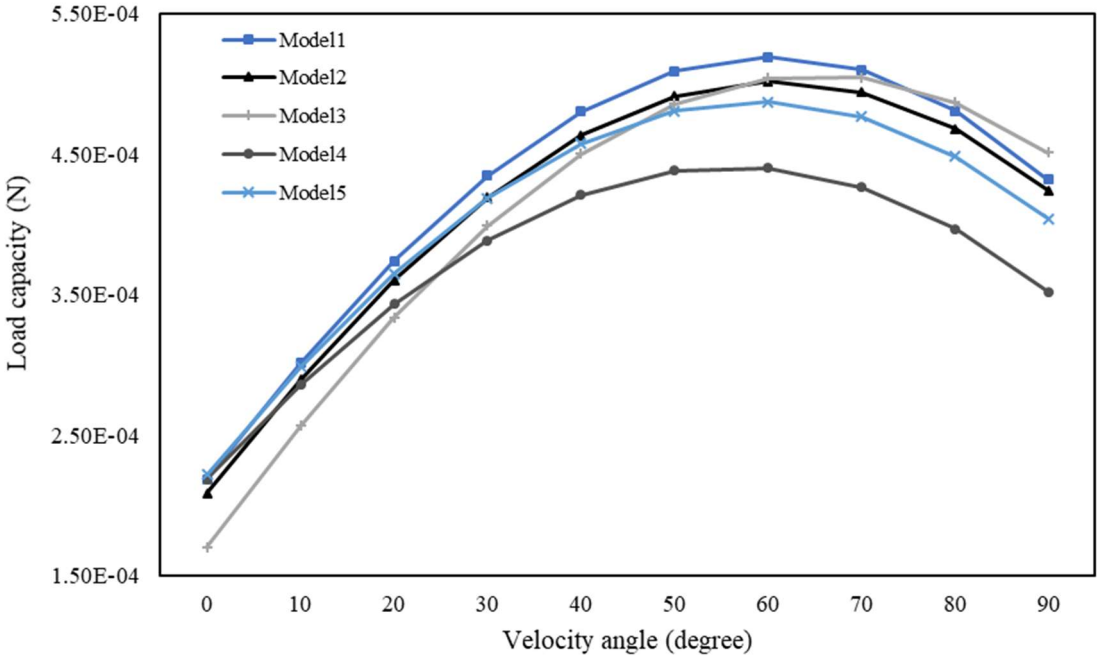


Figure 4-6: The load capacity of Models 1 - 5 against various velocity angles. The value of the velocity is fixed as 120 m/s.

However, the surface of thrust air bearings is round, while the surface of dragonfly wings is more like a rectangle. Models 1 – 5 are thus modified to Models 1a – 5a to suit annular arrangement, as shown in Figure 4-7. Since the direction of velocity is fixed when a thrust bearing is rotating, for Models 1a – 5a, β is changed by adjusting the direction of longer edges of the model. For a circular surface, the length of a grid in the θ coordinate is the arc length. In Model 1a, all the grids are designed to have a same central angle $\theta_W = W/r_{in}$, and all the distances between

the neighbored edges of grids are designed to have a same central angle $\theta_L = T_L/r_{in}$, where r_{in} is the inner radius of the model, to simplify the simulation and machining process while keeping its essential functionalities. The air film thickness in the different area of Models 1a – 5a is formulated by Equation (4-1).

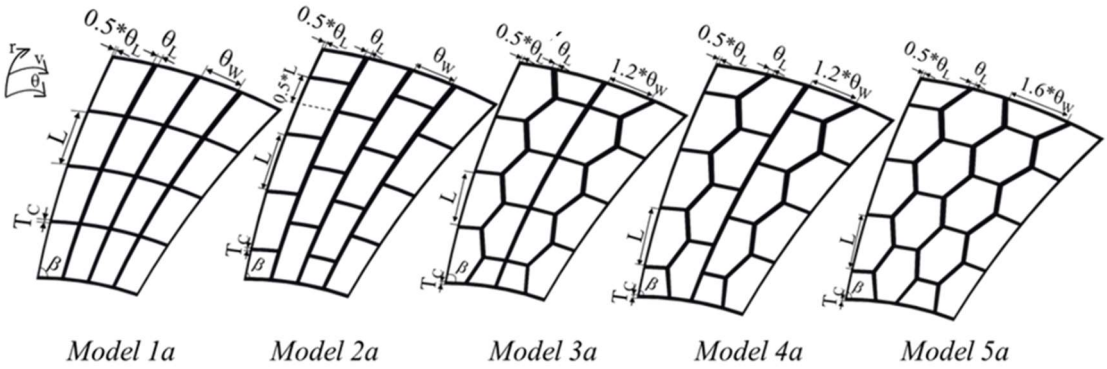


Figure 4-7: Models 1a - 5a are developed for a circular surface. Here, the veins are mimicked by black areas, while the membranes are mimicked by the white.

To find the optimum combination of the model type and the velocity angle for thrust air bearing, Models 1a – 5a are simulated against various velocity angles under an air film thickness of 10 μm, an inner radius of 6 mm, and a rotating speed of 90,000 rpm. The results are shown in Figure 4-8, from which it can be seen that for all the biomimetic models, when longer edges have an angle with the velocity, instead of being vertical to it, a higher load capacity can be achieved. In particular, Model 1a, which corresponding to aligned quadrilateral grids, generates the maximum load capacity with a velocity angle of 24°.

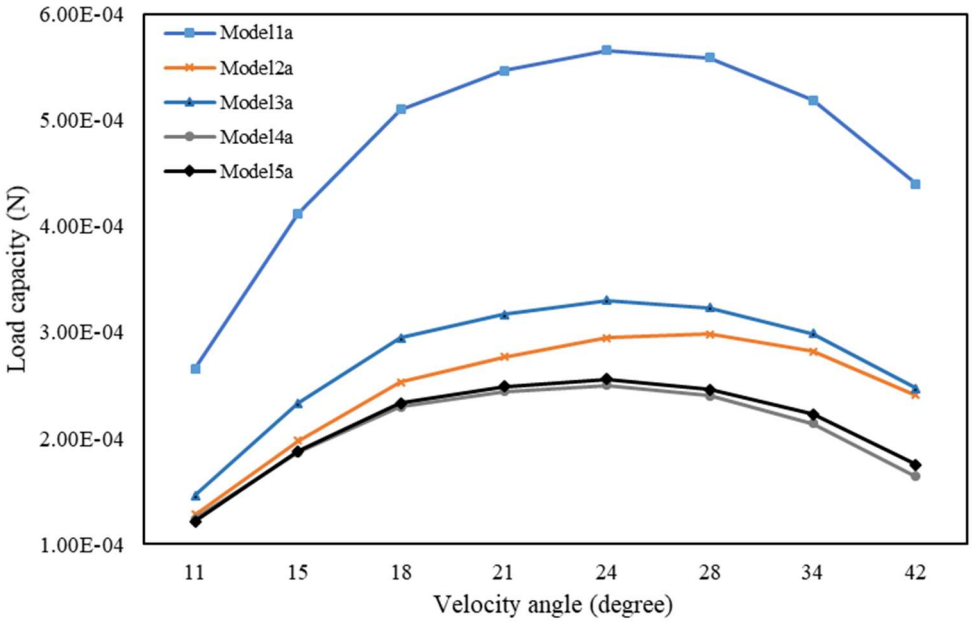


Figure 4-8: The load capacity of Models 1a - 5a against various velocity angles and a fixed rotating speed of 90,000rpm

Therefore, after the above analysis, it can be concluded that it is promising to design biomimetic bearings by mimicking dragonfly wing's micro surface structures, and for thrust bearing designing, it is the aligned quadrilateral grids with a velocity angle of 24° that could achieve the highest load capacity.

4.5 Biomimetic bearing design

Based on the finding in section 4.4 that aligned quadrilateral micro-grids generate the highest load capacity with a β of 24° for a circular surface, a novel biomimetic bearing is designed and presented in Figure 4-9(a). The inner and outer radius

of the bearing is 6 mm and 15 mm respectively. The depth of grids is 35 μm, and the air film thickness is 10 μm. The working conditions and design parameters of the biomimetic bearing are listed in Table 4-1. In this study, the air film thickness of all the designed bearings is set as 10 μm to observe an obvious load capacity while ensuring a safety operation without direct contact of the bearing surfaces.

Table 4-1: Working conditions and design parameters of the studied bearings

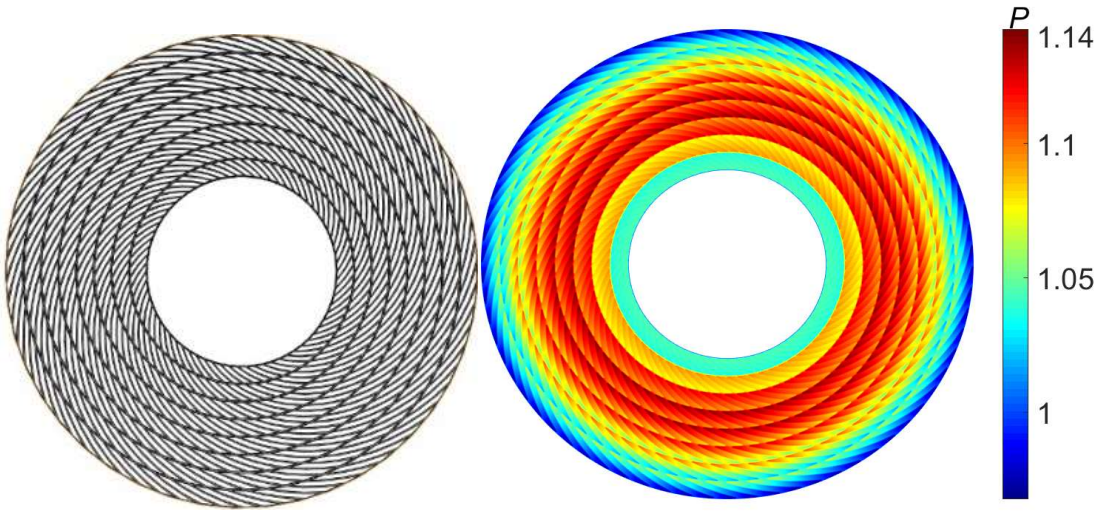
Parameters	Biomimetic bearing	Optimised spiral-grooved bearing	Reference spiral-grooved bearing
Inner radius r_1 (mm)	6	6	6
Outer radius r_2 (mm)	15	15	15
Groove/grid depth h_g (μm)	35	25	35
Air film thickness h_0 (μm)	10	10	10
The ratio of groove width to ridge width w_{gr} (or θ_w/θ_L)	5	1	5
Spiral (or velocity) angle α (or β) (degree)	24	15	24
Number of grooves N_g (or number of grids in the circumferential direction)	70	15	70
Rotating speed ω (rpm)	90,000	90,000	90,000

A conventional spiral-grooved bearing is also designed for comparison. It has 15 grooves, each in 15^{o} angle with the tangential line, a ratio of groove width to ridge width of 1, and a depth of grooves of 25 μm [125,126,127], as depicted in Figure 4-9(b) and Table 4-1. The load capacity and the dimensionless pressure distribution of the two bearings are compared by the CFD model developed in Chapter 3 at 90,000 rpm. In each modelling process, grid independence test is conducted to ensure that the results are independent of the mesh grids.

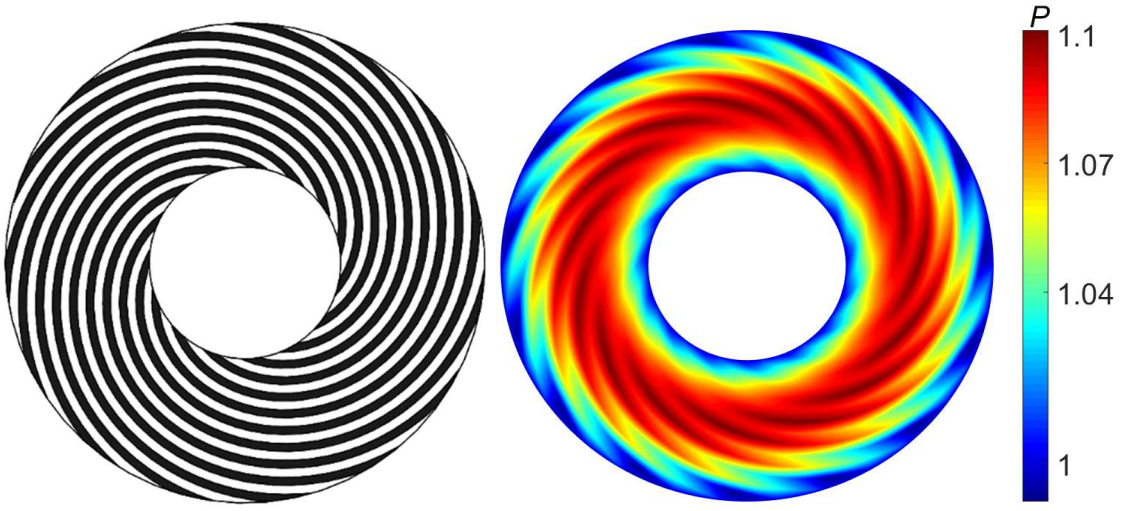
The load capacity of the biomimetic bearing and the optimised spiral-grooved bearing is simulated as 4.59 N and 3.48 N respectively. Thus, it can be concluded that the biomimetic bearing generated a 31.90% higher load capacity compared to the widely used optimised spiral-grooved bearing. A reference spiral-grooved bearing is designed to find out whether the improved load capacity is caused by densified features and a different depth of grooves. It has 70 spiral grooves, a groove angle of 240, and a depth of grooves of 35 μm (Figure 4-9(c) and Table 4-1). At the same working conditions, the load capacity of the reference bearing is simulated as 2.99 N.

The dimensionless pressure distribution of all the studied bearings is also shown in Figure 4-9. It can be found that among all the studied bearings, the biomimetic bearing achieves the highest maximum pressure, followed by the optimised

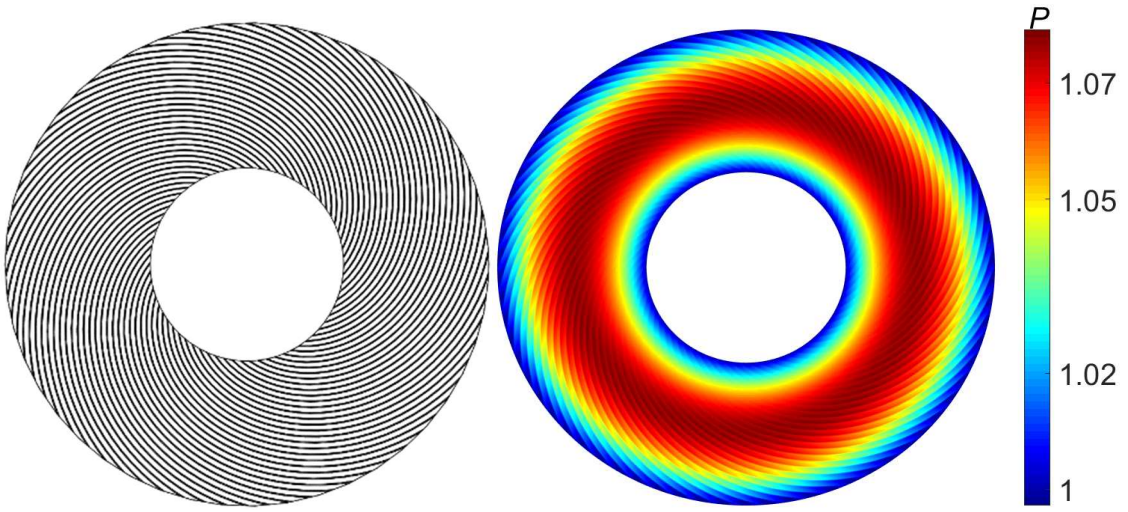
spiral-grooved bearing, while the reference spiral-grooved bearing produces the lowest maximum pressure. Therefore, the increased load capacity of the biomimetic surface can be attributed to the characteristics of the micro surface structures of dragonfly wings.



(a)



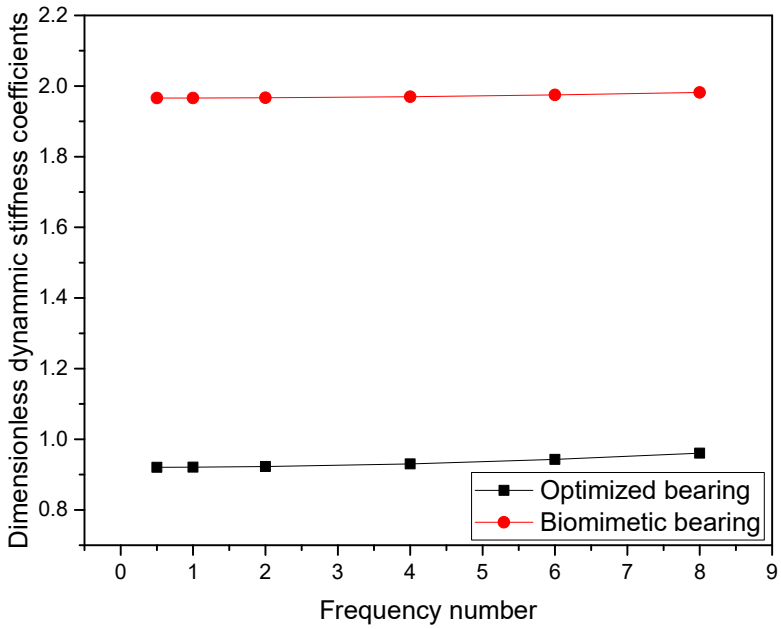
(b)



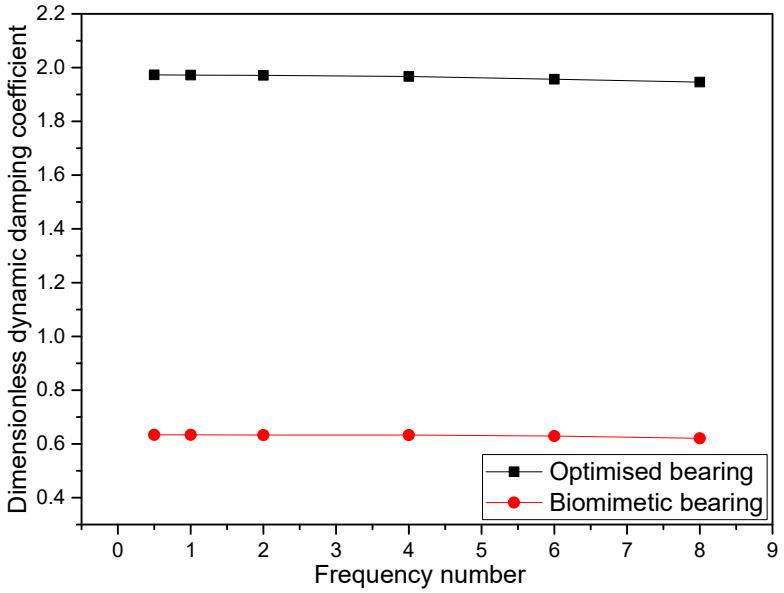
(c)

Figure 4-9: The geometry (left side) and dimensionless pressure distribution (right side) of (a) the biomimetic bearing; (b) the optimised spiral-grooved bearing; and (c) the reference spiral-grooved bearing.

The dynamic stiffness and damping coefficients of the biomimetic bearing and optimised spiral-grooved bearing have also been simulated under various frequency number, as shown in Figure 4-10. From Figure 4-10, it can be found the biomimetic bearing can achieve a higher dynamic stiffness coefficient than the optimised spiral-grooved bearing, but it has a lower dynamic damping coefficient.



(a)



(b)

Figure 4-10: Dynamic performance of the biomimetic and optimised bearing against various frequency number: (a) the dynamic stiffness coefficients and (b) the dynamic damping coefficients

4.6 Experimental Verifications

4.6.1 Test rig description

A test rig for grooved aerodynamic thrust bearings is constructed to verify the proposed biomimetic design method, as shown in Figure 4-11. Regarding Figure 4-11, it is composed of a high-speed motor system, a micrometre stage, an adjustable mount, a shoulder, test bearings, and two force sensors. The function of each component is described in Table 4-2 with the flow sequence referred to in Figure 4-11.

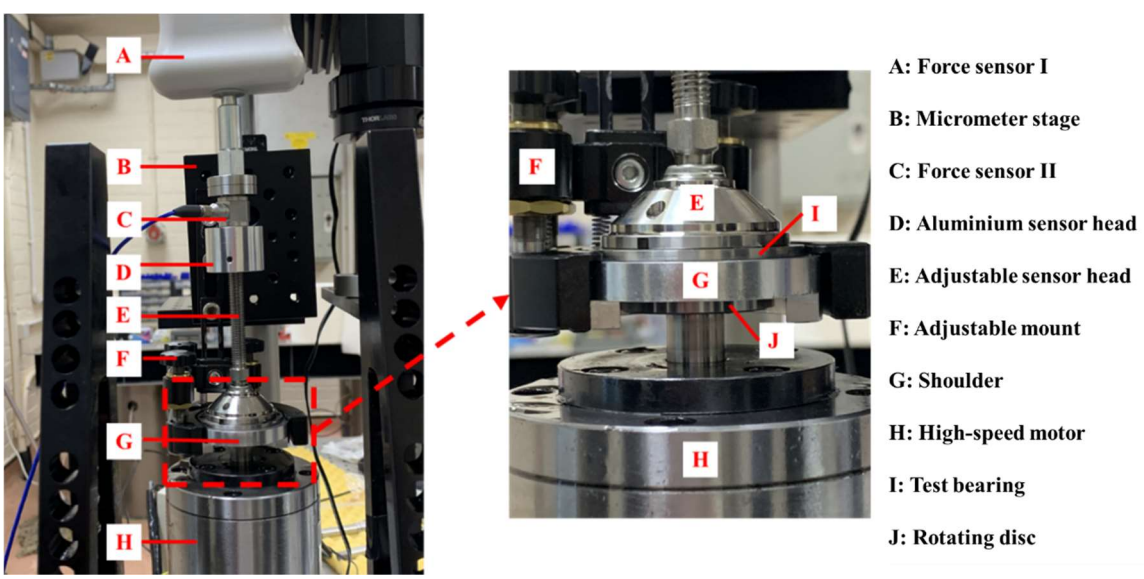


Figure 4-11: Overview of the developed test rig which can be used to measure the load capacity of grooved aerodynamic thrust bearings from 0 to 90,000 rpm.

The main part of the test rig is shown in Figure 4-12. The test bearing rests on a

shoulder with a centre-hole diameter 100 μm larger than the test bearing to provide its one-degree-of-freedom operation. The testing grooves are machined on the surface of the test bearings, while the surface of the rotating disc is kept smooth. In this way, the test bearings can be easily replaced, and thus various types of grooved aerodynamic thrust bearings can be quickly tested. During the tests, the test bearing stays stable, while the rotating disc is driven with a high-speed motor.

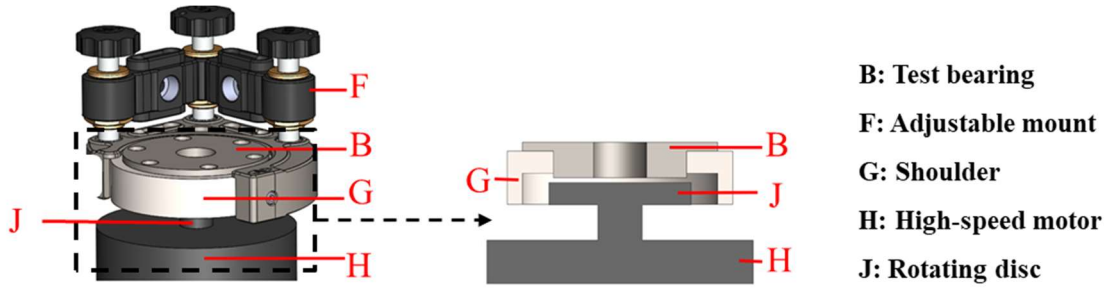


Figure 4-12: The main part of the test rig. The studied air film is formed between the rotating disc and the test bearing, while the rotating disc can rotate up to 90,000 rpm. The parallelism between the test bearing and the rotating disc is adjusted through the adjustable mount.

Table 4-2: Function description of the components of the test rig

Component	Function description
Force sensor I	It is used to measure the load capacity of the test bearing (bandwidth: 1000 Hz).
Micrometre stage	It is used to drive the test bearing close to or leave the rotating disc.
Force sensor II	It is a high-frequency dynamic force sensor used to monitor the fluctuation of the load capacity (bandwidth: 36000 Hz).
Adjustable mount	It has a tip and tilt adjustability over a range of +/- 7 degrees. It is used to adjust the parallelism between the test bearing and the rotating disc.
Shoulder	It is used to support the test bearing.
High-speed motor	It is used to drive the rotating disc to speeds up to 90,000 rpm.
Test bearing	It is the testing sample. The grooves are machined on the surface of the test bearing.
Rotating disc	It forms a thin air film with the test bearing.

The high-speed motor is lubricated by oil mist and cooled by water; thus, it is capable of performing a continuous rotation up to 90,000 rpm. The speed of the motor is controlled by an inverter. Figure 4-13 shows the arrangement of the associated lubrication, cooling and controlling systems; while Figure 4-14 shows the related instruments.

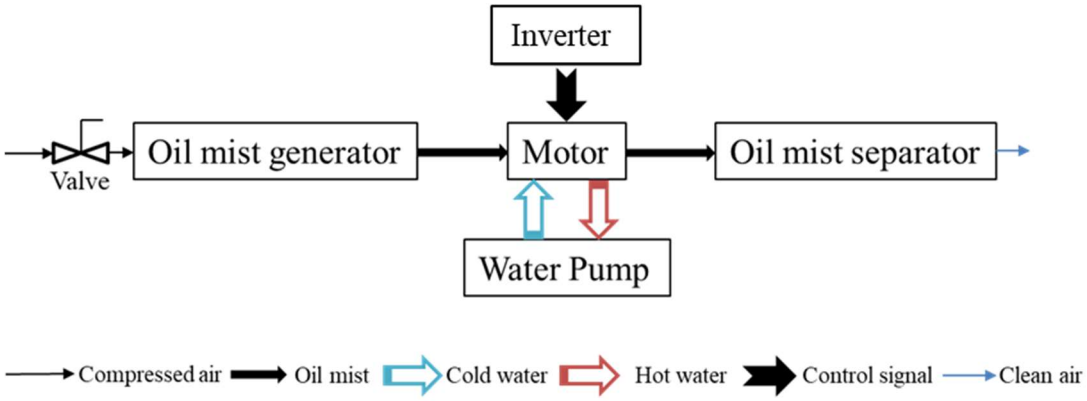


Figure 4-13: Arrangement of the associated systems for the lubricating, cooling and controlling of the motor. The motor is lubricated by oil mist and cooled by water for runs up to 90,000 rpm. The motor is controlled by an inverter. An oil mist separator is used to remove the oil from the oil mist to protect the environment.



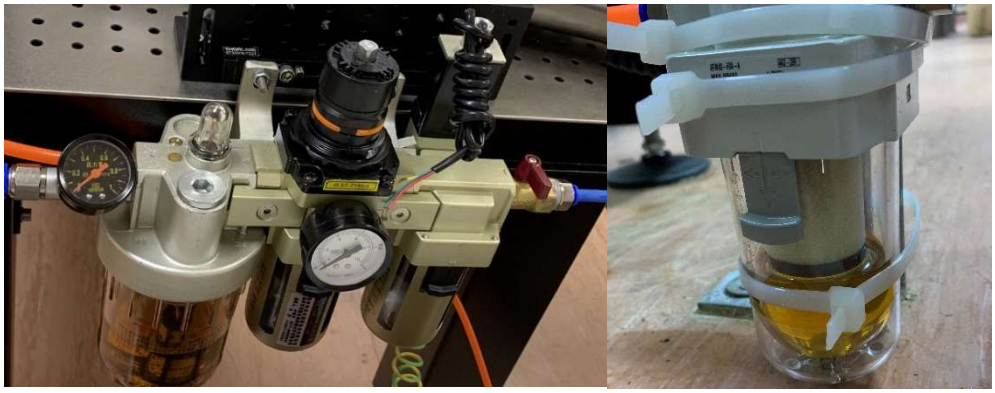
(a)



(b)



(c)



(d)

Figure 4-14: The associated system: (a) the front view (left) and side view (right) of the motor; (b) the inverter of the motor; (c) the water pump to cool the motor; (d) the oil-mist generator (left) and the oil-mist separator (right)

Before conducting tests, the parallelism between the rotating disc and the test bearing should be adjusted to an acceptable range to ensure the safety and accuracy of the experiments. The set-up to adjust the parallelism between the

test bearing and the runner is shown in Figure 4-15. The parallelism adjusting bearing is the same as the test bearing; the only difference being the parallelism adjusting bearing has a hole throughout to mount the eddy current sensor. A weight adding plate is used on the parallelism adjusting bearing for preventing tilt of the parallelism adjusting bearing caused by the sensor cables.

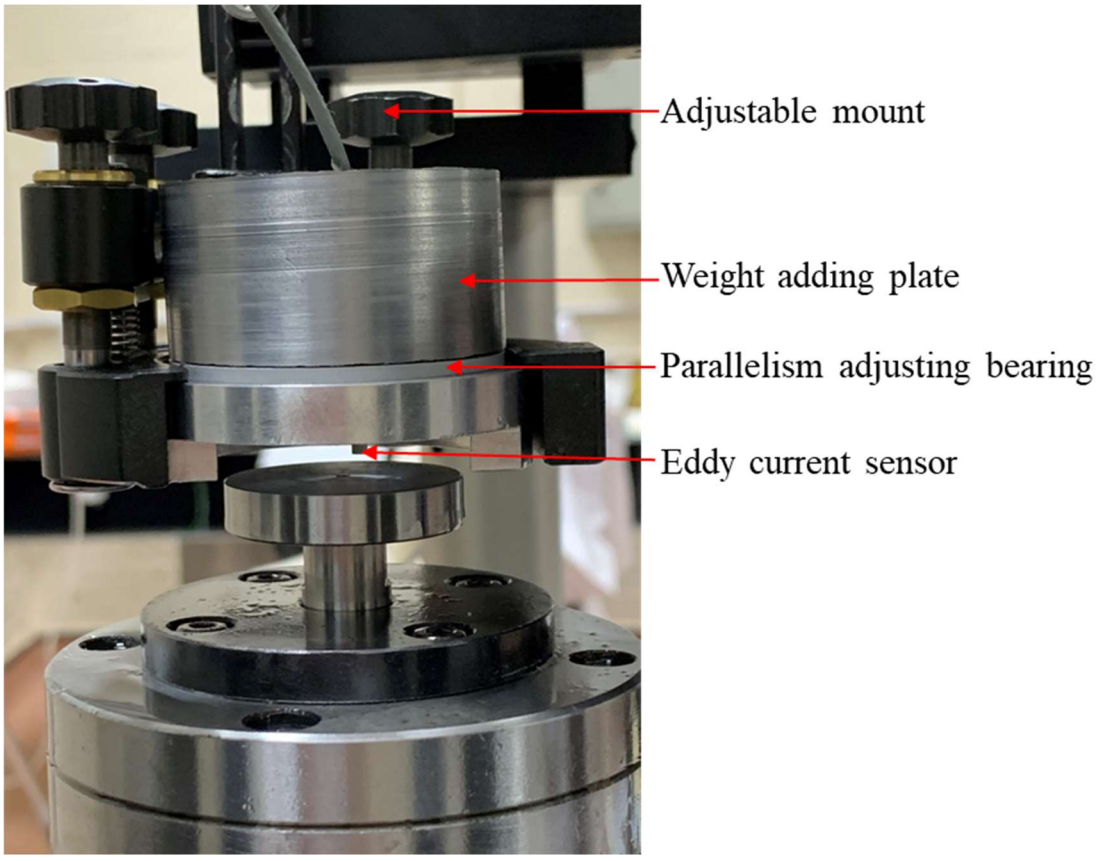


Figure 4-15: The set-up to adjust the parallelism between the two surfaces. It needs to be adjusted before each test to ensure the safety and accuracy of the tests.

Referring to Figure 4-15, the procedures to adjust the parallelism between the

test bearing and the rotating disc are introduced as follows:

i. Use the eddy current sensor (resolution: 0.025 μm) to measure the distance between the bearing surfaces at 8 points in the circumferential direction at the same intervals.

ii. If the differences of the measured air film thicknesses are within 2 μm, the two surfaces are in high parallelism; if not, tune the adjustable mount (sensitivity: 1.5 arc sec) to reduce the differences between the measured results.

iii. Repeat steps i and ii until the differences between the measured air film thicknesses are within 2 μm, which means the two surfaces are in high parallelism.

The 2 microns differences are possibly caused by the following reasons: (1) the machining error of bearing components; (2) the adjustable mount is adjusted manually. After the parallelism adjustment procedures, the parallelism adjusting bearing is replaced by the test bearing, and the designed air film thickness is achieved through adjusting the micrometre stage. The load capacity of the test bearing under various rotating speeds can be measured using the set-up in Figure 4-1. The measuring procedures are introduced as follows:

i. Move the force sensors down until the force sensor I has an initial reading, which means that the adjustable sensor head is fully in contact with the test bearing.

ii. Run the motor to the test speed and monitor the reading of the force sensor I, the increment of the reading is the measured load capacity.

The diameter of the rotating disc is 32 mm, and the maximum rotating speed of the motor is 90,000 rpm. Therefore, the test rig can be used to measure the load capacity of grooved aerodynamic thrust bearings with an outer diameter less than 32 mm at a rotating speed lower than 90,000 rpm.

4.6.2 Instrumentation

An eddy current sensor (DT3010-U05-A-C2 from MICRO-EPSILON limited) is used to measure the air film thickness between the runner and the test bearing. A static force gauge (SAUTER FK25) is used to measure the load capacity of the test bearing; while a dynamic force sensor (208C01 from PCB limited) is used to measure the fluctuation of the load capacity. All the sensors are calibrated before use. Data is acquired with a National Instruments NI BNC-2110 DAQ. The data are recorded, analysed and processed using NI signal express software on the

Windows 7 platform with an Intel® Core i5 processor. The whole data acquisition system is shown in Figure 4-16.

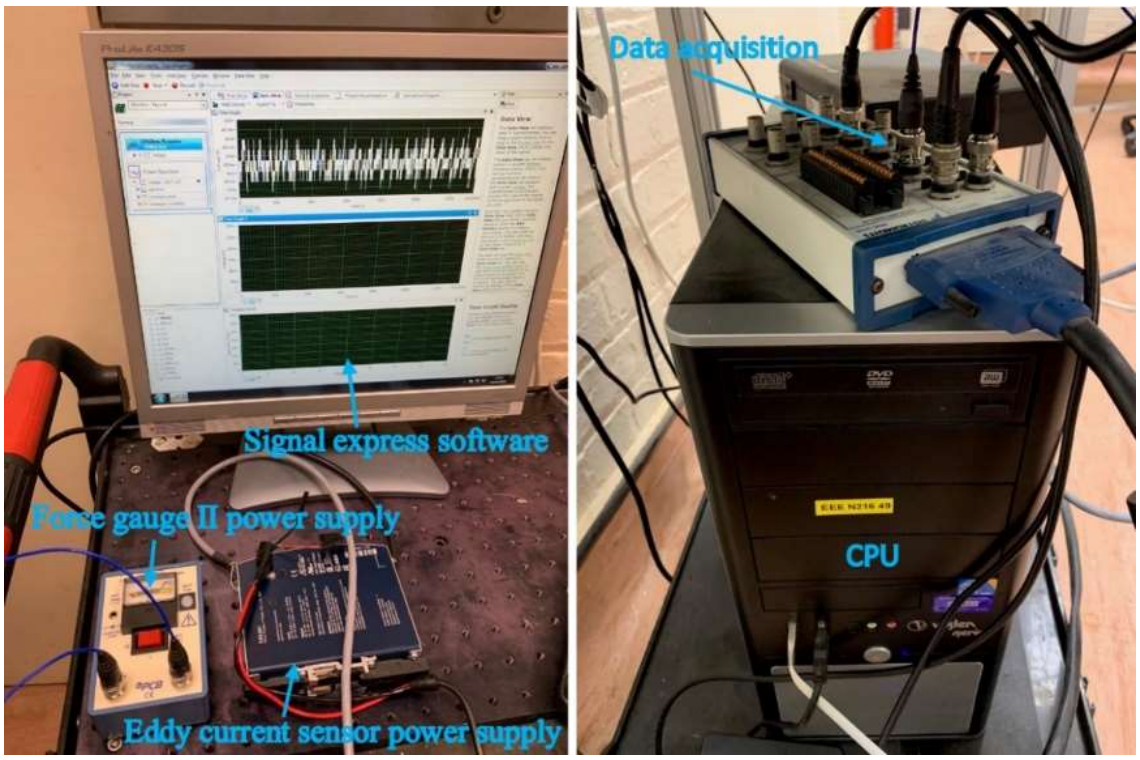


Figure 4-16: Measurement configuration

The biomimetic bearing and the optimised conventional spiral-grooved bearing are shown in Figure 4-17. The load capacity of the two bearings are measured in a range of speed up to 90,000 rpm and the air film is controlled at 10 μm. At each tested condition, the experiment is repeated three times. High reproducibility is found. The fluctuation of the load capacity is found to be within ±0.2 N during all the tests.

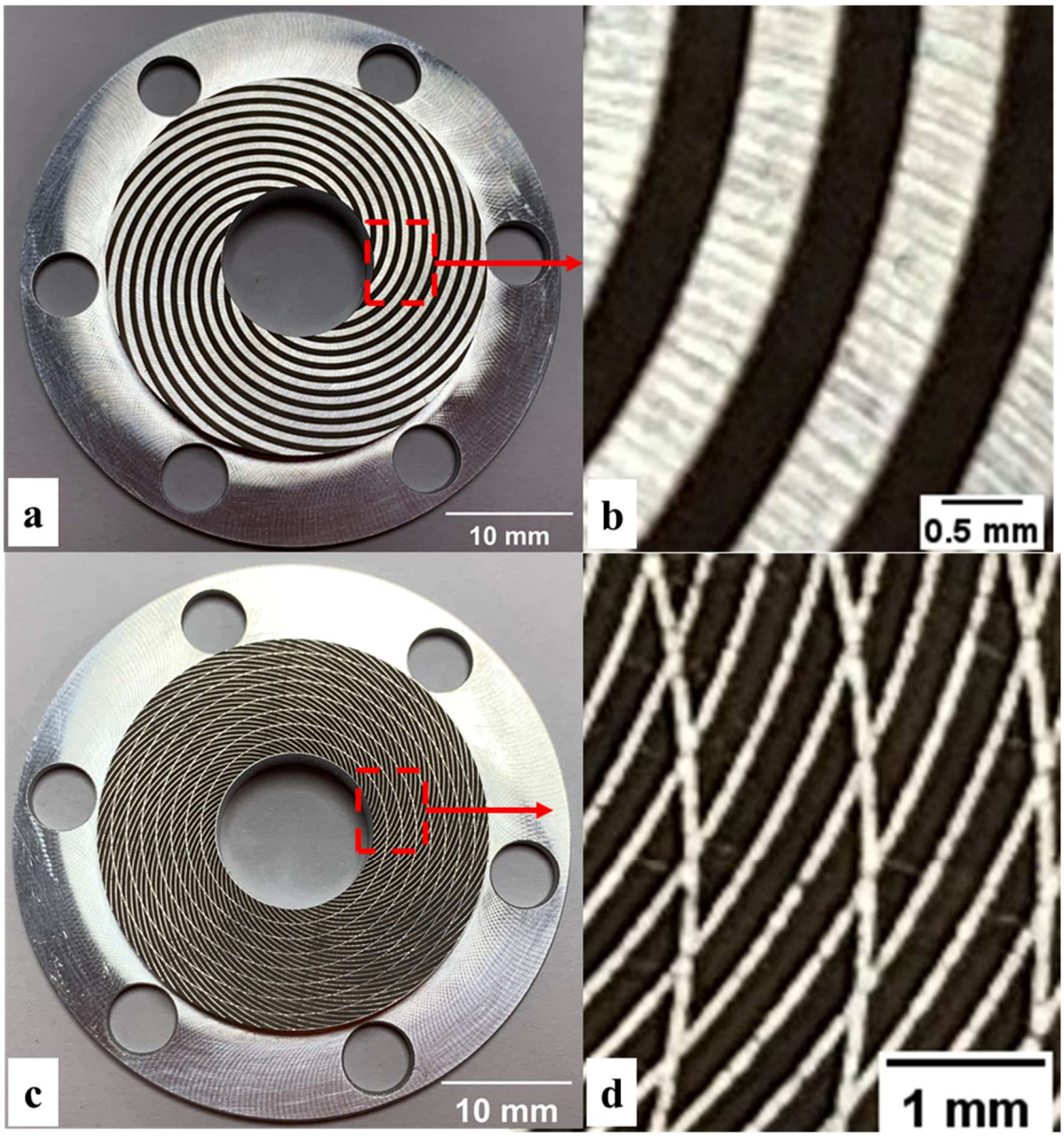


Figure 4-17: The test bearings: (a-b) the optimised spiral-grooved bearing; and (c-d) the biomimetic bearing. The surface structures of the bearings are manufactured by laser ablation (LASEA LS5-001).

4.6.3 Results and discussion

Figure 4-18 summarizes the numerical and experimental load capacity of the biomimetic bearing and the optimised spiral-grooved bearing. From the experimental results shown in Figure 4-18, it can be found that the biomimetic bearing generates a higher load capacity compared with the spiral-grooved bearing at all the measured speeds, which proves that the micro surface structures of dragonfly wings outperform the conventional grooved structures in producing the load capacity. At 90,000 rpm, the load capacity of the spiral-grooved bearing and the biomimetic bearing measured 3.21 N and 4.69 N respectively. The biomimetic bearing achieves a 46.11% higher load capacity compared to the optimised spiral-grooved bearing. Thus, it has been proved that the micro surface structures of dragonfly wings can be important biological samples to aerodynamic bearings. Moreover, a tendency can be observed that the increment percentage could be higher if the rotating speed is further increased.

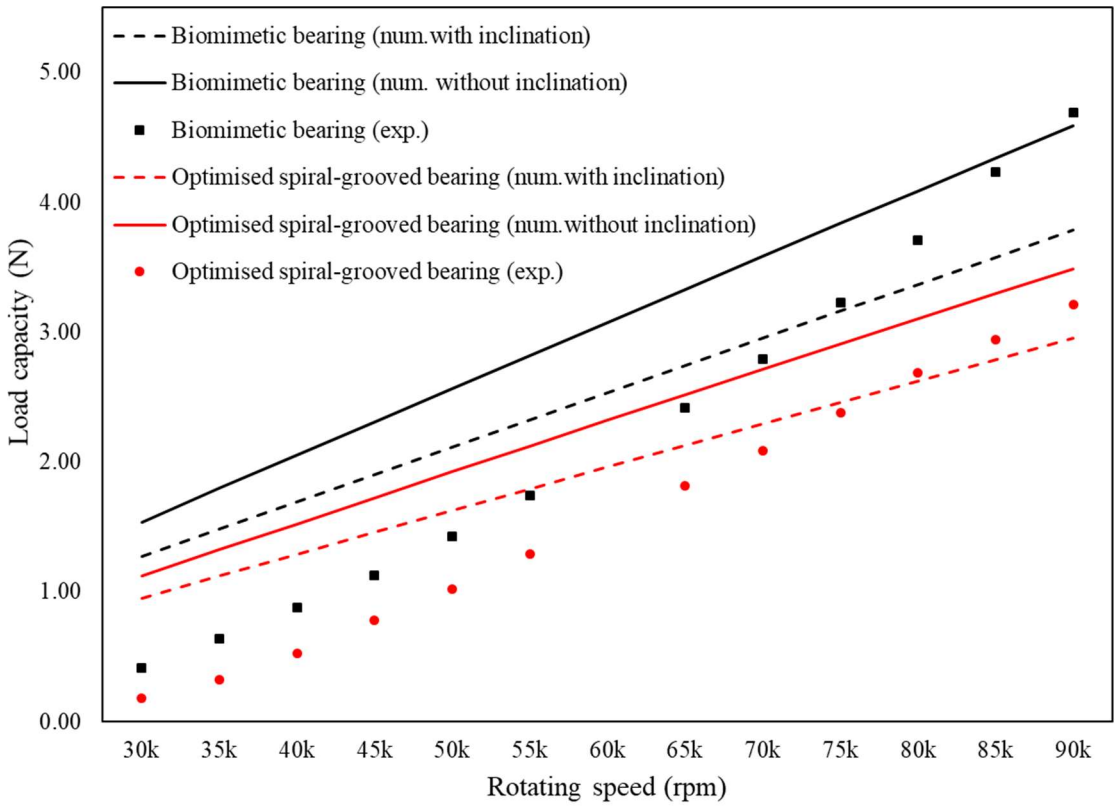


Figure 4-18: The numerical and experimental load capacity of the biomimetic bearing and the optimised spiral-grooved bearing

In simulations, air films with both perfectly parallel surfaces and a slightly inclined surface are modelled with the consideration that the parallelism of the bearing surfaces may not be perfect. The parallelism of the bearing surfaces is tuned at 8 points along the circumference with equal interval and small errors in parallelism are likely to happen. A 2 μm difference in film thickness is used to reflect the tuning limit of the bearing surfaces in the test rig. Therefore, a $\Delta h_{incline} = 2\ \mu\text{m}$ is considered when simulating an inclined air film. The results of the simulations are plotted in Figure 4-18.

In Figure 4-18, it can be found that both for perfectly parallel and inclined surfaces, the biomimetic bearing generates a higher load capacity than the optimised spiral-grooved bearing at all the simulated speeds. Besides, when a slight inclination $\Delta h_{incline} = 2\ \mu\mathrm{m}$ is considered, the results show an overall better agreement with the experimental results. The remaining discrepancies between the simulation and experiments are probably caused by the deformation of the rotating disc due to centrifugal forces [91] and the machining error of bearing components [145].

Following the above analysis, both theoretical and experimental results show that the biomimetic bearing with dragonfly wing structures indeed performs better than conventional bearings with spiral groove structures in generating the load capacity. The efficiency of the proposed biomimetic design method for aerodynamic thrust bearings has thus been proved. Consequently, the micro surface structures of dragonfly wings are proved to be important biomimetic samples for aerodynamic bearings.

4.7 Summary

The presented research in this chapter is to investigate the potential of dragonfly's wing surface structures for generating a load capacity in aerodynamic bearings.

The main contributions of the study in this chapter include: (1) the proof that the micro surface structures of dragonfly wings can generate a load capacity in fluid-film lubrications; and (2) utilized this finding in the design of the first example of the biomimetic aerodynamic bearing.

In this study, five most representative surface structures of dragonfly wings are extracted and their load capacity under the operating condition of aerodynamic thrust bearings is theoretically compared using the CFD model developed in Chapter 3. Each of the models generated an obvious load capacity. Besides, the load capacity of the models is significantly influenced by velocity directions. Based on these findings, the aligned quadrilateral micro-grids with a velocity angle of 24^0 are adopted to design the biomimetic bearing. Theoretical results show that the biomimetic bearing outperforms the optimised conventional spiral-grooved bearing in terms of load capacity and dynamic stiffness coefficient, but it sacrifices the damping coefficient.

A grooved aerodynamic thrust bearing test rig is developed to measure and compare the load capacities of the biomimetic bearing and an optimised conventional spiral-grooved bearing. The test rig is developed from scratch in this PhD project. It can measure the load capacity of grooved aerodynamic thrust bearings with an outer diameter less than 32 mm and a rotating speed less than

90,000 rpm. Experiment results show that the biomimetic bearing achieves a 46.11% higher load capacity than the conventional spiral-grooved bearing.

It has also been pointed out that the inclination of the air film surface, which exists in the experiments due to the difficulties in achieving absolute parallelism between bearing components, is found to have a substantial effect to the load capacity of tested bearings. Accordingly, a modified air film thickness is considered, and the obtained numerical results show a better agreement with the experiment results.

The finding of the study potentially opens up a wide range of applications. For example, equipped with dragonfly wing biomimetic surfaces, wind turbines could generate considerable extra power without additional costs; aeroplanes could have reduced wing sizes or even without wings; centrifugal air compressors could have reduced diameters and avoid critical stresses, and turbines and propellers could be more efficient. Also, with the example of the dragonfly wing inspired bearing, the potential of employing wings of other insects, such as bumblebee or hoverflies, as biomimetic samples for fluid-film lubrications can be explored in the future.

CHAPTER 5 GROOVE GEOMETRY OPTIMISATION FOR SPIRAL-GROOVED AERODYNAMIC THRUST BEARINGS

5.1 Introduction

This chapter introduces a novel groove geometry optimisation method for spiral-grooved aerodynamic thrust bearings (SGATBs) to improve their load capacity. The method integrates the CFD model into the CAPSO algorithm to seek the optimal groove geometry which corresponding to the maximum load capacity. Different from existing studies, which only consider continuous grooves, this method allows the possibility of finding either discontinuous or continuous grooves with completely new geometries.

The optimisation process of an initial SGATB is presented as a case study. The novel optimised grooves are shown as discontinuous grooves with a novel geometry. CFD modelling results show that the novel optimised grooves outperform the initial spiral grooves, the conventional herringbone grooves, and the conventional optimised grooves in terms of the load capacity. Experiments

are then conducted to verify the effectiveness of the proposed method.

The rest of this chapter is organized as follows: in section 5.2, the specific background and motivations of this study are introduced; in section 5.3, the spline function of grooves, the optimisation variables of the proposed method and the principles of CAPSO algorithms are introduced; in section 5.4, the optimisation process and the numerical results are demonstrated; in section 5.5, the effectiveness of the proposed method is verified experimentally; the summary is given in section 5.6. A version of this study has been accepted for publication in International Journal of Mechanical Science.

5.2 Background and motivations

Many studies have been conducted to increase the load capacity of spiral-grooved bearings [6,101,117,118,121,146]. Song et al. [117] proposed guidelines for designing spiral-grooved journal gas bearings by analysing their static and dynamic performance in various operating conditions. Satomi et al. [101] provided optimisation principles for the design of SGATBs by analysing the effects of various design parameters. Wong et al. [118] learned from macroscale gas-bearing literature and provided design charts to seek a tradeoff between the highest working speed and the load capacity of spiral-grooved gas thrust bearings.

However, limited studies have been done in finding novel groove geometries of spiral-grooved thrust bearings to increase their load capacity, except for works by Fesanghary and Khonsari [121] and Hashimoto et al. [6,97].

Fesanghary and Khonsari [121] proposed a novel groove shape to increase the load capacity of an oil-lubricated thrust bearing. Compared to conventional spiral grooves, the novel grooves could achieve a 36% higher load capacity. Similarly, Hashimoto et al. [6,97] used cubic splines to design grooves and presented novel groove geometries of spiral-grooved thrust bearings with different optimisation objectives i.e. the torque, the load capacity and the dynamic stiffness of the bearing. However, when searching for novel groove geometries, only continuous grooves are considered [6,97,121]. The potential of a higher load capacity achieved by discontinuous grooves (Figure 5-1 [147]) remains unexplored [105,106,148]. Therefore, in this study, a novel groove geometry optimisation method, which considering both discontinuous and continuous grooves, is presented to increase the load capacity of SGATBs.

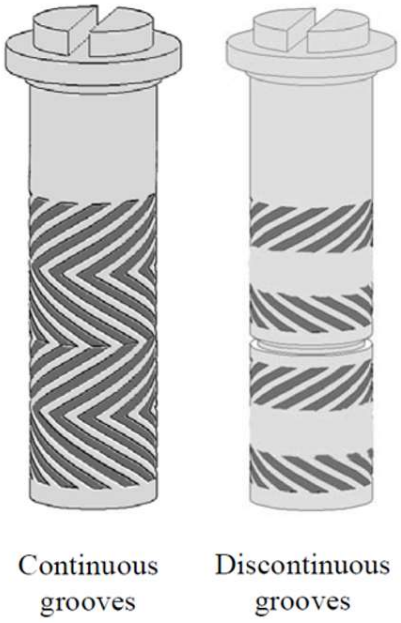


Figure 5-1: An example of continuous and discontinuous grooves [147]

5.3 Problem modelling

5.3.1 Geometrical expression of the groove

In this study, the initial spiral groove is defined by Equation (5-1):

$$\theta = \frac{1}{\tan(\alpha)} log \frac{r}{r_{\text{out}}} \tag{5-1}$$

where α the spiral angle, θ is the coordinate in the circumferential direction, r_{out} the outer radius of the bearing, and r the coordinate in the radial direction.

The initial groove is then divided into n equal sections in the radial direction. A

spline interpolation function, as listed in Equation 5-2, is used to express the general groove:

$$\theta = (\theta_i + \varphi_i)\left(\frac{r_{i+1}-r}{\Delta r}\right) + (\theta_{i+1} + \varphi_{i+1})\left(\frac{r-r_i}{\Delta r}\right) \quad (5\text{-}2)$$

where θ_i is the corresponding angle at r_i, Δr the difference between r_{i+1} and r_i, and φ_i the angle changed in the circumferential direction.

As shown in Figure 5-2, a novel groove can be obtained by adjusting the φ_i (*i*=1~n). In this study, φ_i (*i*=1~n) are retrieved using the CAPSO algorithm to seek the best groove geometry which can lead to the maximum load capacity.

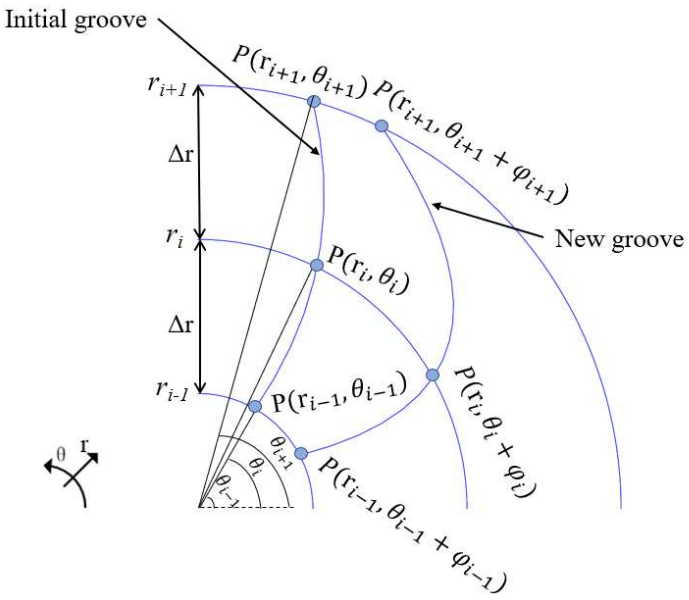


Figure 5-2: The process of finding a new groove

The depth of grooves in each section, dg_i (*i*=1~n), are also retrieved using the

CAPSO algorithm to further increase the load capacity of the bearing. When dg_i is chosen as 0, the corresponding section does not have any grooves. When dg_i is chosen as h_g, the corresponding section is covered by the grooves whose geometry is determined by φ_i. By searching for the best combination of φ_i and dg_i (i=1~n), the optimal groove geometry which can generate the maximum load capacity can be found.

5.3.2 Groove geometry optimisation

5.3.2.1 Optimisation variables and objective function

It is been illustrated in section 5.3.1 that a different combination of φ_i and dg_i (i=1~n) can lead to different continuous or discontinuous grooves. Hence, in this study, the groove geometry optimisation is formulated as seeking the optimal combination of φ_i and dg_i (i=1~n) which can lead to the maximum load capacity.

In this study, the outer radius r_2, the inner radius r_1, the air film thickness h_0, the rotating speed ω and the depth of grooves h_g of the bearing are set as the design conditions. After that, a vector of the optimisation variables X is expressed in Equation (5-3):

$$X = (\varphi_1, \varphi_2, \dots, \varphi_n, dg_1, dg_2, \dots, dg_n) \tag{5-3}$$

In this study, φ_i (*i*=1~n) is selected from $[\pm 7^0, \pm 15^0, \pm 27^0, \pm 45^0]$, while dg_i (*i*=1~n) is selected from $[0,\ h_g]$. The objective of the optimisation in this study is improving the load capacity of the bearing, thus an objective function is defined in Equation (5-4):

$$\mathrm{f(X)} = \mathrm{F} \tag{5.4}$$

where F is the load capacity of the bearing. Therefore, the groove geometry optimisation problem is formulated as:

$$max f(X) = F,\ \varphi_i = \pm 7^0\ or \pm 15^0 or \pm 27^0 or \pm 45^0,\ dg_i = 0\ or\ h_g (i = 1 \sim n) \tag{5-5}$$

5.3.2.2 Principles of CAPSO algorithms

Metaheuristic techniques are found to have good performance in seeking global optimum when dealing with optimisation problems [149]. Among various types of metaheuristic algorithms [150–153], particle swarm optimisation (PSO) algorithm has advantages that it requires less computational efforts and fewer tuning parameters [154]. Accelerated PSO (APSO) algorithm is then proposed based on the PSO algorithm for accelerating the convergence [155].

Inspired by animal swarms, the optimisation process of APSO algorithm involves three main steps: (1) with an initial position of each particle, their objective

function values are compared to find the optimal objective function value; (2) the position of particles are iterated according to a random factor, the current positions of the particles and the current best position; (3) Steps 1 and 2 are repeated until the preset convergence criteria is reached.

If the position of each particle in the iteration is $y^{(i,j)}$, where *i* is the index of iteration, *j* the index of the particle, the position of each particle in the next iteration is determined as:

$$y^{(i+1,j)} = (1-\varrho)\cdot y^{(i,j)} + \varrho \cdot g^{(i,*)} + \varsigma^{(i)} \cdot \iota^{(i,j)} \quad (5\text{-}6)$$

where $g^{(i,*)}$ the current best position in the i^{th} iteration, ϱ the attraction parameter, $\iota^{(i,j)}$ a random movement, and ς the convergence parameter which is calculated as:

$$\varsigma^{(i+1)} = \varsigma^{(i)} \cdot \gamma^{i} \quad (5\text{-}7)$$

Here, γ is the convergence factor. Many studies [154,156] suggested that $\varsigma^{(0)}$ and γ should be chosen from $[0.5,1]$. Therefore, $\varsigma^{(0)}$ is taken as 0.9 and γ is taken as 0.8 in this study.

ϱ is a constant in the standard APSO [154,156], which might force particles to jump into a local optimum. This can be solved by introducing chaotic mapping strategies into the APSO to tune the value of ϱ in each iteration [157]. With the

characteristics of stochastic, chaotic mapping strategies have shown excellent performance in increasing the chaos stability of metaheuristic algorithms [156,158,159]. Therefore, in this study, chaotic mapping strategies are adopted to tune the ϱ in each iteration considering their proved strength in dealing with various optimisation problems.

Among various chaotic mapping strategies, tent mapping strategy attracted keen interest thanks to its good performance in optimising various problems [158], thus it is adopted in this study to improve the APSO algorithm. The tent mapping strategy is formulated by Equation 5-8:

$$\varrho^{(i+1)} = \begin{cases} \frac{\varrho^{(i)}}{0.7} & \varrho^{(i)} < 0.7 \\ \frac{10}{3}(1-\varrho^{(i)}) & \varrho^{(i)} \geq 0.7 \end{cases} \quad (5\text{-}8)$$

where $\varrho^{(1)} = 0.5$ is taken in this study.

5.4 Groove geometry optimisation

5.4.1 Groove geometry optimisation process

Combining the CFD model developed in Chapter 3 with the CAPSO algorithm, this study proposes a novel groove geometry optimisation method to increase the

load capacity of SGATBs. Different from existing studies, the novel optimisation method considers both continuous and discontinuous grooves when searching for novel groove geometries. The process of the proposed method is shown in Figure 5-3. Firstly, the initial groove is divided into equal sections in the radial direction. Then, different combinations of φ_i and dg_i (i=1~n) are retrieved by the CAPSO algorithm to seek the optimal groove geometry which can lead to the highest load capacity. Before conducting the optimisation process, the working conditions of the bearing need to be confirmed. In the present study, the working conditions and design parameters of the initial SGATB are listed in Table 5-1.

Table 5-1: Working conditions and design parameters of the initial SGATB

Parameters	Values
Inner radius r_1 (mm)	6
Outer radius r_2 (mm)	15
Depth of grooves h_g (μm)	15
Air film thickness h_0 (μm)	10
The ratio of groove width to ridge width w_{gr}	1
Spiral angle α (degree)	15
Number of grooves N_g	11
Rotating speed ω (rpm)	80,000

The number of partitions of the initial groove is set as 6 in this study to ensure that even a slight change in groove geometry can be represented. The vector of the optimising variables is then defined in Equation 5-9:

$$X = (\varphi_1, \varphi_2, \dots, \varphi_6, dg_1, dg_2, \dots, dg_6) \tag{5-9}$$

Here, $\varphi_1, \varphi_2, \dots, \varphi_6$ are angular changes from the initial groove, $dg_1, dg_2, \dots, dg_6$ are the depth of grooves in each section.

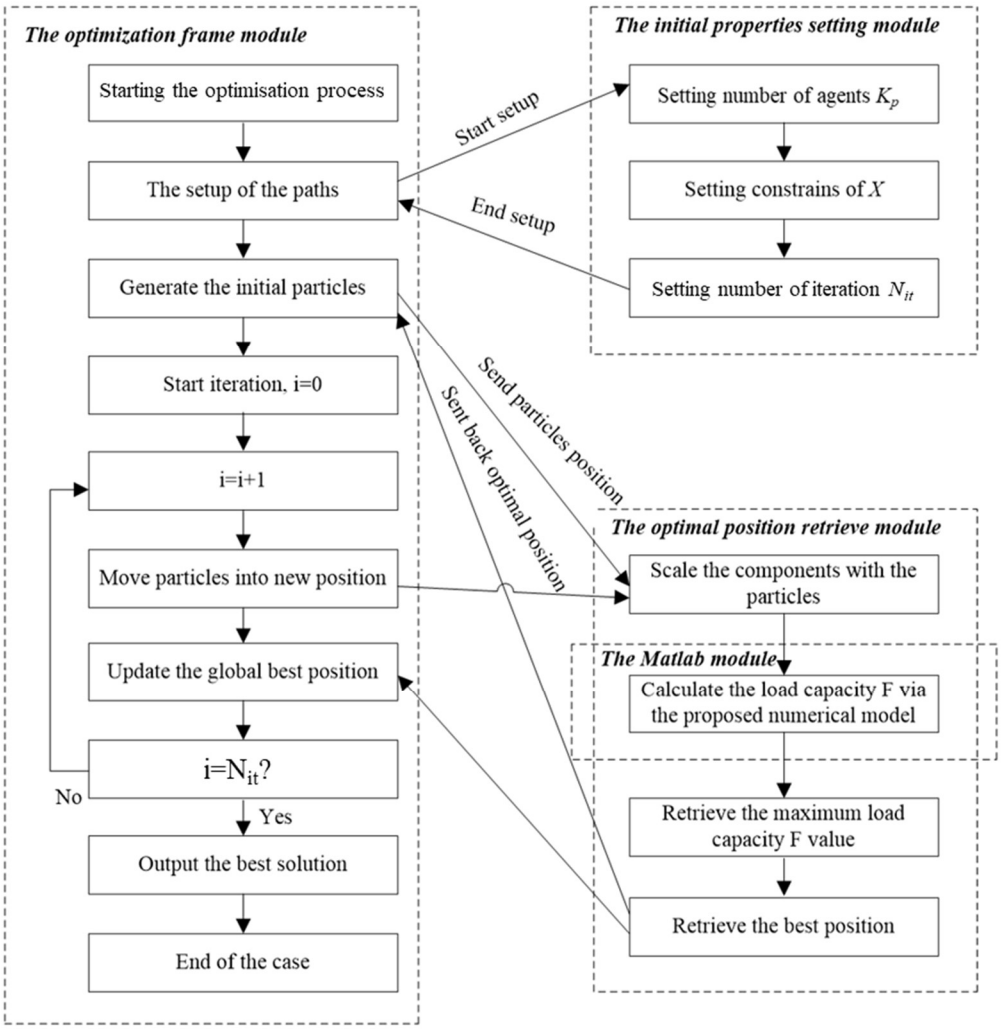


Figure 5-3: The groove geometry optimisation process

Then, the initial position of each agent (or particle) is generated randomly after the number of agents (or particles) K_p and the iteration number N_{it} are chosen. Here, the value of K_p and N_{it} should be selected reasonably to find a tradeoff between saving the computation effort and finding the global optimum.

After that, the corresponding load capacity of each agent (or particle) is calculated using the CFD model developed in Chapter 3. The position of the agent (or particle) which achieves the highest load capacity is set to be the current best position. Based on the current best position, a random factor, and the current actual position of each agent (or particle), the new position of each agent (or particle) is found. The result at the N_{it} iteration is the final optimisation result.

5.4.2 Optimisation results

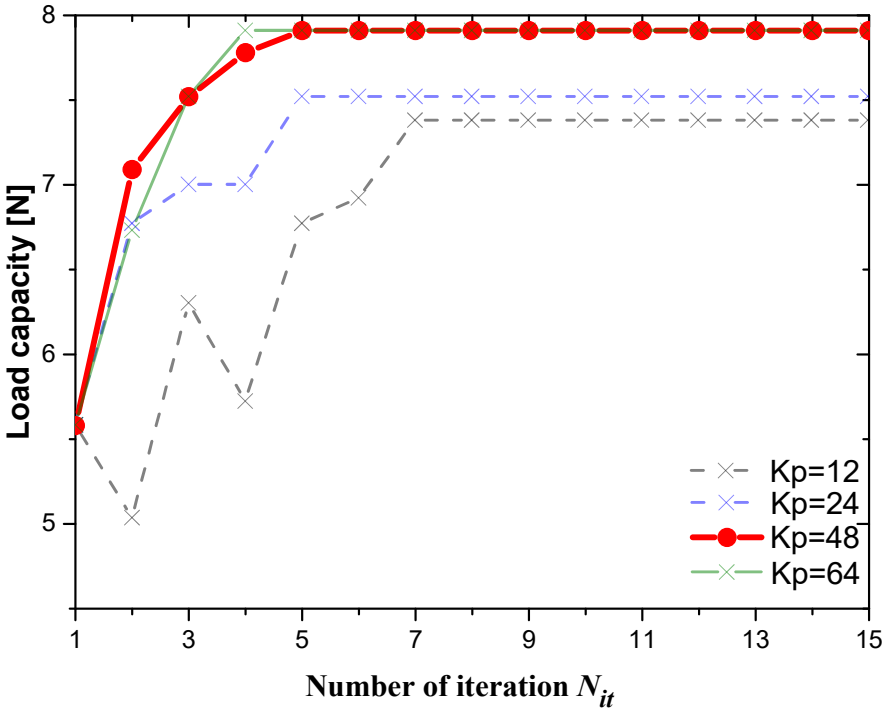
The optimisation progress of the proposed method with a various number of agents (or particles) K_p is shown in Figure 5-4. For comparison, the progress of a conventional optimisation method, which considers continuous grooves only, is also presented in Figure 5-4. The only difference between the two optimisation methods is in their optimisation variables, as listed in Table 5-2. For the conventional optimisation method, the optimisation variables only include the angles changed in the circumferential direction, which are the same with the

optimisation variables in Ref. [97]. For the proposed method, the optimisation variables include the angular changes in the circumferential direction and the depth of grooves in each section. In this way, both continuous and discontinuous grooves are considered.

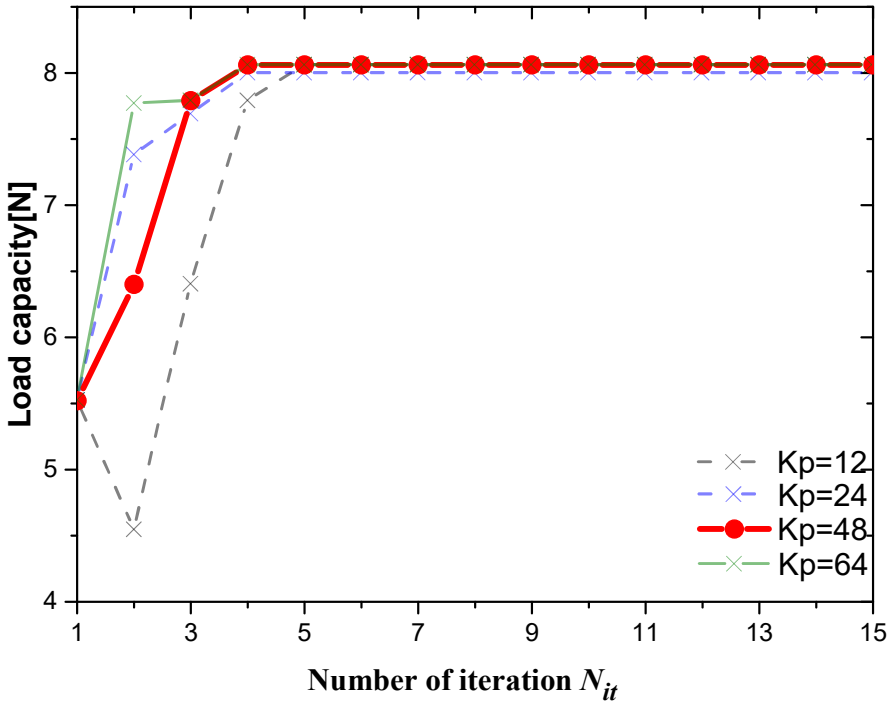
Table 5-2: The vector of optimisation variables of the proposed method and the conventional method

Vector of optimisation variables	Conventional method	Proposed method
X	$\varphi_1, \varphi_2, \dots, \varphi_6$	$\varphi_1, \varphi_2, \dots, \varphi_6, dg_1, dg_2, \dots, dg_6$

From Figure 5-4, it could be found that for both of the methods, a satisfying convergence is achieved within 15 iterations. For the conventional method, the optimal results are local optimum when K_p is taken as 12 or 24. When K_p is taken as 48 or 64, a higher load capacity can be found. Therefore, to find a tradeoff between finding the global optimum and saving the computational effort, in this case, the K_p is taken as 48 and the N_{it} is taken as 15.



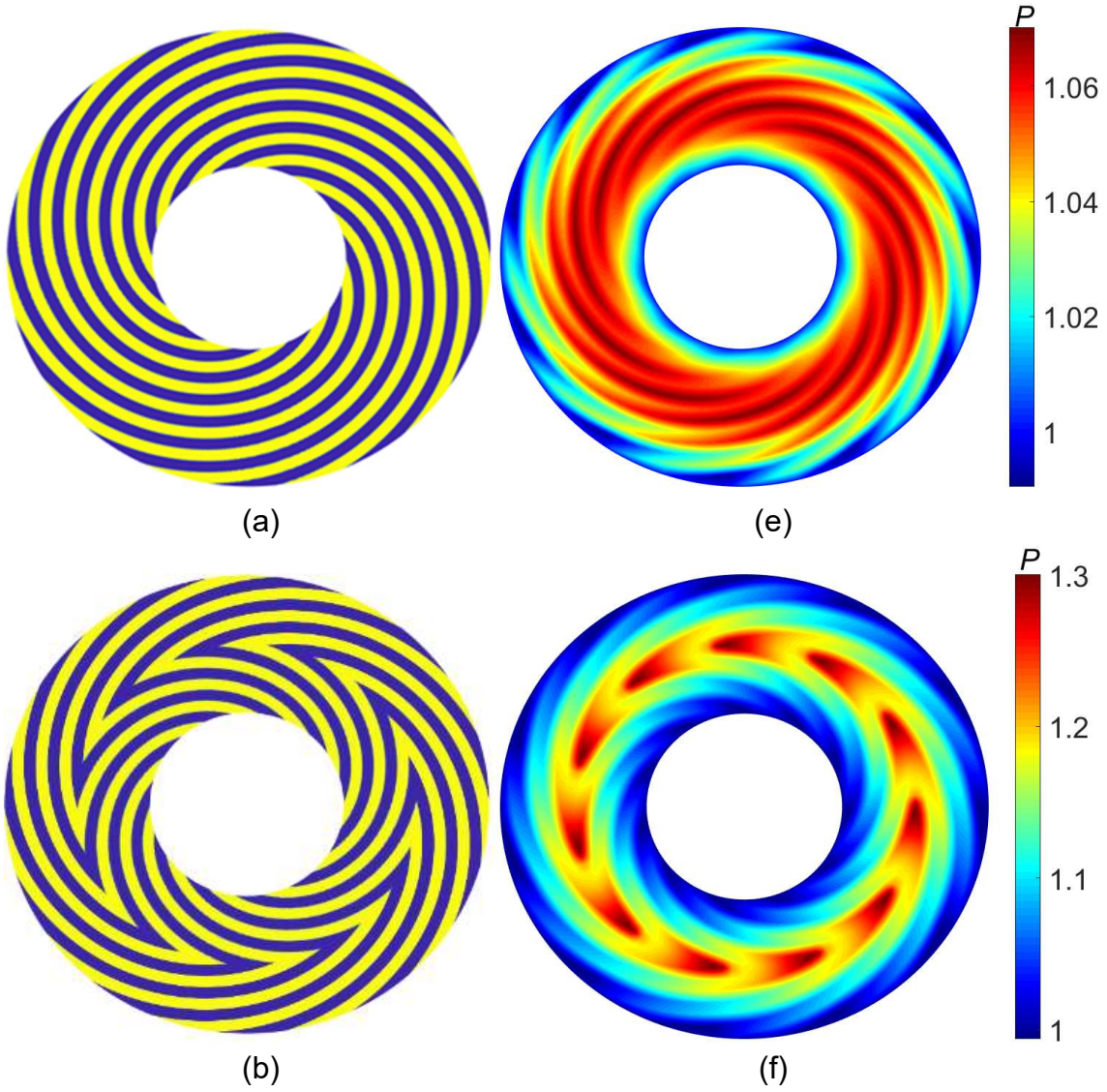
(a)



(b)

Figure 5-4: The optimisation process of: (a) the conventional optimisation method; and (b) the proposed optimisation method

It can also be seen from Figure 5-4 that the proposed optimisation method can achieve a higher load capacity compared to the conventional optimisation method. The geometries and dimensionless pressure distributions of the initial spiral grooves, conventional optimised grooves and novel optimised grooves are shown in Figure 5-5. As a comparison, the geometry and dimensionless pressure distribution of the conventional herringbone grooves are also presented in Figure 5-5.



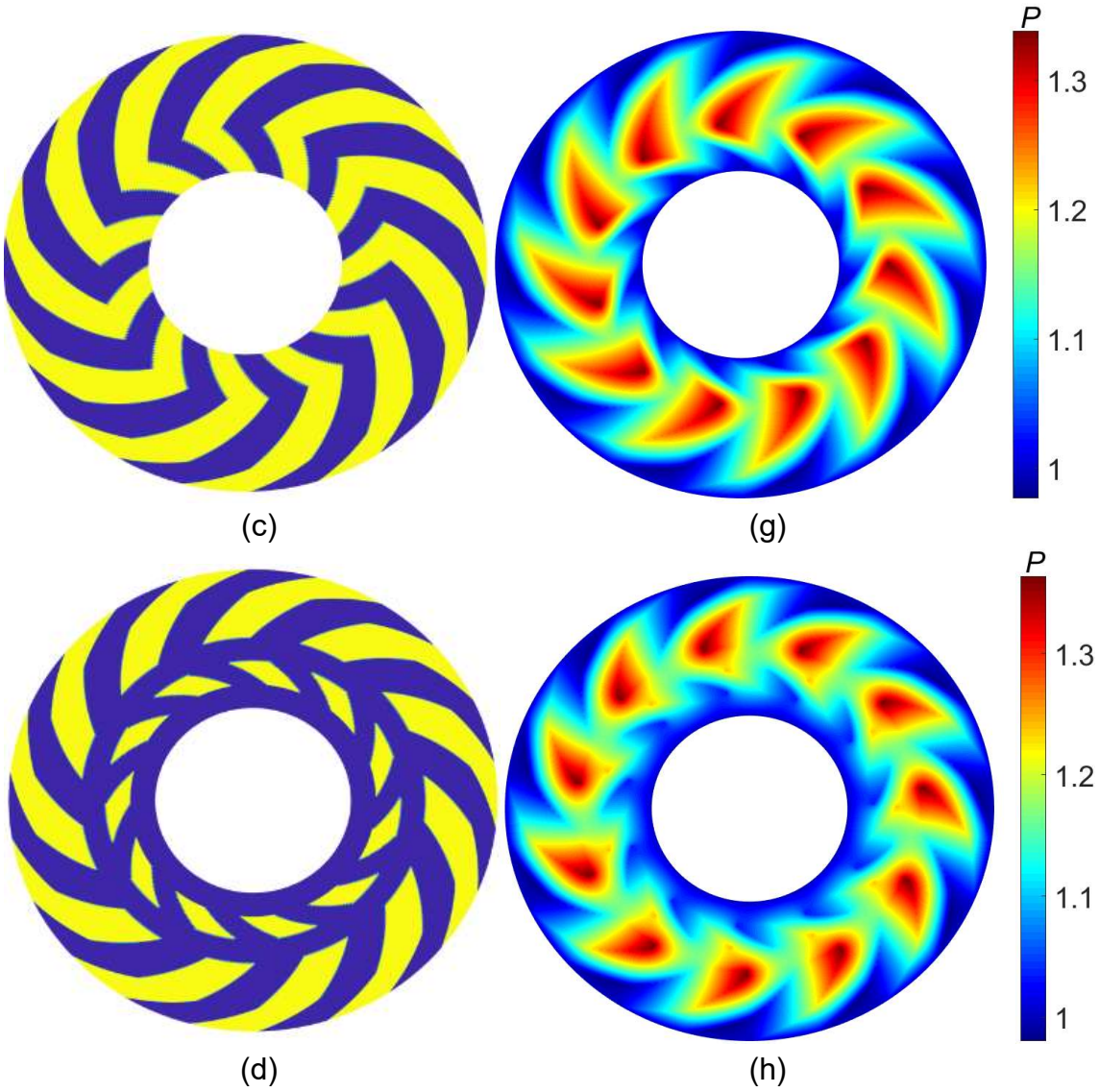


Figure 5-5: The geometries of: (a) the initial spiral grooves; (b) the conventional herringbone grooves; (c) the conventional optimised grooves; (d) the novel optimised grooves, and the dimensionless pressure distribution of: (e) the initial spiral grooves; (f) the conventional herringbone grooves; (g) the conventional optimised grooves; (h) the novel optimised grooves. Here, the grooves are represented by yellow areas, while the ridges are represented by the blue.

As shown in Figures 5-5, both the conventional optimised groove and the

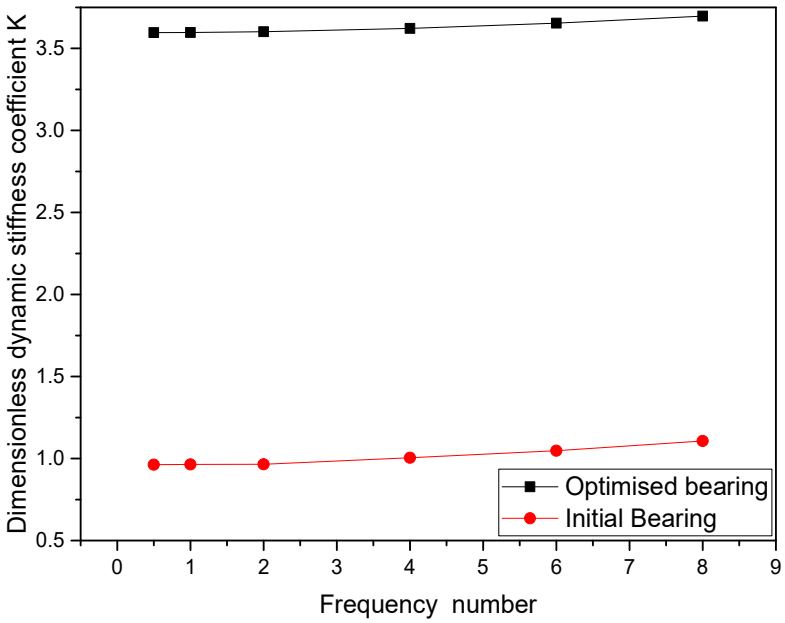
conventional herringbone groove have a sharp bend in the midway of the groove. However, different from the conventional herringbone groove, the conventional optimised groove shows a sharper bend in the region near the outer boundary. The novel optimised groove shows a similar geometry with the conventional optimised groove in the region between the middle of the bearing and the outer boundary. However, the novel optimised groove has two unique features: (1) its inner circular region does not have any groove, and (2) its middle circular region is smooth without any groove.

Table 5-3 lists the load capacity of the studied grooves obtained by the CFD model developed in Chapter 3. It can be concluded from Table 5-3 that all of the conventional herringbone grooves, the conventional optimised grooves and the novel optimised grooves achieve a higher load capacity compared with the initial spiral grooves. In particular, the load capacity obtained by the novel optimised grooves is the highest among all the grooves, followed by the conventional optimised grooves and the conventional herringbone grooves.

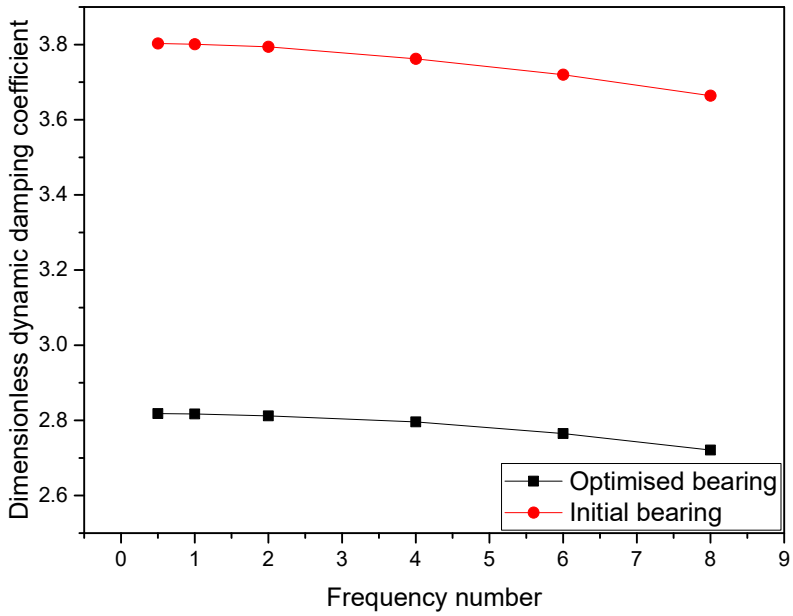
Table 5-3: The load capacity of all the studied grooves

	Initial spiral grooves	Conventional herringbone grooves	Conventional optimised grooves	Novel optimised grooves
Load capacity (N)	2.23	7.01	7.82	8.06
Increment percentage	-	214.35%	250.67%	261.43%

The dynamic stiffness and damping coefficients of the novel optimised and initial spiral grooves under various frequency number are also compared in Figure 5-6. It can be concluded that the novel optimised bearing can always achieve a higher dynamic stiffness coefficient than the initial SGATB, but it sacrifices the dynamic damping coefficient. This is acceptable since the objective of the proposed optimisation method is determined to improve the load capacity. For applications which seeking high damping coefficient, the problem can be solved either by introducing external damping through flexible support or changing the optimisation objective to improve the damping coefficients.



(a)

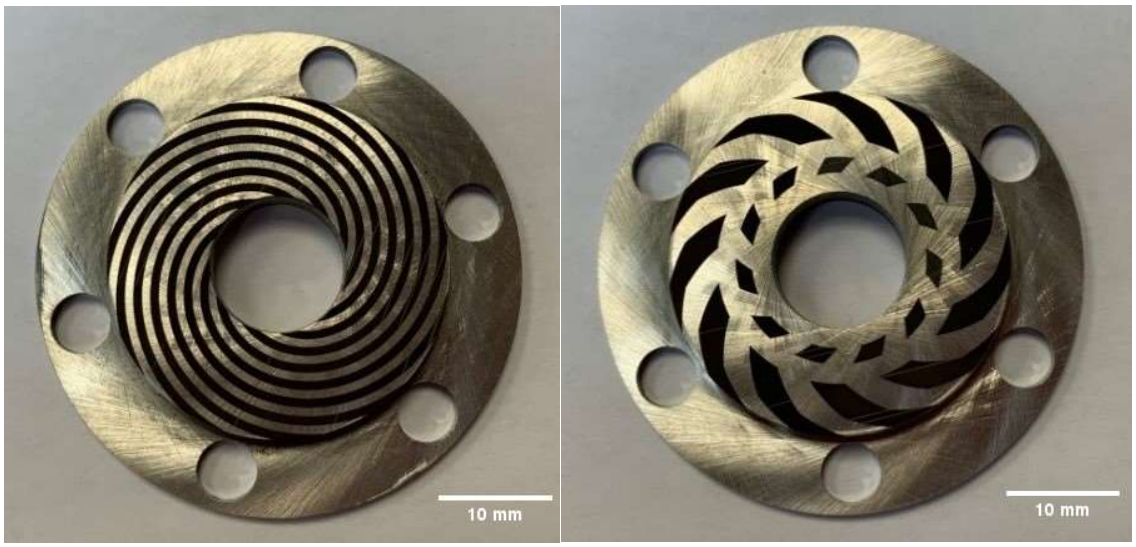


(b)

Figure 5-6: The dynamic performance of the optimised and initial bearing: (a) the dimensionless dynamic stiffness coefficients and (b) the dimensionless dynamic damping coefficients against the frequency number at 80,000 rpm

5.5 Experiment results and discussion

The proposed optimisation method is examined experimentally by comparing the load capacities of the initial spiral grooves and the novel optimised grooves. The test bearings with the initial spiral grooves and the novel optimised grooves are presented in Figure 5-7. The test rig for measuring the load capacity has been introduced in chapter 4. At each testing condition, the load capacity of the test bearing is measured three times. High repeatability is found. The mean values of measurements are taken as the experiment results of the load capacity. During all the tests, the fluctuation of the load capacity is all within ±0.4 N.



(a) (b)

Figure 5-7: The test bearings: (a) the initial SGATB; and (b) the novel optimised bearing. The grooves are manufactured by laser ablation (LASEA LS5-001).

The simulation and experiment results of the load capacity of the tested bearing are compared in Figure 5-8. At all the tested conditions, the measured load capacity of the novel optimised bearing is obviously higher than the load capacity of the initial SGATB, indicating a strong effect of the optimisation. At 80,000 rpm, the load capacity of the novel optimised bearing measured 7.12 N, while the load capacity of the initial SGATB measured 2.65 N. An increase of 168.68% in load capacity is achieved after optimisation. It also needs to be pointed out that this increment percentage might be even higher if the rotating speed is higher, as shown in Figure 5-8.

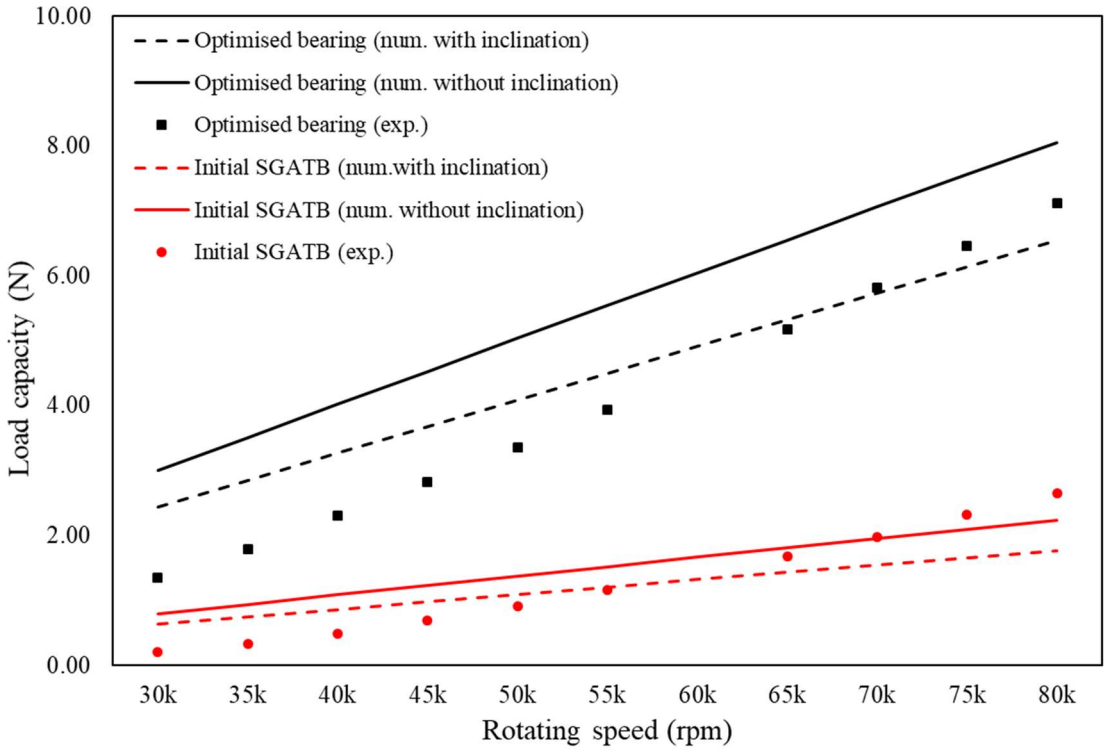


Figure 5-8: The theoretical and experimental load capacity of the initial SGATB and the novel optimised bearing.

In simulations, air films with both perfectly parallel surfaces and a slightly inclined surface with $\Delta h_{incline} = 2\ \mu\mathrm{m}$ are modelled. The results of the simulations are plotted in Figure 5-8. It can be found that both for perfectly parallel and inclined surfaces, the novel optimised bearing achieves a higher load capacity than the initial SGATB at all speeds. Besides, when a slight inclination $\Delta h_{incline} = 2\ \mu\mathrm{m}$ is considered, the simulation results show better agreement with the experimental results. The remaining discrepancies between the simulation and experiments are probably caused by the deformation of the rotating disc due to centrifugal forces [91] and the machining error of bearing components [145].

Following the above analysis, both theoretical and experimental results show that the novel optimised bearing with discontinuous grooves indeed performs better than the initial SGATB in generating a load capacity, the efficiency of the proposed groove geometry optimisation method has thus been proved. Simulation results also show that the novel optimised bearing has a higher load capacity than the bearings with conventional herringbone grooves and optimised continuous grooves, which further proves the superiority of the proposed method.

The reasons for the increased load capacity can be given below. For the initial spiral grooves, airflow is pumped into the middle part of the bearing only from the outer bearing boundary to produce positive pressure. Differently, the air is

pumped from both the inner and outer bearing boundaries for conventional herringbone grooves and conventional optimised grooves. In this way, higher positive pressure is produced, which can lead to a higher load capacity. Compared to the conventional herringbone grooves, the sharp bend near the outer boundary of the conventional optimised grooves helps to pump more air, while the less sharp bend near the middle part of the bearing helps hold more air by forming a wider airflow passage. Consequently, higher positive pressure is generated, thus a higher load capacity is achieved. The novel optimised grooves do not have any grooves in the middle and inner parts compared with conventional optimised grooves. When it works, the air is scooped from both the inner and outer boundaries, while the ridge areas in the bearing help damp air leakage and maintain the pressure. In this way, a higher load capacity is obtained.

5.6 Summary

In this chapter, a novel groove geometry optimisation method for SGATBs is proposed to improve their load capacity. In the proposed optimisation method, firstly, the initial groove is divided into equal sections in the radial direction. Next, the key parameters of the groove and the depth of the grooves in each section are retrieved by the CAPSO algorithm to find the optimal groove geometry which

can lead to the highest load capacity.

A case study of the optimisation of an initial SGATB is presented. The novel optimised grooves are discontinuous grooves with completely new geometry. Theoretical results show that the novel optimised grooves have a higher load capacity than the initial spiral grooves, the conventional herringbone grooves and the conventional optimised grooves. Besides, at all of the simulated conditions, the novel optimised bearing has higher dynamic stiffness coefficients than the initial SGATB, but it sacrifices the dynamic damping coefficients.

The static load capacities of the novel optimised and initial bearings are measured experimentally using the test rig introduced in Chapter 4. Similarly, when the inclination of the air film which existing in the experiments is considered, the obtained numerical results show a better agreement with the experiment results. At all the tested conditions, the novel optimised bearing achieves a higher load capacity comparing to the initial SGATB. In particular, at 80,000 rpm, the load capacity of the novel optimised bearing is measured as 7.12 N, while the load capacity of the initial SGATB is measured as measured 2.65 N. The load capacity has been improved by 168.68% after the optimisation. The effectiveness of the proposed optimisation method has thus been verified.

The main contributions of the study in this chapter are: (1) the design and

verification of a novel groove geometry optimisation method, which integrate the CFD model into the CAPSO algorithm to increase the load capacity of spiral-grooved aerodynamic thrust bearings, and (2) the proof that a higher load capacity can be achieved by considering both discontinuous and continuous grooves in the optimisation process. The proposed optimisation method can also be modified to optimise other bearing performance i.e. torque, stiffness, damping, or any combination of them. Moreover, other designing parameters of SGATBs i.e. the ratio of groove width to ridge width and the number of grooves can also be selected as optimisation variables to explore the potential of a higher load capacity in the future, but that will cost much longer computational time.

CHAPTER 6 GROOVE CONFIGURATION OPTIMISATION OF HERRINGBONE-GROOVED AERODYNAMIC THRUST BEARINGS

6.1 Introduction

In this chapter, a novel optimisation method is proposed for improving the load capacity of herringbone-grooved aerodynamic thrust bearings by seeking the optimal groove parameters in each section of the bearing independently. An example of an optimised HGATB is presented. The resultant herringbone grooves are found to have different parameters in the inner and outer sections, which is uncommon in existing grooves. Numerical results show that the novel HGATB has a higher load capacity than a non-optimised HGATB and a conventionally optimised HGATB. Experiment results verified that the new design can increase load capacity by 30.77%.

The rest of this chapter is constructed as follows: section 6.2 gives the specific background and motivations of this study; section 6.3 formulates the groove configuration optimisation as searching for the optimal combination of key groove

parameters in different sections of herringbone grooves; section 6.4 illustrates the optimisation process and the numerical results; section 6.5 introduces the experiment verification processes; section 6.6 states the conclusions. A version of this study has been submitted for publication.

6.2 Background and motivations

Many studies have focused on finding the optimal parameters of the herringbone grooves for improved performance [86,94,160]. Hirayama et al. [160] optimised groove width ratio, groove angle and dimensionless depth of grooves in herringbone-grooved journal bearings to improve the repeatable runout characteristics. Hashimoto et al. [94] optimised the depth of grooves, the ratio of groove width to ridge width, the groove angle, the number of grooves of an HGATB to improve the friction and stability characteristics. Zhang et al. [86] investigated the effects of depth of grooves, air film thickness, groove angle, number of grooves on the load capacity of an HGATB to find the optimum parameters. However, the abovementioned studies did not design grooves in sections differently.

Different from the abovementioned studies, Chen et al. [161,162] analysed the

optimum parameters of herringbone-grooved journal bearings under small radius for increased load capacity. In particular, they optimised the groove angles in different sections of the journal bearing independently. Similarly, Yen et al. [163] optimised the elliptical axis ratios of six regions of elliptical grooved bearings and achieved a higher load capacity than conventional herringbone-grooved cylindrical journal bearings.

However, the optimisation processes in references [161–163] are all focused on journal bearings which have the same linear velocity at any position of the bearing. Since thrust bearings have different linear velocities along the radial direction, it is reasonable to assume that having different grooves in different radial sections could lead to higher load capacity. The author has not found reports of an optimal design method using different groove parameters in different radial sections in HGATBs. In this study, a novel groove configuration optimisation method is proposed to improve the load capacity of HGATBs by searching for the optimal groove parameters in two radial sections independently.

6.3 Search area and the objective function

An example of herringbone grooves is shown in Figure 6-1, where r_1 is the inner radius, r_2 the outer radius, r_m the average radius which equals the mean value of

r_1 and r_2, r_{s1} the inner sealing radius where the groove in the inner section finishes, r_{s2} the outer sealing radius where the groove in outer section starts, b_1 is the groove width, b_2 the ridge width, α the groove angle. The ratio of groove width to ridge width $w_{gr} = \frac{b_1}{b_2}$, and the sealing ratio $\sigma_{sealing} = \frac{r_2 - r_{s2}}{r_2 - r_m} (= \frac{r_{s1} - r_1}{r_m - r_1})$.

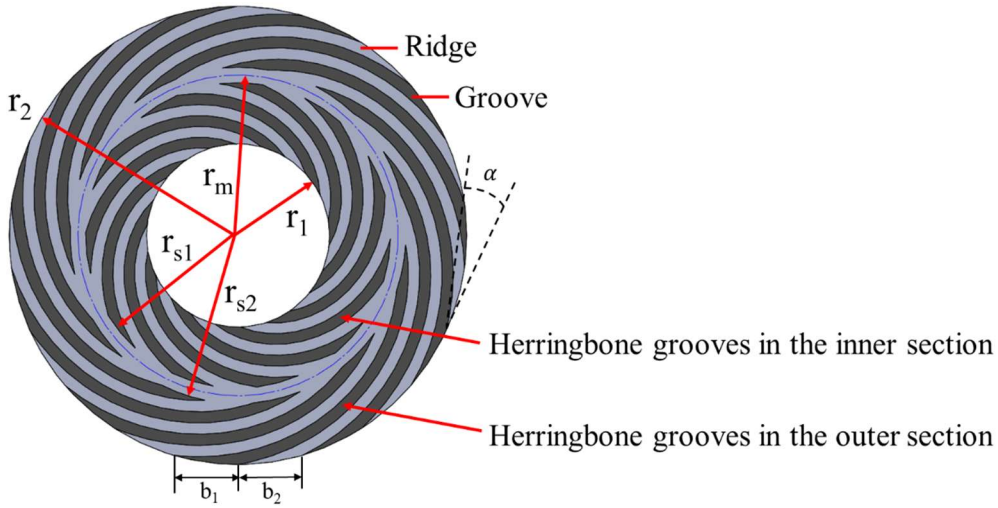


Figure 6-1: Variables of herringbone grooves

Any groove parameters, bearing dimension parameters and bearing working conditions can be taken as design variables. For limiting the simulation time to a manageable level, in this study, the ratio of groove width to ridge width, the groove angle, the sealing ratio and the number of grooves in the inner and outer sections of herringbone grooves are taken as the design variables to increase the load capacity, while other bearing parameters are set as constants. However, this decision does not imply that other parameters are less important. The optimisation process is formulated as finding the best combination of the ratio of

groove width to ridge width ($w_{gr\text{-}inner}$ and $w_{gr\text{-}outer}$), groove angles (α_{inner} and α_{outer}), sealing ratio ($\sigma_{sealing}$) and the number of grooves (n_{inner} and n_{outer}) in different sections of herringbone grooves for achieving the highest load capacity. In formulating the groove configuration optimisation problem, the inner radius r_1, the outer radius r_2, the air film thickness h_0, the rotating speed ω and the depth of grooves h_g are set at the beginning as the designing conditions. Then, a vector of design variables X can be defined as the equation (6-1):

$$X = (w_{gr-inner}, w_{gr-outer}, \alpha_{inner}, \alpha_{outer}, n_{inner}, n_{outer}, \sigma_{sealing}) \quad (6\text{-}1)$$

6.4 Groove configuration optimisation

6.4.1 Groove configuration optimisation Process

The permissible values of each groove parameter are listed in Table 6-1. The operating conditions and other design parameters of a conventional herringbone-grooved aerodynamic thrust bearing (non-optimised HGATB) are listed in Table 6-2. Before the optimisation, the effect of the permissible values of the groove parameters on the load capacity of the non-optimised bearing is checked, as shown in Figure 6-2. It can be found that the ranges of the search values cover the maximum load capacity. Thus, the set of permissible values is reasonable

and can be used for the following optimisation.

Table 6-1: Groove design variables and their permissible values in the optimisation process

Variable	Value
$w_{gr-inner}, w_{gr-outer}$	0.11, 0.25, 0.43, 0.67, 1, 1.5, 2.3, 4, 9
$\alpha_{inner}, \alpha_{outer}$	$\pm 7^0, \pm 15^0, \pm 27^0, \pm 45^0$
n_{inner}, n_{outer}	4,8,11,22,44,55
$\sigma_{sealing}$	$\frac{1}{2}, \frac{1}{4}, \frac{1}{6}, \frac{1}{8}, \frac{1}{10}, \frac{1}{15}, \frac{1}{20}$,0

Table 6-2: Design variables and operating conditions of the non-optimised HGATB

Parameters	Values
Inner radius r_1 (mm)	6
Outer radius r_2 (mm)	15
Depth of grooves h_g (μm)	15
Air film thickness h_0 (μm)	10
The ratio of groove width to ridge width w_{gr}	1
Spiral angle α (degree)	15
Number of grooves N	11
Rotating speed ω (rpm)	70,000

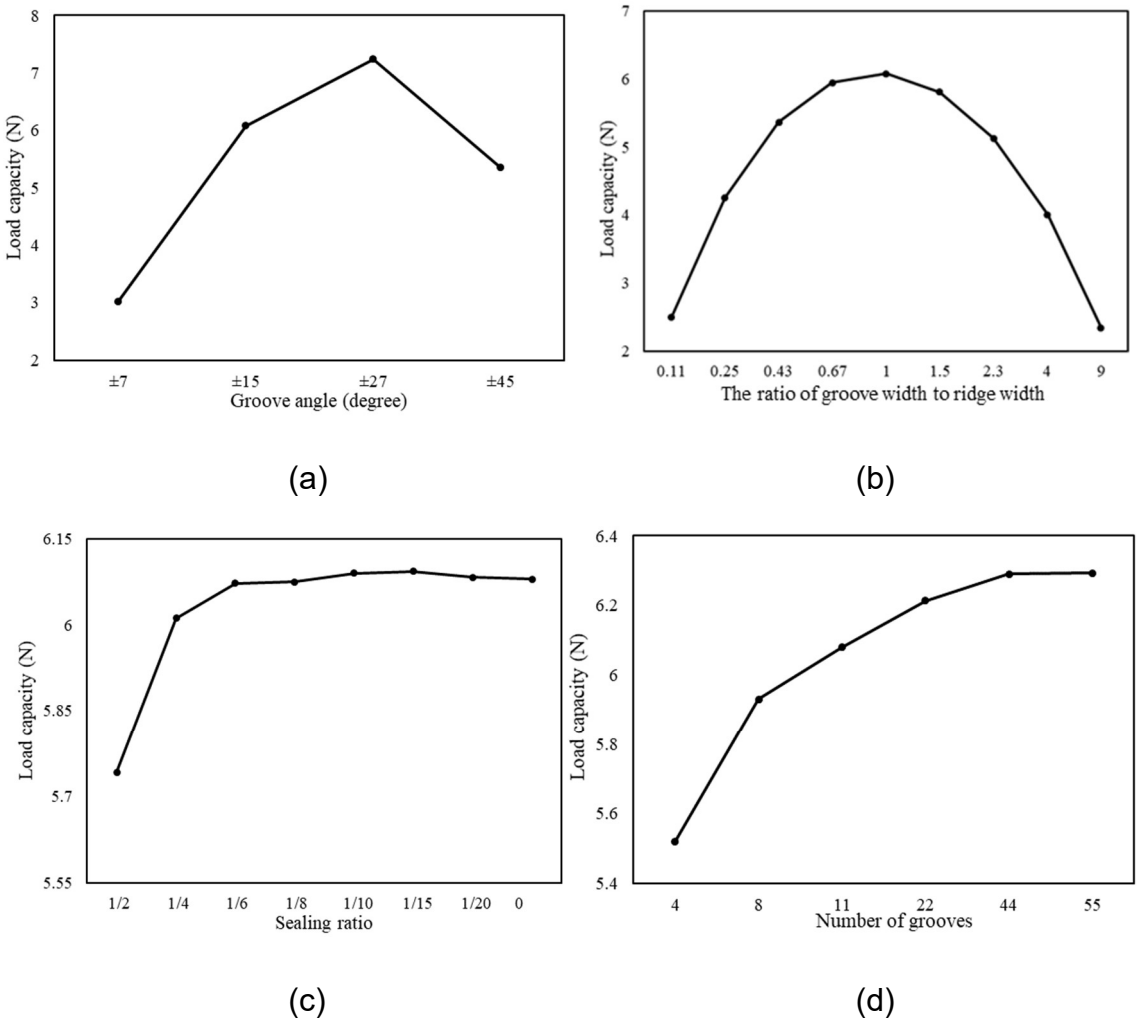


Figure 6-2: The effect of the permissible values of the groove parameters on the non-optimised HGATB

The optimisation process is shown in Figure 6-3. With vector $X = (w_{gr-inner}, w_{gr-outer}, \alpha_{inner}, \alpha_{outer}, n_{inner}, n_{outer}, \sigma_{sealing})$, the pre-decided number of iterations N_{it} and number of particles K_p, the initial position of each particle is obtained, and the load capacity of each particle is calculated using the CFD model build in Chapter 3. The best X of the initial particles is found for achieving the maximum load capacity. Next, the position of each X is updated in each

iteration corresponding to the current positions of particles, the best *X* found, and the random factor. Finally, the optimised result and variables are achieved after N_{it} th iterations.

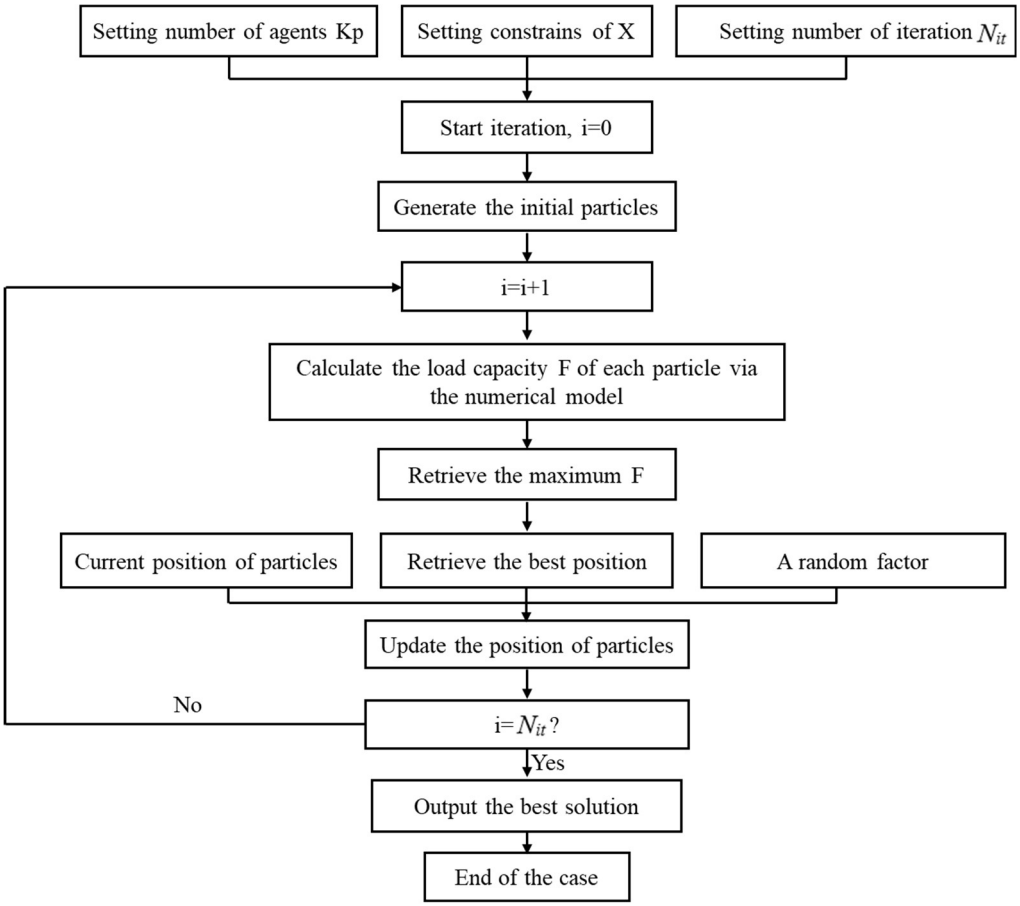
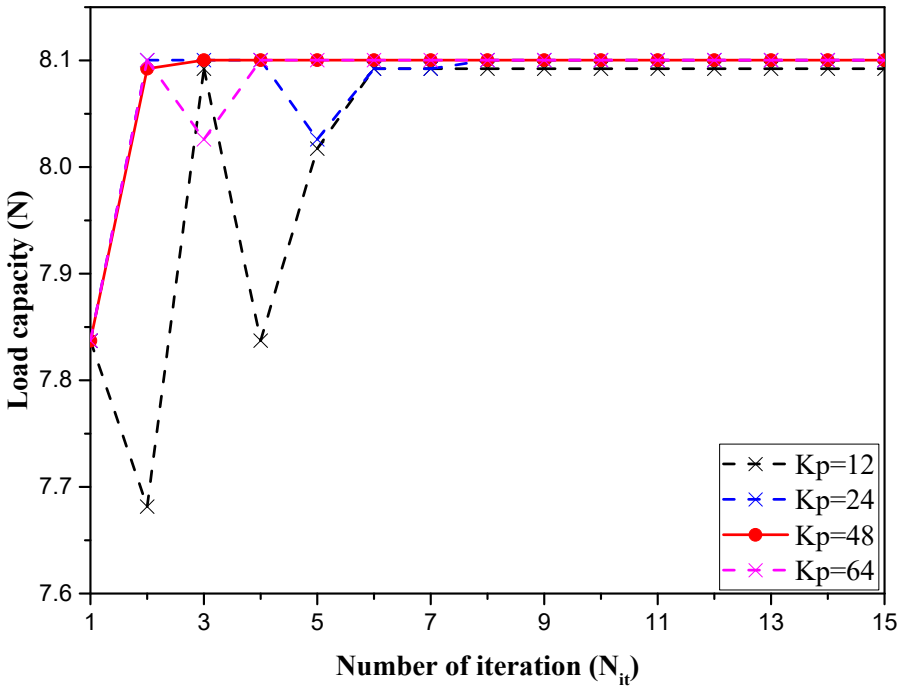


Figure 6-3: The groove configuration optimisation process

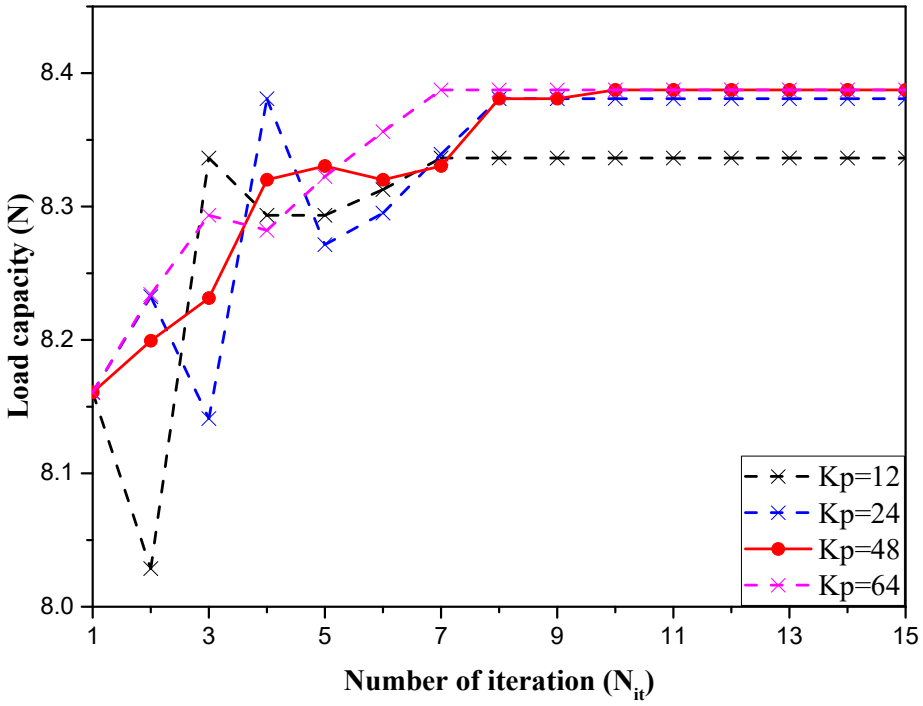
6.4.2 Optimisation results

The progress of the proposed optimisation process (the novel optimisation) is shown in Figure 6-4. For comparison, an optimisation process in an undivided

optimisation domain is also shown as the conventional optimisation approach. From Figure 6-4, it could be found that for both of the novel optimisation and conventional optimisation approaches, a satisfying convergence is achieved within 15 iterations. For the novel optimisation process, the optimal results are local optimum when K_p is taken as 12 or 24. When K_p is taken as 48 or 64, a higher load capacity can be found. Therefore, to find a tradeoff between finding the global optimum and saving the computational effort, in this case, the K_p is taken as 48 and the N_{it} is taken as 15.



(a)



(b)

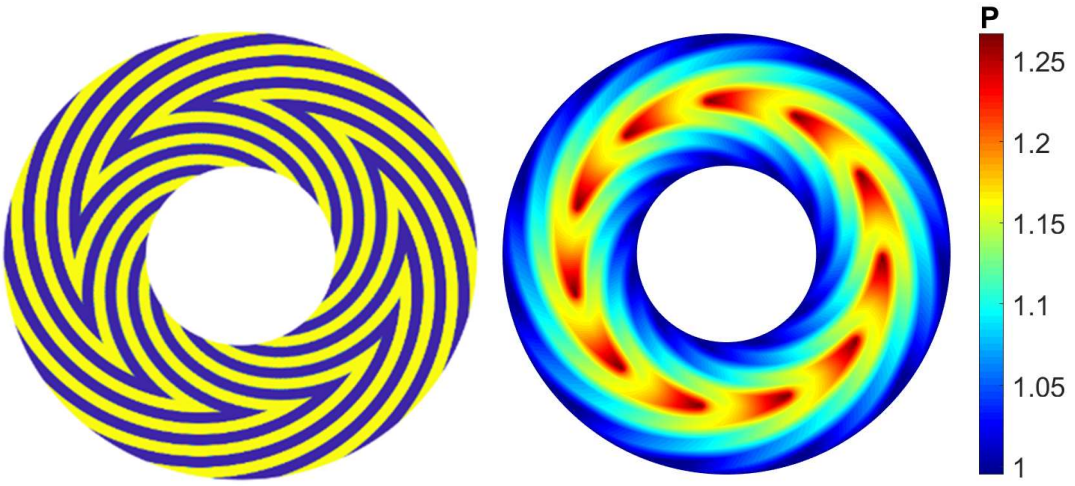
Figure 6-4: The progress of (a) the conventional optimisation; and (b) the novel optimisation

From Figure 6-4, it can also be found that the novel optimisation can achieve a higher load capacity than the conventional optimisation. The non-optimised bearing, the conventional optimised bearing and the novel optimised bearing are shown in Figures 6-5 (a-c), where the yellow part represents the groove area, and the blue part represents the ridge area. Their groove parameters are listed in Table 6-3. The pressure distributions of the three types of grooves with the operating parameters in Table 6-2 are shown in Figures 6-5 (d-f). It can be found that the novel optimised bearing achieves the highest maximum pressure, while

both the conventional optimised and the novel optimised bearings lead to a higher maximum pressure than the non-optimised bearing. The load capacity of the studied non-optimised and optimised bearings is listed in Table 6-4.

Table 6-3: The parameters of the non-optimised HGATB and the optimised HGATBs

	Non-optimised HGATB	Conventional optimised HGATB	Novel optimised HGATB	
Sealing ratio	0	$\frac{1}{20}$	$\frac{1}{15}$	
			Inner section	Outer section
Groove number	11	55	22	55
Groove angle(degree)	15	27	15	27
The ratio of groove width to ridge width	1	0.67	0.43	0.67



(a) (d)

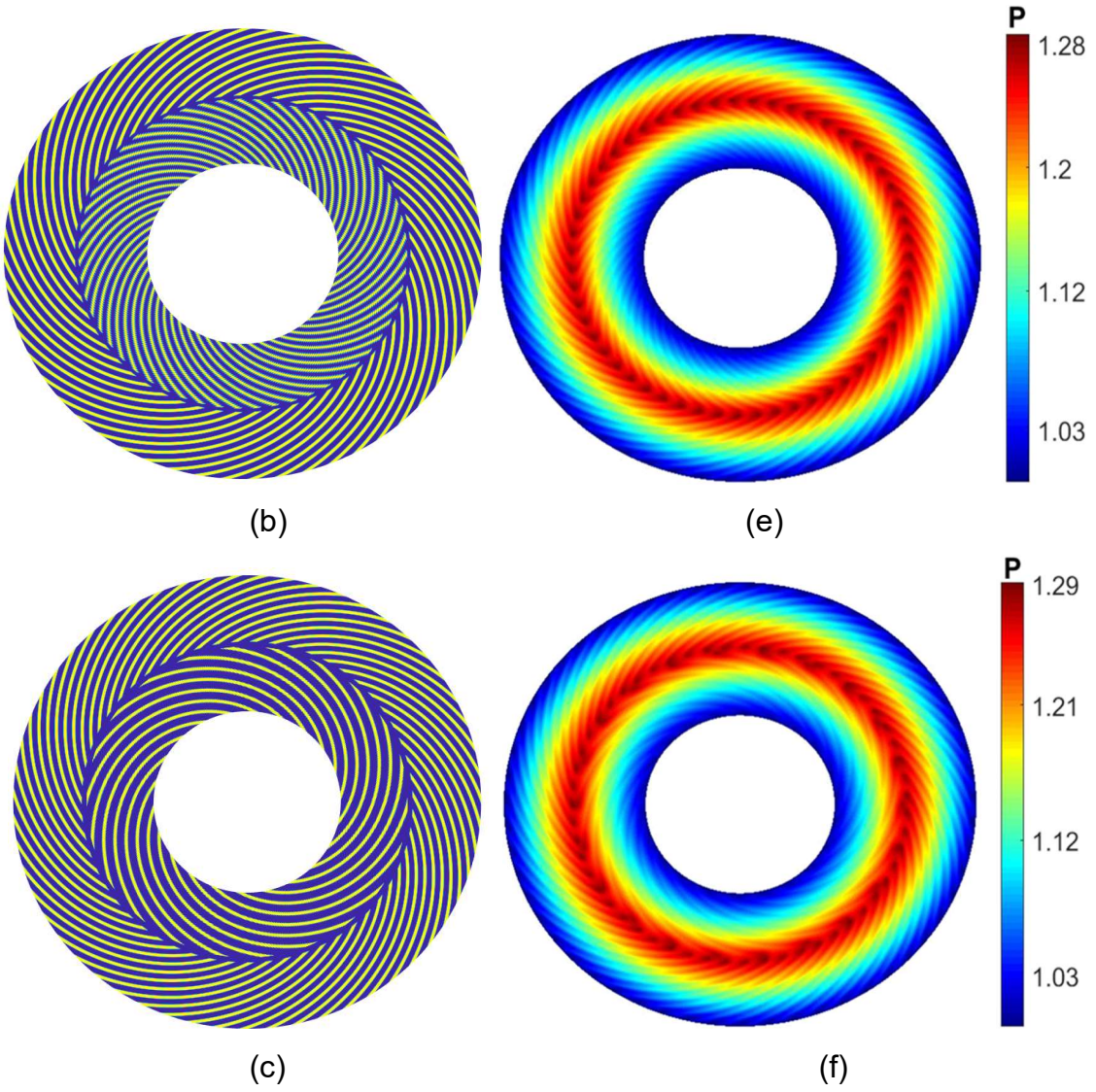


Figure 6-5: The geometry of: (a) non-optimised HGATB; (b) conventional optimised HGATB and (c) novel optimised HGATB, and the dimensionless pressure distribution of: (d) non-optimised HGATB; (e) conventional optimised HGATB and (f) novel optimised HGATB

As it is evident from Table 6-4, both of the optimised bearings lead to a higher load capacity than the non-optimised bearing, while the novel optimised bearing

achieves the highest load capacity.

Table 6-4: The load capacity of the non-optimised HGATB and the optimised HGATBs

	Non-optimised HGATB	Conventional optimised HGATB	Novel optimised HGATB
Load capacity (N)	6.08	8.10	8.38
Increment percentage	-	33.22%	37.83%

The dynamic stiffness and damping coefficients of the non-optimised HGATB and novel optimised HGATB under various frequency number are also compared in Figure 6-6. Both bearings show positive stiffness and damping coefficients at the studied conditions. Besides, the novel optimised bearing achieves a larger stiffness and damping coefficient than the non-optimised bearing at all the frequency number, indicating better dynamic performance.

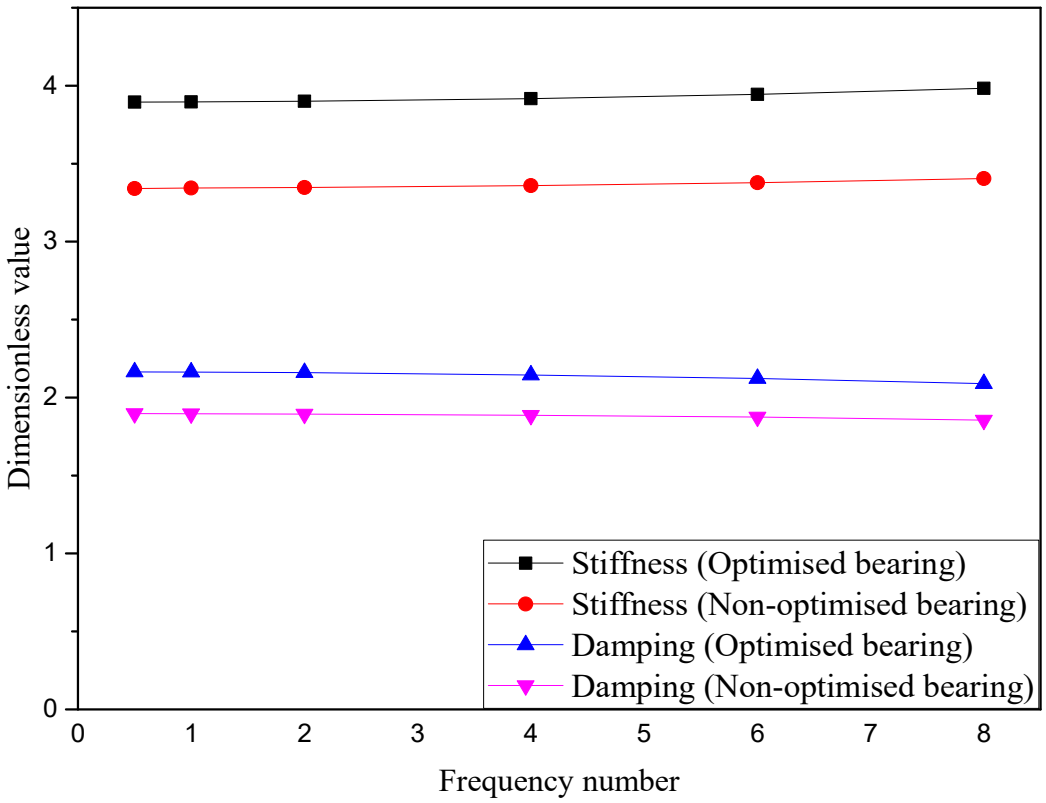
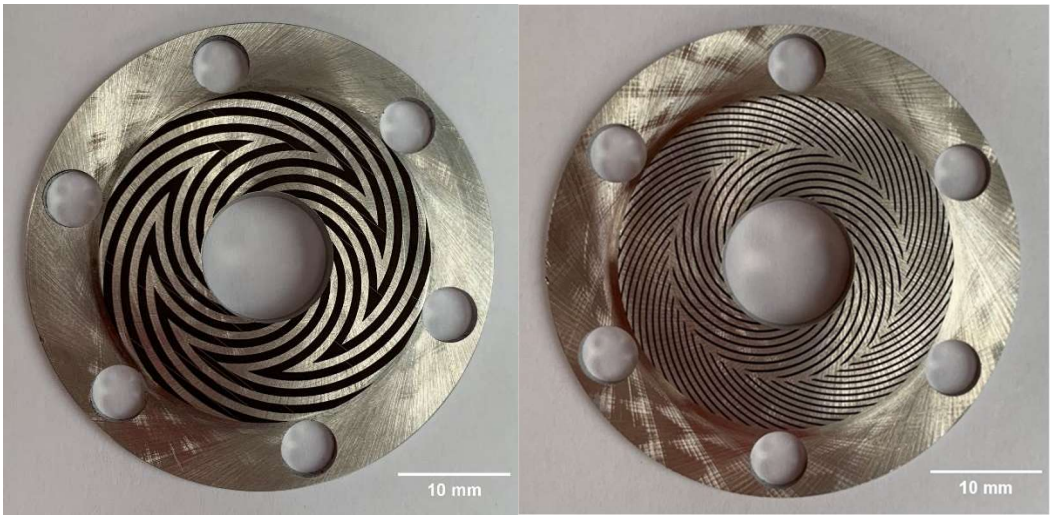


Figure 6-6: The dynamic performance of the optimised and non-optimised bearing against the frequency number at 70,000 rpm

6.5 Experiment results and discussion

To verify the proposed optimisation method, the load capacities of the non-optimised bearing and the novel optimised bearing are measured experimentally. The grooves are machined using laser ablation (LASEA LS5-001). The machined samples are shown in Figure 6-7.



(a) (b)

Figure 6-7: The geometry of (a) the non-optimised HGATB and (b) the novel optimised bearing

The test rig has been introduced in Chapter 4. During all the tests, the fluctuation of the load capacity is within ±0.4 N. In each testing condition, the load capacity is measured three times. High reproducibility is found. The mean values of the measurements are taken as the experiment results.

The load capacities acquired from experiments and simulation are shown in Figure 6-8. Here, both non-inclined and inclined air films are simulated respectively. It can be seen in Figure 6-8 that the load capacity of the novel optimised HGATB is larger than the non-optimised HGATB at all the measured speeds, demonstrating the effectiveness of the proposed optimisation method. In particular, the load capacity of the novel optimised, and the non-optimised bearings measured 6.70 N and 5.12 N respectively at 70,000 rpm, showing an

improvement of 30.77% after optimisation. It can also be pointed out that the improvement percentage increases with the rotating speeds, as shown in Figure 6-8.

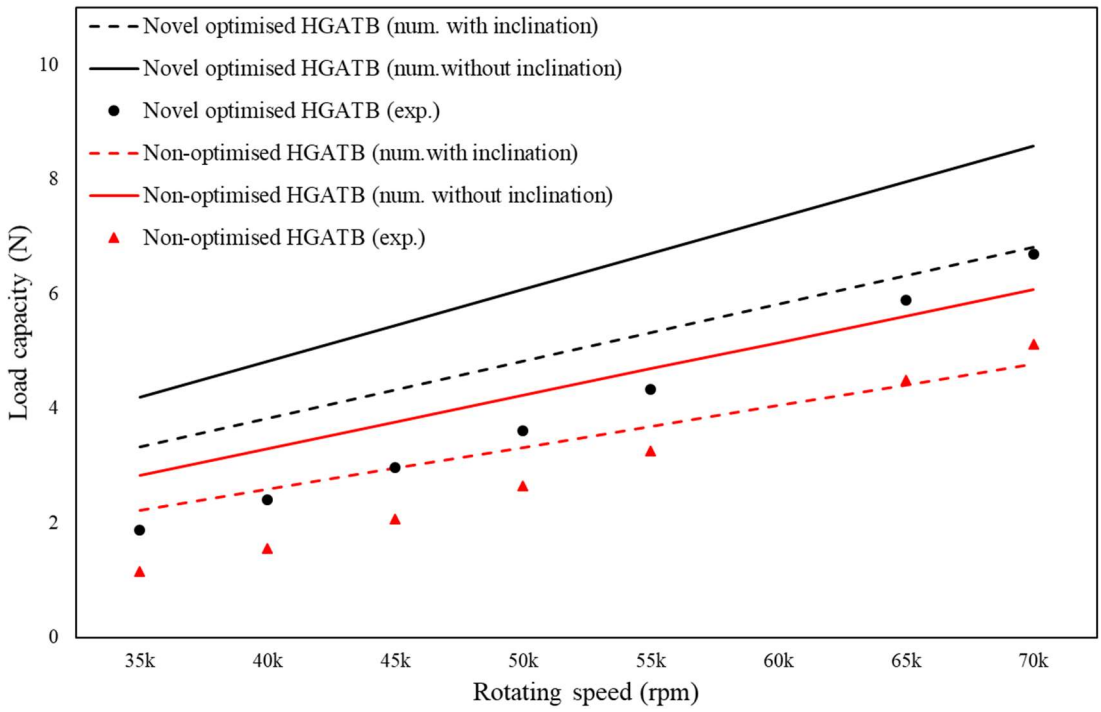


Figure 6-8: Simulation and experiment results on the load capacity of tested bearings.

In simulations, air films with both perfectly parallel surfaces and a slightly inclined surface with $\Delta h_{incline} = 2\ \mu m$ are modelled. The results of the simulations are plotted in Figure 6-8. It can be found that both for perfectly parallel and inclined surfaces, the novel optimised HGATB achieves a higher load capacity than the non-optimised HGATB at all speeds. Besides, when an inclination $\Delta h_{incline} =$

$2\,\mu m$ is considered, the simulation results show better agreement with the experimental results. The remaining discrepancies between the simulation and experiments are probably caused by the deformation of the rotating disc due to centrifugal forces [91] and the machining error of bearing components [145].

Following the above analysis, both simulation and experiment results show that the novel optimised bearing indeed performs better than the non-optimised HGATB in generating load capacity, the efficiency of the proposed groove configuration optimisation method for HGATBs has thus been proved. Simulation results also show that the novel optimised bearing has a higher load capacity than the non-optimised bearing and a conventionally optimised bearing without dividing grooves into sections, which further proves the superiority of the proposed method.

The reasons for the increased load capacity can be given as follows. Compared with the non-optimised HGATB, the conventionally optimised bearing takes the optimal groove angle, sealing ratio and number of grooves to achieve a maximum load capacity, referring to Figure 6-2. Although the ratio of groove width to ridge width is taken as the second optimal one in the conventionally optimised bearing, the difference with taking the optimal one is neglectable considering such a dense groove arrangement. As a result, the load capacity of the conventionally

optimised bearing is higher than that of the non-optimised HGATB. The novel optimised bearing has the same groove angle, the number of grooves and the ratio of groove width to ridge width with the conventionally optimised bearing in the outer section; although the two bearings have a difference sealing ratio, that effect on the load capacity is neglectable, referring to Figure 6-2. However, in different bearing sections, the optimal groove parameters for the maximum pumping effect could be different, as shown in References [161–163]. Therefore, by adopting a different groove angle, the number of grooves and the ratio of groove width to ridge width in its inner section, which can thereby increase the pumping capability, higher load capacity is achieved in novel optimised bearing compared with the conventionally optimised bearing.

6.6 Summary

In this chapter, a novel groove configuration optimisation method is proposed for HGATBs to increase their load capacity. In the proposed method, firstly, the groove angle, the ratio of groove width to ridge width, number of grooves, and sealing ratio of the inner and the outer sections of herringbone grooves are selected as design variables, and the optimisation problem is formulated as searching for the best combination of the chosen groove parameters for achieving

the highest load capacity. Then, the best combinations of the groove parameters in each bearing section are sought by the CAPSO algorithm.

Through the optimisation, the novel optimised bearing which has different groove parameters in each section of herringbone grooves are found to achieve a higher load capacity than the non-optimised HGATB and the bearing optimised in one section. Moreover, at the simulated conditions, the novel optimised bearing has higher dynamic stiffness and damping coefficients than the non-optimised bearing, demonstrating a better dynamic performance.

The inclination of the air film surface is again found to have a substantial effect to load capacity of tested bearings. When a modified air film thickness is considered, the obtained numerical results show a better agreement with the experiment results. At all of the tested speeds, the novel optimised bearing achieves a higher load capacity than the non-optimised bearing. A 30.77% increase in load capacity is proved experimentally at 70,000 rpm. Moreover, a tendency can be observed that the increment percentage is increasing with the rotating speed, which means a higher increment percentage is achievable if the rotating speed is not limited by the motor.

The main contributions of this chapter are: (1) the design and verification of a novel groove configuration optimisation method for HGATBs to increase their load

capacity; (2) the proof that a higher load capacity can be obtained by adopting different groove parameters in different sections of HGATBs. It needs to be pointed out that although the optimised grooves achieve a certain improvement in load capacity, there is no guaranty that other performances will not be affected. Multiple-objective optimisations can be considered in the future for achieving the best performance in several aspects at the same time. Also, considering more design parameters and adopting higher sampling resolution of permissible values can be conducted in the future with the improvement in computer speed.

CHAPTER 7 CONCLUSIONS AND FUTURE WORK

7.1 Introduction

This chapter presents the conclusions from this study; followed by the novel contributions of this PhD research. Suggestions for future research projects are given in the last section.

7.2 Conclusions

The overall aims of this research are to develop novel micro surface structures for grooved aerodynamic thrust bearings to achieve a considerable increase in load capacity when operating under a given air film thickness acceptable in engineering practice, which will help widen the application of grooved aerodynamic thrust bearings while ensuring a safe operation. This is achieved by the development of a novel biomimetic bearing and the proposition of two novel CAPSO-based optimisation methods for conventional spiral- and herringbone-grooved bearings.

Among all the three methods, the groove configuration optimisation method presented in Chapter 6 achieves the maximum load capacity with the same bearing dimensions. However, the biomimetic design and groove geometry optimisation methods presented in Chapter 4 and 5 are also meaningful since they have addressed different limitations of the current performance-improving methods for grooved aerodynamic bearings, i.e. none of existing methods have been carried out under the inspiration of biology, and there are limited publications concerning finding novel and non-uniform grooves with flexibly changed geometries. The main conclusions of this study are listed below:

1) Micro-grid structures of dragonfly wings can help produce load capacity in fluid-film lubrications. The biomimetic bearing, which mimics quadrilateral micro-grid structures of dragonfly wings with a velocity angle of 24^0, can achieve a 46.11% higher load capacity compared to an optimised conventional spiral-grooved bearing, as verified by the experiments.

2) The proposed novel groove geometry optimisation method, which allows the possibility of finding either discontinuous or continuous grooves, can find completely new groove geometries for thrust bearings with a 168.68% higher load capacity, compared with a non-optimised spiral-grooved bearing, as verified by the experiments.

3) The proposed new groove configuration optimisation method, which when optimising the herringbone grooves in sections, can find completely new groove configurations for HGATBs with a 30.77% higher load capacity, compared with a non-optimised herringbone-grooved bearing, again verified by the experiments.

4) The inclination of the air film surface was present in the experiments due to the difficulties in achieving absolute parallelism between bearing components; and it was found to have a substantial effect on the loading capacity of the tested bearings. Accordingly, a modified air film thickness was considered, and the obtained numerical results then showed a better agreement with the experiment results.

5) It is both theoretically and experimentally verified that with the novel biomimetic and optimal design methods proposed in this study, the load capacity of grooved aerodynamic thrust bearings can be increased. The aims and objectives of the research have thus been met.

7.3 Summary of novel contributions to knowledge

The novel contributions of this PhD research can be listed as follows:

1) It is the first time that a biomimetic aerodynamic thrust bearing has been presented. This dragonfly wing inspired bearing can achieve a 46.11% higher load capacity compared to an optimised conventional spiral-grooved bearing.

2) A novel groove geometry optimisation method for spiral-grooved bearings is proposed. A completely new groove geometry, which is formed by discontinuous grooves, is discovered with the method. A bearing with the new groove geometry can achieve a 168.68% higher load capacity compared to a non-optimised conventional spiral-grooved bearing.

3) A novel groove configuration optimisation method for herringbone-grooved bearings is proposed. A completely new groove configuration, which adopts different groove parameters in the inner and outer sections of the bearing, is delivered through the proposed method. A bearing with the new groove configuration can achieve a 30.77% higher load capacity compared to a non-optimised conventional herringbone-grooved bearing.

7.4 Proposal for future work

It is proposed that the future development of research work from this study should

include one of the following topics:

(1) Explore potential applications of dragonfly wings' biomimetic surfaces

Dragonfly wings' biomimetic surfaces could have great potential for aeronautical and energy applications. For example, equipped with dragonfly wing biomimetic surfaces, wind turbines could generate considerable extra power without additional costs; aeroplanes could have reduced wing sizes or even no wings; centrifugal air compressors could have reduced diameters and avoid critical stresses; and turbines and propellers could be more efficient. These potential applications can also be explored in future work.

(2) Explore potential applications of optimisation methods

The optimisation methods proposed in this study, which combined optimisation algorithms with CFD simulations, have great potential for aeronautical, energy and agricultural applications. For example, by combining optimisation algorithms with CFD simulations, the optimal shape of aeroplane wings and high-speed train heads, along with cars which can achieve the best aerodynamic performance could be revealed. Furthermore, using these combinations the optimal profile of diffusers, compressors, turbines, and propellers for different applications could be explored; and optimal ventilation systems, which are vital to maintaining

desired environmental conditions in intensive production systems, could be designed in the agricultural industry.

(3) Explore potential applications of biomimetic and/or optimal design methods for improving other bearing performances

The objective of this study is to improve the load capacity of grooved aerodynamic thrust bearings. However, other bearing performances, such as stiffness, damping, torque, or any combination of them, may also be of extreme importance to different applications. Therefore, in the future, the objective of the proposed biomimetic and/or optimal design methods can be modified to improve other bearing performances, and thus further widen the applications of grooved aerodynamic bearings.

(4) Further model refinements to explain the remaining discrepancy with experimental data

In this study, after considering the inclination of the air films, which were present in the experiments due to the difficulty in achieving absolute parallel surfaces, the discrepancy between the simulation and the experiments was reduced to an acceptable range. The remaining discrepancies between the simulation and the experiments are probably caused by the deformation of the rotating disc due to

centrifugal forces and the machining error of the bearings' components. These effects can be considered in a refined modelling process to further reduce the discrepancies between the simulation and the experiments in future work.

APPENDIX

The discretization of the modified Reynolds equation

In this study, FDM is used to discretize the modified Reynolds Equation. For thrust air bearing, the study domain is a rectangle domain, as shown in Figure A-1.

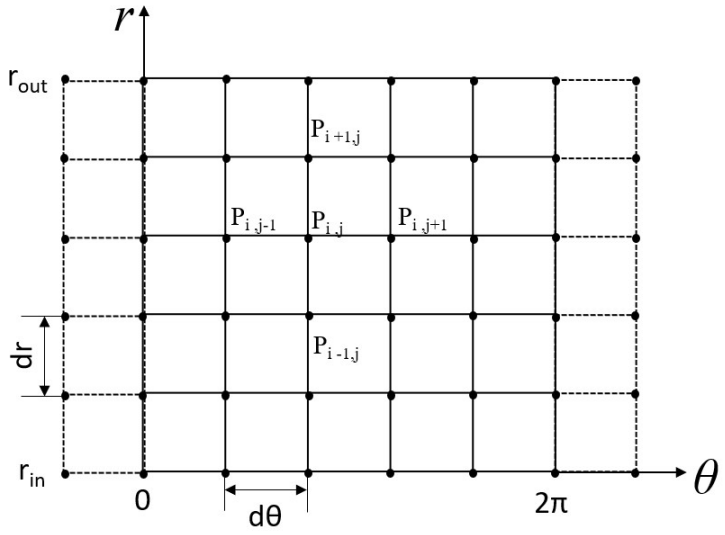


Figure A-1 Grid for computation: ● nodes corresponding to computational points

The domain occupied by the film is covered by mesh grids. The computing points are placed where the grid lines cross. The values on the bearing edges, namely on the upset and lowest edges of the grid, are known. The grid is extended by one mesh at either side horizontally to be able to take the boundary conditions of

periodicity into account at x = 0 and x = 2πR.

Consider a computational point $P_{i,j}$ situated toward the middle of the domain,$P_{i-1,j}$, $P_{i+1,j}$, $P_{i,j-1}$, $P_{i,j+1}$ are used to designate the points of the grid surrounding the point $P_{i,j}$. By Taylor's theorem:

$$P_{i+1,j} = P_{i,j} + \Delta \mathrm{r}\frac{\partial \mathrm{p}}{\partial \mathrm{r}} + \frac{\Delta \mathrm{r}^2}{2!}\frac{\partial^2 p}{\partial r^2} + \text{higher order terms} \quad \text{(A-1)}$$

$$P_{i-1,j} = P_{i,j} - \Delta \mathrm{r}\frac{\partial \mathrm{p}}{\partial \mathrm{r}} + \frac{\Delta \mathrm{r}^2}{2!}\frac{\partial^2 p}{\partial r^2} + \text{higher order terms} \quad \text{(A-2)}$$

The terms containing third and higher-order derivatives can be ignored. Therefore, it can be obtained:

$$\frac{\partial \mathrm{p}}{\partial \mathrm{r}} = \frac{P_{i+1,j} - P_{i-1,j}}{2\Delta \mathrm{r}} \quad \text{(A-3)}$$

$$\frac{\partial^2 p}{\partial r^2} = \frac{P_{i+1,j} + P_{i-1,j} - 2P_{i,j}}{\Delta \mathrm{r}^2} \quad \text{(A-4)}$$

Similarly:

$$\frac{\partial \mathrm{p}}{\partial \theta} = \frac{P_{i,j+1} - P_{i,j-1}}{2\Delta \theta} \quad \text{(A-5)}$$

$$\frac{\partial^2 p}{\partial \theta^2} = \frac{P_{i,j+1} + P_{i,j-1} - 2P_{i,j}}{\Delta \theta^2} \quad \text{(A-6)}$$

To solve the discretized modified Reynolds Equation, the FVM is also adopted in this study. Figure A-2 shows an example of a control volume Ω (blue area) which has a thickness *h* in the *z*-direction. From the mass flow balance on the control

volume Ω, the equation (A-7) can be obtained:

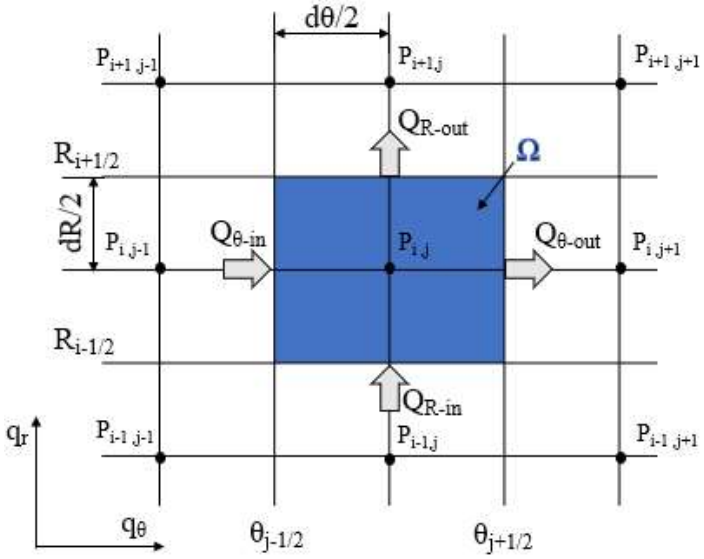


Figure A-2 A control volume Ω

$$Q_{R\text{-}in} + Q_{\theta\text{-}in} - Q_{R\text{-}out} - Q_{\theta\text{-}out} = 0 \qquad \text{(A-7)}$$

Here, $Q_{R\text{-}in}$ and $Q_{\theta\text{-}in}$ is the mass flow entering into the control volume Ω, while $Q_{R\text{-}out}$ and $Q_{\theta\text{-}out}$ is the mass flow leaving the control volume Ω.

Since the mass flow rate in θ-direction and *r*-direction can be calculated as:

$$q_\theta = -\Phi_p P H^3 \frac{\partial P}{\partial \theta} + \mathrm{f(Kn)} \Lambda R P H \qquad \text{(A-8)}$$

$$q_r = -\Phi_p R P H^3 \frac{\partial P}{\partial R} \qquad \text{(A-9)}$$

It can be concluded that:

$$Q_\theta = \int_{R_{i-1/2}}^{R_{i+1/2}} \left(-\Phi_p P H^3 \frac{\partial P}{\partial \theta} + \mathrm{f(Kn)} \Lambda R P H\right) dR \qquad \text{(A-10)}$$

$$Q_r = \int_{\theta_{j-1/2}}^{\theta_{j+1/2}} (-\Phi_p R P H^3 \frac{\partial P}{\partial R}) d\theta \quad \text{(A-11)}$$

Therefore:

$$Q_{\theta-in} = (-\Phi_p P_{i,j-\frac{1}{2}} H^3_{i,j-\frac{1}{2}} * \frac{P_{i,j}-P_{i,j-1}}{d\theta} + \mathrm{f(Kn)} \Lambda R_i P_{i,j-\frac{1}{2}} H_{i,j-\frac{1}{2}}) * dR \quad \text{(A-12)}$$

$$Q_{R-in} = (-\Phi_p R_{i-\frac{1}{2}} P_{i-\frac{1}{2},j} H^3_{i-\frac{1}{2},j} * \frac{P_{i,j}-P_{i-1,j}}{dR}) * d\theta \quad \text{(A-13)}$$

$$Q_{\theta-out} = (-\Phi_p P_{i,j+\frac{1}{2}} H^3_{i,j+\frac{1}{2}} * \frac{P_{i,j+1}-P_{i,j}}{d\theta} + \mathrm{f(Kn)} \Lambda R_i P_{i,j+\frac{1}{2}} H_{i,j+\frac{1}{2}}) * dR \quad \text{(A-14)}$$

$$Q_{R-out} = (-\Phi_p R_{i+\frac{1}{2}} P_{i+\frac{1}{2},j} H^3_{i+\frac{1}{2},j} * \frac{P_{i+1,j}-P_{i,j}}{dR}) * d\theta \quad \text{(A-15)}$$

Combining equations (A-12) to (A-15) with equation (A-7), at node (i,j), the following equation can be obtained:

$$\mathrm{A}_{i,j} * \mathrm{P}^2_{i,j} + \mathrm{B}_{i,j} * P_{i,j} + \mathrm{C}_{i,j} * \mathrm{P}^2_{i+1,j} + \mathrm{D}_{i,j} * \mathrm{P}^2_{i-1,j} + \mathrm{E}_{i,j} * \mathrm{P}^2_{i,j+1} + \mathrm{F}_{i,j} * \mathrm{P}^2_{i,j-1} + \mathrm{G}_{i,j} * P_{i,j+1} + \mathrm{H}_{i,j} * P_{i,j-1} = 0 \quad \text{(A-16)}$$

Here, $\mathrm{A}_{i,j} = \Phi_p H^3_{i,j-\frac{1}{2}} * \frac{dR}{2d\theta} + \Phi_p H^3_{i,j+\frac{1}{2}} * \frac{dR}{2d\theta} + \Phi_p R_{i-\frac{1}{2}} H^3_{i-\frac{1}{2},j} * \frac{d\theta}{2d} + \Phi_p R_{i+\frac{1}{2}} H^3_{i+\frac{1}{2},j} * \frac{d\theta}{2dR}$; $\mathrm{B}_{i,j} = \mathrm{f(Kn)} \Lambda R_i H_{i,j+\frac{1}{2}} * \frac{dR}{2} - \mathrm{f(Kn)} \Lambda R_i H_{i,j-\frac{1}{2}} * \frac{dR}{2}$; $\mathrm{C}_{i,j} = -\Phi_p R_{i+\frac{1}{2}} H^3_{i+\frac{1}{2},j} * \frac{d\theta}{2dR}$; $\mathrm{D}_{i,j} = -\Phi_p R_{i-\frac{1}{2}} H^3_{i-\frac{1}{2},j} * \frac{d\theta}{2dR}$; $\mathrm{E}_{i,j} = -\Phi_p H^3_{i,j+\frac{1}{2}} * \frac{dR}{2d}$; $\mathrm{F}_{i,j} = -\Phi_p H^3_{i,j-\frac{1}{2}} * \frac{dR}{2d\theta}$, $\mathrm{G}_{i,j} = \mathrm{f(Kn)} \Lambda R_i H_{i,j+\frac{1}{2}} * \frac{dR}{2}$, $\mathrm{H}_{i,j} = -\mathrm{f(Kn)} \Lambda R_i H_{i,j-\frac{1}{2}} * \frac{dR}{2}$.

Thus, a linear system of M × N equations can be obtained if the grid has M and N points in the R and θ directions, respectively.

REFERENCES

[1] DellaCorte C, Bruckner RJ. Remaining technical challenges and future plans for oil-free turbomachinery. J Eng Gas Turbines Power 2011;133:1–7. doi:10.1115/1.4002271.

[2] Gu L, Guenat E, Schiffmann J. A Review of Grooved Dynamic Gas Bearings. Appl Mech Rev 2020;72:010802. doi:10.1115/1.4044191.

[3] Wang CC. Chaotic Behaviour Investigation of a Front Opposed-Hemispherical Spiral-Grooved Air Bearing System. Shock Vib 2017;2017:8985040. doi:10.1155/2017/8985040.

[4] Rosset K, Mounier V, Guenat E, Schiffmann J. Multi-objective optimization of turbo-ORC systems for waste heat recovery on passenger car engines. Energy 2018;159:751–65. doi:10.1016/j.energy.2018.06.193.

[5] Guenat E, Schiffmann J. Dynamic force coefficients identification on air-lubricated herringbone grooved journal bearing. Mech Syst Signal Process 2020;136:106498. doi:10.1016/j.ymssp.2019.106498.

[6] Hashimoto H, Ochiai M. Optimization of Groove Geometry for Thrust Air

Bearing to Maximize Bearing Stiffness. J Tribol 2008;130:031101. doi:10.1115/1.2913546.

[7] Chen G, Ju B, Fang H, Chen Y, Yu N, Wan Y. Air bearing: academic insights and trend analysis. Int J Adv Manuf Technol 2020;106:1191–202. doi:10.1007/s00170-019-04663-5.

[8] Shi M, Liu X, Feng K, Zhang K, Huang M. Running Performance of a Squeeze Film Air Bearing with Flexure Pivot Tilting Pad. Tribol Trans 2020;63:704–17. doi:10.1080/10402004.2020.1736360.

[9] Popescu A, Houpert L, Olaru DN. Four approaches for calculating power losses in an angular contact ball bearing. Mech Mach Theory 2020;144:103669. doi:10.1016/j.mechmachtheory.2019.103669.

[10] Cen H, Lugt PM. Replenishment of the EHL contacts in a grease lubricated ball bearing. Tribol Int 2020;146:106064. doi:10.1016/j.triboint.2019.106064.

[11] Fonseca CA, Santos I, Weber HI. An experimental and theoretical approach of a pinned and a conventional ball bearing for active magnetic bearings. Mech Syst Signal Process 2020;138:106541. doi:10.1016/j.ymssp.2019.106541.

[12] Soni T, Dutt JK, Das AS. Magnetic Bearings for Marine Rotor Systems - Effect of Standard Ship Maneuver. IEEE Trans Ind Electron 2020;0046:1–1. doi:10.1109/tie.2020.2967664.

[13] Najar FA, Harmain GA. Influence on temperature profile in an oil film in thrust bearings using an embedded cooling circuitry beneath the pad surface: An experimental investigation. Proc Inst Mech Eng Part J J Eng Tribol 2020;234:676–92. doi:10.1177/1350650119886508.

[14] Zheng L, Zhu H, Zhu J, Deng Y. Effects of oil film thickness and viscosity on the performance of misaligned journal bearings with couple stress lubricants. Tribol Int 2020;146:106229. doi:10.1016/j.triboint.2020.106229.

[15] Schiffmann J. Integrated design, optimization and experimental investigation of a direct driven turbocompressor for domestic heat pumps. Ecole Polytechnique Federale de Lausanne, 2008. doi:10.5075/epfl-thesis-4126.

[16] Powell JW. A review of progress in gas lubrication. Rev Phys Technol 1970;1:96–129. doi:10.1088/0034-6683/1/2/303.

[17] Guenat E, Schiffmann J. Thin Gas Film Isothermal Condensation in Aerodynamic Bearings. J Tribol 2019;141:111701. doi:10.1115/1.4044447.

[18] Gu Y, Ren G, Zhou M. A fully coupled elastohydrodynamic model for static performance analysis of gas foil bearings. Tribol Int 2020;147:106297. doi:10.1016/j.triboint.2020.106297.

[19] Dobrica MB, Fillon M. Thermohydrodynamic behavior of a slider pocket bearing. J Tribol 2006;128:312–8. doi:10.1115/1.2162914.

[20] Becze S, Vuscan GI. Comparison study regarding bearing performance on 3 types of air bearingsusing Dyrobes software. MATEC Web Conf 2019;299:04001. doi:10.1051/matecconf/201929904001.

[21] Duijnhouwer FRANS, Nijmeijer HENK. Modelling and simulation of a compliant tilting pad air bearing. Proc Inst Mech Eng Part C J Mech Eng Sci 2016;230:69–87. doi:10.1177/0954406215589843.

[22] Maamari N, Krebs A, Weikert S, Wegener K. Centrally fed orifice based active aerostatic bearing with quasi-infinite static stiffness and high servo compliance. Tribol Int 2019;129:297–313. doi:10.1016/j.triboint.2018.08.024.

[23] Gao S, Cheng K, Chen S, Ding H, Fu H. CFD based investigation on influence of orifice chamber shapes for the design of aerostatic thrust bearings at ultra-high speed spindles. Tribol Int 2015;92:211–21.

doi:10.1016/j.triboint.2015.06.020.

[24] Yan R, Wang L, Wang S. Performance comparison between aerostatic bearings with orifice and porous restrictors based on parameter optimization. Aust J Mech Eng 2019;00:1–12. doi:10.1080/14484846.2019.1626529.

[25] Li W, Liu M, Ren YH, Chen Q. A high-speed precision micro-spindle use for mechanical micro-machining. Int J Adv Manuf Technol 2019;102:3197–211. doi:10.1007/s00170-019-03383-0.

[26] Gao S, Cheng K, Chen S, Ding H, Fu H. Computational design and analysis of aerostatic journal bearings with application to ultra-high speed spindles. Proc Inst Mech Eng Part C J Mech Eng Sci 2017;231:1205–20. doi:10.1177/0954406216639344.

[27] Song L, Cheng K, Ding H, Chen S, Gao Q. The static performance of the high-speed aerostatic spindles with modified discharge coefficients. Proc Inst Mech Eng Part B J Eng Manuf 2020:095440542091206. doi:10.1177/0954405420912068.

[28] Talukder HM, Stowell TB. Pneumatic hammer in an externally pressurized orifice-compensated air journal bearing. Tribol Int 2003;36:585–91.

doi:10.1016/S0301-679X(02)00247-5.

[29] Shi M, An L, Feng K, Guo Z, Liu W. Numerical and experimental study on the influence of material characteristics on the levitation performance of squeeze-film air bearing. Tribol Int 2018;126:307–16. doi:10.1016/j.triboint.2018.05.030.

[30] Li H, Deng Z. Prediction of Load-Carrying Capacity in the Radial Direction for Piezoelectric-Driven Ultrasonic Bearings. IEEE Access 2019;7:30599–614. doi:10.1109/ACCESS.2019.2897572.

[31] Ertas B, Delgado A. Compliant Hybrid Gas Bearing Using Modular Hermetically Sealed Squeeze Film Dampers. J Eng Gas Turbines Power 2019;141. doi:10.1115/1.4041310.

[32] Wang B, Sun Y, Ding Q. Free Fluid-Structure Interaction Method for Accurate Nonlinear Dynamic Characteristics of the Plain Gas Journal Bearings. J Vib Eng Technol 2020;8:149–61. doi:10.1007/s42417-019-00086-4.

[33] Samanta P, Murmu NC, Khonsari MM. The evolution of foil bearing technology. Tribol Int 2019;135:305–23. doi:10.1016/j.triboint.2019.03.021.

[34] Shalash K, Schiffmann J. On the manufacturing of compliant foil bearings. J Manuf Process 2017;25:357–68. doi:10.1016/j.jmapro.2016.12.021.

[35] Morosi S, Santos IF. Experimental investigations of active air bearings. Proc ASME Turbo Expo 2012;7:901–10. doi:10.1115/GT2012-68766.

[36] Meli F, Kueng A, Thalmann R. Ultra precision micro-CMM using a low force 3D touch probe. Recent Dev Traceable Dimens Meas III 2005;5879:58790S. doi:10.1117/12.618692.

[37] Hwang J, Park CH, Kim SW. Estimation method for errors of an aerostatic planar XY stage based on measured profiles errors. Int J Adv Manuf Technol 2010;46:877–83. doi:10.1007/s00170-009-2008-9.

[38] Lim G, Park YP, Park NC. Analysis of dynamic response of hard disk drive according to air bearing stiffness. 2016 Asia-Pacific Magn Rec Conf APMRC 2016 2016:2–3. doi:10.1109/APMRC.2016.7524265.

[39] Belforte G, Eula G. Smart pneutronic equipments and systems for mechatronic applications. Control Eng Appl Informatics 2012;14:70–9.

[40] Tabilo-Munizaga G, Barbosa-Cánovas G V. Rheology for the food industry. J Food Eng 2005;67:147–56. doi:10.1016/j.jfoodeng.2004.05.062.

[41] Tsai MH, Hus TY, Pai KR, Shih MC. Precision position control of pneumatic servo table embedded with aerostatic bearing. 9th Int. Symp. Fluid Control Meas. Vis. 2007, FLUCOME 2007, vol. 2, 2007, p. 634–43. doi:10.1299/jsdd.2.940.

[42] Gao S, Cheng K, Ding H, Fu H. Multiphysics-based design and analysis of the high-speed aerostatic spindle with application to micro-milling. Proc Inst Mech Eng Part J J Eng Tribol 2016;230:852–71. doi:10.1177/1350650115619609.

[43] Dykas B, Howard SA. Journal design considerations for turbomachine shafts supported on foil air bearings. Tribol Trans 2004;47:508–16. doi:10.1080/05698190490493391.

[44] Devitt AJ. Porous VS. Orifice Air Bearing Technology. New Way Air Bearings; 1999.

[45] IBM Archives: IBM 1301 disk storage unit n.d. www-03.ibm.com.

[46] Gill DD, Ziegert JC, Jokiel B, Pathak JP, 2004. Next Generation Spindles for Micromilling. 2004.

[47] Yu H, Wang G, Ma W, Zhang G, Zhao Z. Research on flow characteristics

of aerostatic circular thrust bearing. J Eng 2019;2019:114–8. doi:10.1049/joe.2018.8975.

[48] Yan J, Liu Z, Zhang G, Yu X, Xu L. Feasibility study of a turbocharger rotor supported by air foil bearings with diameter of 17 mm focusing on rotordynamic performance. Proc Inst Mech Eng Part D J Automob Eng 2019;233:1331–44. doi:10.1177/0954407018758134.

[49] Guo Y, HOU Y, WANG Y, ZHAO Q, ZHENG Y, LAI T. Numerical analysis of aerodynamic lubricated double-decked protuberant foil thrust bearing. J Adv Mech Des Syst Manuf 2019;13:JAMDSM0056–JAMDSM0056. doi:10.1299/jamdsm.2019jamdsm0056.

[50] Barnett MA, Silver A. Application of air bearings to high-speed turbomachinery. SAE Tech Pap 1970:No. 700720. doi:10.4271/700720.

[51] Gao, Chen W, Lu L, Huo D, Cheng K. Aerostatic bearings design and analysis with the application to precision engineering: State-of-the-art and future perspectives. Tribol Int 2019;135:1–17. doi:10.1016/j.triboint.2019.02.020.

[52] Jena RM, Chakraverty S. Solving time-fractional Navier–Stokes equations using homotopy perturbation Elzaki transform. SN Appl Sci 2019;1:1–13.

doi:10.1007/s42452-018-0016-9.

[53] Wang LP, Min H, Peng C, Geneva N, Guo Z. A lattice-Boltzmann scheme of the Navier–Stokes equation on a three-dimensional cuboid lattice. Comput Math with Appl 2019;78:1053–75. doi:10.1016/j.camwa.2016.06.017.

[54] Malanoski SB, Pan CHT. The Static and Dynamic Characteristics of the Spiral-Grooved Thrust Bearing. J Basic Eng 1965;87:547–55. doi:10.1115/1.3650603.

[55] Bonneau D, Huitric J, Tournerie B. Finite element analysis of grooved gas thrust bearings and grooved gas face seals. J Tribol 1993;115:348–54. doi:10.1115/1.2921642.

[56] Reynolds O. On the Theory of Lubrication and Its Application to Mr. Beauchamp Tower's Experiments. Proc R Soc London 1886;40:191–203. doi:10.1098/rstl.1763.0053.

[57] Harrison WJ. The Hydrodynamical Theory of Lubrication with Special Reference to Air as a Lubricant. 1913.

[58] Whipple RTP. Herringbone Pattern Thrust Bearing. 1949.

[59] Boeker GF, Fuller DD, Kayan C. Gas-Lubricated Bearings, A Critical Survey. New York: 1958.

[60] Whitley S. The Design of the Spiral Groove Thrust Bearing. UK: 1967.

[61] Muijderman EA. Analysis and Design of Spiral-Groove Bearings. J Lubr Technol 1967;89:291.

[62] Vohr JH, Pan CHT. On the Spiral-Groooved, Self-Acting Gas Bearing. 1963.

[63] Vohr JH, Chow CY. Characteristics of herringbone-grooved, gas-lubricated journal bearings. J Basic Eng 1965;87:568–76.

[64] van der Stegen RHM. Numerical Modelling of Self-Acting Gas Lubricated Bearings with Experimental Verification. The University of Twente, 1997.

[65] Reddi MM, Chu TY. Finite element solution of the steady-state compressible lubrication problem. J Tribol 1970;92:495–502. doi:10.1115/1.3451453.

[66] Miller BA, Green I. Numerical formulation for the dynamic analysis of spiral-grooved gas face seals. J Tribol 2001;123:395–403. doi:10.1115/1.1308015.

[67] Jia C, Du C, Qiu M. Analysis of Steady-state Characteristics of Aerodynamic Bearing Based on FLUENT 2015:150–5. doi:10.2991/isrme-15.2015.35.

[68] Chang L, Zhang H. An asperity-based mathematical model for the boundary lubrication of nominally flat metallic contacts. Lubr Sci 2008;20:1–19. doi:10.1002/ls.

[69] Hua W, Yu S, Zhou W, Sett Myo K. A fast implicit algorithm for time-dependent dynamic simulations of air bearing sliders. J Tribol 2012;134:1–8. doi:10.1115/1.4006134.

[70] Yu H, Ma W. Study on two different calculation methods for thrust aerostatic bearings with single supply hole at large gas film clearance. 2010 IEEE Int Conf Mechatronics Autom ICMA 2010 2010:53–8. doi:10.1109/ICMA.2010.5588721.

[71] Bonneau D, Absi J. Analysis of Aerodynamic Journal Bearings With Small Number of Herringbone Grooves by Finite Element Method. J Tribol 1994;116:698–704. doi:10.1115/1.2927320.

[72] Arghir M, Le Lez S, Frene J. Finite-volume solution of the compressible Reynolds equation: Linear and non-linear analysis of gas bearings. Proc

Inst Mech Eng Part J J Eng Tribol 2006;220:617–27. doi:10.1243/13506501JET161.

[73] Schiffmann J. Integrated Design, Optimization and Experimental Investigation of a Direct Driven Turbocompressor for Domestic Heat Pumps. Ecole Polytechnique Federale de Lausanne, 2008. doi:10.5075/epfl-thesis-4126.

[74] Zhang C, Gu L, Wang J, Wang L. Effect of air rarefaction on the contact behaviors of air lubricated spiral-groove thrust micro-bearings. Tribol Int 2017;111:167–75. doi:10.1016/j.triboint.2017.03.004.

[75] De Kraker A, Van Ostayen RAJ, Rixen DJ. Development of a texture averaged Reynolds equation. Tribol Int 2010;43:2100–9. doi:10.1016/j.triboint.2010.06.001.

[76] Schiffmann J, Favrat D. The effect of real gas on the properties of herringbone grooved journal bearings. Tribol Int 2010;43:1602–14. doi:10.1016/j.triboint.2010.03.006.

[77] Wachmann C, Malanoski SB, Vohr JH. Thermal distortion of spiral-grooved gas-lubricated thrust bearings. J Tribol 1971;93:102–11. doi:10.1115/1.3451493.

[78] Murthy AN, Etsion I, Talke FE. Analysis of surface textured air bearing sliders with rarefaction effects. Tribol Lett 2007;28:251–61. doi:10.1007/s11249-007-9269-y.

[79] Bhore SP, Darpe AK. Investigations on characteristics of micro/meso scale gas foil journal bearings for 100-200 W class micro power systems using first order slip velocity boundary conditions and the effective viscosity model. Microsyst Technol 2013;19:509–23. doi:10.1007/s00542-012-1639-1.

[80] Hsing FC, Malanoski SB. Mean free path effect in spiral-grooved thrust bearings. J Tribol 1969;91:69–78. doi:10.1115/1.3554901.

[81] Shukla JB, Kumar S, Chandra P. Generalized reynolds equation with slip at bearing surfaces: Multiple-layer lubrication theory. Wear 1980;60:253–68. doi:10.1016/0043-1648(80)90226-4.

[82] Belforte G, Raparelli T, Viktorov V. Theoretical investigation of fluid inertia effects and stability of self-acting gas journal bearings. J Tribol 1999;121:836–43. doi:10.1115/1.2834143.

[83] Sahlin F, Glavatskih SB, Almqvist T, Larsson R. Two-dimensional CFD-analysis of micro-patterned surfaces in hydrodynamic lubrication. J Tribol

2005;127:96–102. doi:10.1115/1.1828067.

[84] Cupillard S, Glavatskih S, Cervantes MJ. Inertia effects in textured hydrodynamic contacts. Proc Inst Mech Eng Part J J Eng Tribol 2010;224:751–6. doi:10.1243/13506501JET697.

[85] Dobrica MB, Fillon M. About the validity of Reynolds equation and inertia effects in textured sliders of infinite width. Proc Inst Mech Eng Part J J Eng Tribol 2009;223:69–78. doi:10.1243/13506501JET433.

[86] Zhang Q, Guo G, Bi C. Air bearing spindle motor for hard disk drives. Tribol Trans 2005;48:468–73. doi:10.1080/05698190500313445.

[87] Hwang P, Park SS, Sohn JL, Kwon SI, Kim DH, Kim WS. Design of air turbine and air bearing for dental handpiece. Tribol Lubr 2007;23:240–7.

[88] Guenat E, Schiffmann J. Real-gas effects on aerodynamic bearings. Tribol Int 2018;120:358–68. doi:10.1016/j.triboint.2018.01.008.

[89] Hughes WF, Osterle JF. Heat Transfer Effects in Hydrostatic Thrust Bearing Lubrication. ASME Trans 1957;79:1225–8.

[90] Wilson D. Gas Lubrication Research for 1900F Non-Isothermal Operation. 1968.

[91] Waumans T, Mattheijssens J, Meuws D, Vleugels P, Peirs J, Al-Bender F, et al. Design and Testing of Aerodynamic Thrust Bearings for Micro Turbomachinery Applications. Proc PowerMEMS 2007 2007:257–60.

[92] Cunningham RE, Fleming DP, Anderson WJ. Experimental Stability Studies of the Herringbone-Grooved Gas-Lubricated Journal Bearing. J Lubr Technol 1969;91:52–7.

[93] Hassan MFB. Nonlinear Analysis of Rotating Machinery Running on Foil-Air Bearings. The University of Manchester, 2017.

[94] Hashimoto H, Ochiai M, Nanba T. Theoretical Analysis and Optimum Design of High Speed Air Film Thrust Bearings. J Adv Mech Des Syst Manuf 2007;1:306–18. doi:10.1299/jamdsm.1.306.

[95] Ibrahim, M.D., Namba, T., Ochiai, M. and Hashimoto H. Optimum Design of Thrust Air Bearing for Hard Disk Drive Spindle Motor. J Adv Mech Des Syst Manuf 2010;4:70–81. doi:10.1299/kikaic.77.234.

[96] Hashimoto H, Ochiai M. Theoretical analysis and optimum design of high speed gas film thrust bearings (1st report, static and dynamic characteristic analysis with experimental verifications). Nihon Kikai Gakkai Ronbunshu, C Hen/Transactions Japan Soc Mech Eng Part C 2006;72:1311–9.

doi:10.1299/jamdsm.1.102.

[97] Hashimoto H, Namba T. Optimization of groove geometry for-thrust air bearing according to various objective functions. J Tribol 2009;131:041704. doi:10.1115/1.3201860.

[98] Chow CY, Vohr JH. Helical-Grooved Journal Bearing Operated in Turbulent Regime. J Lubr Technol 1970;92:346–57. doi:10.1115/1.3451407.

[99] Shan XC, Zhang QD, Sun YF, Maeda R. Studies on a micro turbine device with both journal- and thrust-air bearings. Microsyst Technol 2007;13:1501–8. doi:10.1007/s00542-006-0346-1.

[100] James, D.D. and Potter A. Numerical analysis of the gas-lubricated spiral-groove thrust bearing-compressor. J Lubr Technol 1967;89:439–43.

[101] Satomi T, Lin G. Design optimization of spirally grooved thrust air bearings for polygon mirror laser scanners. JSME Int Journal Ser C, Dyn Control Robot Des Manuf 1993;36:393–9.

[102] Zhang QD, Shan XC. Dynamic characteristics of micro air bearings for microsystems. Microsyst Technol 2008;14:229–34. doi:10.1007/s00542-007-0414-1.

[103] Zhang Q, Shan XC, Guo G, Wong S. Performance analysis of air bearing in a micro system. Mater Sci Eng A 2006;423:225–9. doi:10.1016/j.msea.2005.10.076.

[104] Tala-Ighil N, Fillon M, Maspeyrot P. Effect of textured area on the performances of a hydrodynamic journal bearing. Tribol Int 2011;44:211–9. doi:10.1016/j.triboint.2010.10.003.

[105] Manser B, Belaidi I, Hamrani A, Khelladi S, Bakir F. Performance of hydrodynamic journal bearing under the combined influence of textured surface and journal misalignment: A numerical survey. Comptes Rendus - Mec 2019;347:141–65. doi:10.1016/j.crme.2018.11.002.

[106] Zhang Y, Chen G, Wang L. Thermoelastohydrodynamic analysis of misaligned bearings with texture on journal surface under high-speed and heavy-load conditions. Chinese J Aeronaut 2019;32:1331–42. doi:10.1016/j.cja.2018.08.005.

[107] Wang CC, Lee RM, Yau HT, Lee TE. Nonlinear analysis and simulation of active hybrid aerodynamic and aerostatic bearing system. J Low Freq Noise Vib Act Control 2018;38:1404–21. doi:10.1177/1461348418792737.

[108] Zirkelback NL. Computational Analysis of Spiral Groove Thrust Bearings

and Face Seals. Texas A&M University, 1997.

[109] Maday CJ. The One-Dimensional Optimum Hydrodynamic Gas Slider Bearing. J Lubr Technol 1968;90:281–4. doi:10.1115/1.3601547.

[110] Chow, C.Y., Cheng, H.S. and Wilcock DF. Optimum Surface Profile for the Enclosed Pocket Hydrodynamic Gas Thrust Bearing. J Lubr Technol 1970;92:318–24. doi:10.1115/1.3451402.

[111] Gross WA. Gas bearings: A survey. Wear 1963;6:423–43. doi:10.1016/0043-1648(63)90279-5.

[112] Ausman JS. An approximate analytical solution for self-acting gas lubrication of stepped sector thrust bearings. ASLE Trans 1961;4:304–13. doi:10.1080/05698196108972443.

[113] Fesanghary M, Khonsari MM. On the shape optimization of self-adaptive grooves. Tribol Trans 2011;54:256–64. doi:10.1080/10402004.2010.539772.

[114] Shahin I, Gadala M, Alqaradawi M, Badr O. Centrifugal compressor spiral dry gas seal simulation working at reverse rotation. Procedia Eng 2013;68:285–92. doi:10.1016/j.proeng.2013.12.181.

[115] Pan CHT, Kim D. Stability Characteristics of a Rigid Rotor Supported by a Gas Lubricated Spiral-Groove Conical Bearing. Int. Jt. Tribol. Conf., 2008, p. 1271–9. doi:10.1115/IJTC2006-12105.

[116] Fleming DP, Hamrock BJ. Optimization of self-acting herringbone journal bearing for maximum stability. 1973.

[117] Song L, Cheng K, Ding H, Chen S, Gao Q. Analysis of static and dynamic characteristics of spiral-grooved gas journal bearings in high speed. Proc Inst Mech Eng Part C J Mech Eng Sci 2019;233:6774–92. doi:10.1177/0954406219869751.

[118] Wong CW, Zhang X, Jacobson SA, Epstein AH. A self-acting gas thrust bearing for high-speed microrotors. J Microelectromechanical Syst 2004;13:158–64. doi:10.1109/JMEMS.2004.824900.

[119] Chen-Hui, I., Wei, Y. and Ming Q. Load capacity analysis and structural parameters optimizing of spiral groove aerodynamic bearings. J Appl Sci 2013;13:3649–58. doi:10.3923/jas.2013.3649.3658.

[120] Liu, F., Lu, Y., Zhang, Q., Zhang, Y., Gupta, P. and Müller N. Load performance analysis of three-pad fixing pad aerodynamic journal bearings with parabolic grooves. Lubr Sci 2016;28:207–20. doi:10.1002/ls.

[121] Fesanghary M, Khonsari MM. On the optimum groove shapes for load-carrying capacity enhancement in parallel flat surface bearings: Theory and experiment. Tribol Int 2013;67:254–62. doi:10.1016/j.triboint.2013.08.001.

[122] Schiffmann J. Enhanced Groove Geometry for Herringbone Grooved Journal Bearings. J Eng Gas Turbines Power 2013;135:102501. doi:10.1115/1.4025035.

[123] Ikeda, S., Arakawa, Y., Hishida, N., Hirayama, T., Matsuoka, T. and Yabe H. Herringbone-grooved bearing with non-uniform grooves for high-speed spindle Shinichi. Lubr Sci 2010;22:377–92. doi:10.1002/ls.

[124] Xu Z, Todorov E. Design of a highly biomimetic anthropomorphic robotic hand towards artificial limb regeneration. Proc - IEEE Int Conf Robot Autom 2016;2016-June:3485–92. doi:10.1109/ICRA.2016.7487528.

[125] Yao Z, Linnenberg C, Argubi-Wollesen A, Weidner R, Wulfsberg JP. Biomimetic design of an ultra-compact and light-weight soft muscle glove. Prod Eng 2017;11:731–43. doi:10.1007/s11740-017-0767-y.

[126] Shen Q, Olsen Z, Stalbaum T, Trabia S, Lee J, Hunt R, et al. Basic design of a biomimetic underwater soft robot with switchable swimming modes and programmable artificial muscles 2020;29:035038. doi:10.1088/1361-

665X/ab6fe8.

[127] Pecht GG, Hamaker JB. Non-contacting mechanical face seal. 5,441,283, 1995.

[128] X.D.Peng, J.B.Jiang, S.X.Bai, J.Y.Li. Correlational research of bionics design of dry gas face seal groove. J Mech Eng 2015;50:151–7.

[129] Gao S., Sun J., Zhang B. A method designed for bionic air bearing based on the structure of long-eared owl wing. Ind Lubr Tribol 2019;72:122–7. doi:10.1108/ILT-05-2019-0173.

[130] Pu G. Hybrid air bearings for high speed turbo machinery. University of Birmingham, 2017.

[131] Reynolds O. IV. On the theory of lubrication and its application to Mr. Beauchamp tower's experiments, including an experimental determination of the viscosity of olive oil. Philos Trans R Soc London 1886;177:157–234. doi:10.1098/rstl.1886.0005.

[132] Harrison WJ. The hydrodynamical theory of lubrication with special reference to air as a lubricant. University Press; 1913.

[133] Okamura H. A Contribution to the Numerical Analysis of Isothermal

Elastohydrodynamic Lubrication, Tribology of Reciprocating Engines. Proc. 9th Leeds-Lyon Symp. Tribol., vol. 313, 1982.

[134] Houpert LG, Hamrock BJ. Fast approach for calculating film thicknesses and pressures in elastohydrodynamically lubricated contacts at high loads. J Tribol 1986;108:411–9. doi:10.1115/1.3261220.

[135] Lubrecht AA. The numerical solution of the elastohydrodynamically lubricated line- and point contact problem, using multigrid techniques. Enschede: University of Twente, 1987.

[136] Waumans, T., Mattheijssens, J., Meuws, D., Vleugels, P., Peirs, J., Al-Bender, F. and Reynaerts D. Design and testing of aerodynamic thrust bearings for micro turbomachinery applications. Proc. 7th Int. Work. Micro Nanotechnol. Power Gener. Energy Convers. Appl., 2007, p. 257–60.

[137] Zirkelback N, Andres LS. Effect of Frequency Excitation on Force Coefficients of Spiral Groove Gas Seals 1999;121:853–61.

[138] Liu Y, Shen X, Xu W. Numerical analysis of dynamic coefficients for gas film face seals. J Tribol 2002;124:743–54. doi:10.1115/1.1472459.

[139] Faria MTC. An Efficient Finite Element Procedure for Analysis of High-

Speed Spiral Groove Gas 2001;123. doi:10.1115/1.1331276.

[140] Helmli F, Danzl R, Prantl M, Grabner M. Ultra High Speed 3D Measurement with the Focus Variation Method. Fringe, Springer; 2013. doi:10.1007/978-3-642-36359-7.

[141] Taobao n.d. www.taobao.com.

[142] Muijderman EA. spiral groove bearings. Wear 1965;17:12–7. doi:10.1016/0043-1648(69)90423-2.

[143] Lehn A, Schweizer B. Generalized Reynolds equation for fluid film problems with arbitrary boundary conditions: application to double-sided spiral groove thrust bearings. Arch Appl Mech 2016;86:743–60. doi:10.1007/s00419-015-1059-7.

[144] Yemelyanov A V., Yemelyanov IA. Physical models, theory and fundamental improvement to self-acting spiral-grooved gas bearings and visco-seals. Proc Inst Mech Eng Part J J Eng Tribol 1999;213:263–71. doi:10.1243/1350650991542659.

[145] Cui C, Ono K. Theoretical and experimental investigation of an externally pressurized porous annular thrust gas bearing and its optimal design. J

Tribol 1997;119:486–92. doi:10.1115/1.2833524.

[146] Xiang G, Han Y, Wang J, Xiao K, Li J. A transient hydrodynamic lubrication comparative analysis for misaligned micro-grooved bearing considering axial reciprocating movement of shaft. Tribol Int 2019;132:11–23. doi:10.1016/j.triboint.2018.12.004.

[147] Rondonuwu C. Performance of vertical herringbone grooved hydrodynamic journal bearings. NATIONAL UNIVERSITY OF SINGAPORE, 2004.

[148] Wang X, He Z, Yang J, Cai L. Residential level electric vehicle and grid dynamic interaction modeling and stability analysis. IEEJ Trans Electr Electron Eng 2018;13:1404–11. doi:10.1002/tee.22706.

[149] Hassani L, Daneshvar kakhki M, Sabouhi sabouni M, Ghanbari R. The optimization of resilience and sustainability using mathematical programming models and metaheuristic algorithms. J Clean Prod 2019;228:1062–72. doi:10.1016/j.jclepro.2019.04.324.

[150] Hajimirzaei B, Navimipour NJ. Intrusion detection for cloud computing using neural networks and artificial bee colony optimization algorithm. ICT Express 2019;5:56–9. doi:10.1016/j.icte.2018.01.014.

[151] Rubaiee S, Yildirim MB. An energy-aware multiobjective ant colony algorithm to minimize total completion time and energy cost on a single-machine preemptive scheduling. Comput Ind Eng 2019;127:240–52. doi:10.1016/j.cie.2018.12.020.

[152] Monsef H, Naghashzadegan M, Jamali A, Farmani R. Comparison of evolutionary multi objective optimization algorithms in optimum design of water distribution network. Ain Shams Eng J 2019;10:103–11. doi:10.1016/j.asej.2018.04.003.

[153] Basu S, Kannayaram G, Ramasubbareddy S, Venkatasubbaiah C. for Monitoring of Virtual Machines in Cloud Environment. vol. 2. Springer Singapore; 1927. doi:10.1007/978-981-13-1927-3.

[154] Aghbashlo M, Tabatabaei M, Nadian MH, Davoodnia V, Soltanian S. Prognostication of lignocellulosic biomass pyrolysis behavior using ANFIS model tuned by PSO algorithm. Fuel 2019;253:189–98. doi:10.1016/j.fuel.2019.04.169.

[155] Yang X. Nature-inspired metaheuristic algorithms. 2010.

[156] Zhou Q, Zhang W, Cash S, Olatunbosun O, Xu H, Lu G. Intelligent sizing of a series hybrid electric power-train system based on Chaos-enhanced

accelerated particle swarm optimization. Appl Energy 2017;189:588–601. doi:10.1016/j.apenergy.2016.12.074.

[157] Luo YZ, Tang GJ, Zhou LN. Hybrid approach for solving systems of nonlinear equations using chaos optimization and quasi-Newton method. Appl Soft Comput J 2008;8:1068–73. doi:10.1016/j.asoc.2007.05.013.

[158] Li J, Zhou Q, He Y, Shuai B, Li Z, Williams H, et al. Dual-loop online intelligent programming for driver-oriented predict energy management of plug-in hybrid electric vehicles. Appl Energy 2019;253. doi:10.1016/j.apenergy.2019.113617.

[159] Zhang Y, Zhou Q, Li Z, Li J, Xu H. Intelligent transient calibration of a dual-loop EGR diesel engine using chaos-enhanced accelerated particle swarm optimization algorithm. Proc Inst Mech Eng Part D J Automob Eng 2019;233:1698–711. doi:10.1177/0954407018776745.

[160] Hirayama T, Yamaguchi N, Sakai S, Hishida N, Matsuoka T, Yabe H. Optimization of groove dimensions in herringbone-grooved journal bearings for improved repeatable run-out characteristics. Tribol Int 2009;42:675–81. doi:10.1016/j.triboint.2008.09.006.

[161] Chen CY, Liu CS, Tee CK, Li YC. Application of stabilized term in free

boundary problems for optimizing bi-directional-rotation herringbone-grooved journal bearings. Appl Math Model 2017;47:826–38. doi:10.1016/j.apm.2016.11.002.

[162] Chen CY, Liu CS, Li YC. Design and characterization of miniature fluid dynamic bearing using novel multi-step elliptical grooves. Microsyst Technol 2013;21:91–100. doi:10.1007/s00542-013-2023-5.

[163] Yen R-H, Chen C-Y. Enhancement of Reversible Rotation Journal Bearing Performance Using Elliptical Grooves. J Tribol 2011;133:011704. doi:10.1115/1.4003148.